

ION BEAM-MIXED GERMANIUM AND SILICON LITHIUM ION BATTERY ANODES

By
NICHOLAS VITO

A DISSERTATION PRESENTED TO THE GRADUATE SCHOOL
OF THE UNIVERSITY OF FLORIDA IN PARTIAL FULFILLMENT
OF THE REQUIREMENTS FOR THE DEGREE OF
DOCTOR OF PHILOSOPHY

UNIVERSITY OF FLORIDA

2013

© 2013 Nicholas Vito

ACKNOWLEDGMENTS

I thank Aaron Lind, Patrick Whiting, Henry Aldridge, and Tom Martin for our many stimulating discussions, relevant or not. Rohit Mohan and Mithun Nair provided a great deal of assistance in sample preparation and have my deepest gratitude. I acknowledge Nick Rudawski and Kerry Seibein for their training, tips, and discussions relating to transmission electron microscopy. I appreciate the opportunity to work with Danijel Gostovic, who imparted a wealth of knowledge onto me regarding the FEI Strata DB235 SEM/FIB, microstructure characterization, and local electron atom probe analysis. I thank Ray Holzworth Jr. for being available to discuss any of the analysis techniques listed above. I thank Al Ogden and David Hays for training in electron beam physical vapor deposition and plasma enhanced chemical vapor deposition, respectively. I want to express my gratitude to Gregory Sawyer, Curtis Taylor, and Kathryn Harris for discussions and help with tribological and fracture experiments. Nagid Brown deserves special recognition for his help with all nanoindentation experiments. I thank Rob Elliman for his collaboration and help with ion implantation. Finally, I would like to recognize Kevin Jones, my advisor, for being a constant during my time at the University of Florida and providing every opportunity for me to complete this work.

TABLE OF CONTENTS

	<u>page</u>
ACKNOWLEDGMENTS.....	3
LIST OF FIGURES	8
LIST OF ABBREVIATIONS.....	13
ABSTRACT.....	15
CHAPTER	
1 INTRODUCTION.....	17
1.1 Lithium Ion Batteries	17
1.1.1 Road to Commercialization	18
1.1.2 Lithium Ion Battery Chemistry.....	18
1.2 Anode Materials for Lithium Ion Batteries	20
1.3 Ion Beam Mixing.....	22
1.3.1 Ion Implantation.....	23
1.3.2 Concept of Ion Beam Mixing	23
1.3.3 Adhesion Improvements due to Ion Beam Mixing.....	24
1.4 Objectives and Overview.....	26
2 EXPERIMENTAL METHODS.....	30
2.1 Methodology for Ion Beam-Mixing	30
2.1.1 Monte-Carlo Ion Simulation	31
2.1.2 Equipment for Ion Implantation.....	32
2.2 Pouch Cell Assembly	33
2.2.1 Windowed Pouch Cell	33
2.2.2 Electrode Mass Calculation	33
2.2.3 Glove Box.....	34
2.3 Electrochemical Characterization	34
2.3.1 Galvanostatic Cycling.....	34

2.3.2 Cyclic Voltammetry.....	35
2.4 Material Characterization	35
2.4.1 Optical Microscopy	35
2.4.2 Scanning Electron Microscopy	36
2.4.3 Focused Ion Beam	37
2.4.4 Transmission Electron Microscopy	39
2.4.5 Energy Dispersive X-Ray Spectroscopy	40
2.4.6 Selected Area Electron Diffraction	40
2.4.7 Nanoindentation	41
2.5 Fracture Analysis	43
2.5.1 Electrode Cracking	44
2.5.2 Fracture Measurement	45
2.5.3 Shape Descriptors.....	46
2.5.4 Statistical Analysis.....	46
3 DEPOSITION AND IMPLANTATION OF GERMANIUM AND SILICON THIN FILMS	55
3.1 Thin Film Deposition Techniques	55
3.1.1 Electron Beam Physical Vapor Deposition.....	55
3.1.1 Plasma Enhanced Chemical Vapor Deposition	56
3.2 Thin Film Characterization	57
3.2.1 Amorphous Germanium	57
3.2.2 Amorphous Silicon	58
3.3 Concluding Remarks.....	59
4 ION BEAM-MIXED GERMANIUM ELECTRODES	66
4.1 Experiments.....	67
4.1.1 Sample Preparation.....	67
4.1.2 Nanoindentation	67
4.1.3 Electrochemistry.....	68
4.2 Results.....	68
4.2.1 Thin Film Characterization.....	68

4.2.2	Nanoindentation	69
4.2.3	Electrochemistry.....	70
4.2.4	Cycling Induced Fracture.....	72
4.3	Discussion.....	73
4.3.1	Effect of Ion Implantation on Fracture Toughness	73
4.3.2	Effect of Ion Implantation on Electrochemical Properties	75
4.3.3	Effect of Ion Implantation on Electrode Failure	76
4.4	Concluding Remarks	76
5	ION BEAM-MIXED SILICON ELECTRODES	89
5.1	Experiments	90
5.1.1	Sample Preparation.....	90
5.1.2	Electrochemistry.....	90
5.2	Results	91
5.2.1	Sample Characterization	91
5.2.2	Electrochemistry.....	91
5.2.3	Cycling Induced Fracture.....	93
5.2.4	In-situ Optical Microscopy	95
5.3	Discussion.....	96
5.3.1	Effect of Ion Implantation on Electrochemical Properties	96
5.3.2	Effect of Ion Implantation on Electrode Failure	98
5.3.3	Deformations at the Nanoscale	100
5.4	Concluding Remarks	101
6	FRACTURE DUE TO CYCLING RATE AND THICKNESS OF ION BEAM-MIXED SILICON ELETRODES	113
6.1	Experiments	114
6.1.1	Sample Preparation.....	114
6.1.2	Electrochemistry.....	114
6.2	Results.....	115
6.2.1	Sample Characterization	115

6.2.2 Electrochemistry.....	116
6.2.3 Cycling Induced Fracture.....	119
6.3 Discussion.....	120
6.3.1 Effect of Ion Implantation and Thickness on Electrochemical Properties	120
6.3.2 Effect of Ion Implantation and Cycling Rate on Electrochemical Properties	120
6.3.3 Effect of Ion Implantation and Thickness on Electrode Failure.....	121
6.3.4 Effect of Cycling Rate on Electrode Failure	121
6.4 Concluding Remarks.....	122
7 ION BEAM-MIXING.....	131
8 CONCLUSIONS.....	137
8.1 Summary.....	137
8.2 Future Work	138
APPENDIX: THREE DIMENSION RECONSTRUCTION AND ANALYSIS OF SERIALY SECTIONED SOLID OXIDE FUEL CELL ELECTRODES.....	140
A.1 FIB/SEM Serial Sectioning.....	140
A.2 Phase Identification and Measurements	141
A.2.1 Alignment and Shearing.....	141
A.2.2 Labeling	142
A.2.3 Surface Generation.....	144
A.2.4 Measurements Module.....	144
A.2.5 Nodal Connectivity and Measured Average Z-Orientation.....	145
A.2.6 Active Connectivity and TPB Measurements.....	146
LIST OF REFERENCES	153
BIOGRAPHICAL SKETCH.....	160

LIST OF FIGURES

<u>Figure</u>		<u>page</u>
1-1	A schematic view of the basic battery components and operation	28
1-2	Illustration of delamination mechanism for germanium and silicon lithium ion battery electrodes during cycling	29
1-3	Illustration of damage from ion implantation comparing the interface between silicon and a substrate.....	29
2-1	Implant profile for an idealized system to promote ion beam-mixing at the current collector interface	47
2-2	Schematic of the NEC model 5SDH-4 with a SNICS sputter ion source	47
2-3	Exterior and cross-sectional view of a pouch cell.....	48
2-4	Exterior and comparison cross-sectional views of the standard and windowed pouch cell.....	49
2-5	Plots to determine the areal mass density of the substrates	50
2-6	Schematic and optics of a light microscope under bright field conditions	50
2-7	Optical ray diagram depicting different types of aberration	51
2-8	Schematic and optics of a light microscope under dark field conditions	51
2-9	Methodology for XTEM sample preparation via FIB viewed at an angle	52
2-10	Cross-sectional illustration of nanoindentation induced surface deformations.....	53
2-11	Cross-sectional illustration of the electrode cracking model.....	53
2-12	Labeling and island identification for a cracked electrode surface.....	54
3-1	Schematic of an EBPVD system.....	60
3-2	Schematic of a PECVD system	60
3-3	XTEM image of a 140 nm germanium film on a nickel-iron substrate	61
3-4	STEM images of the interface between the as-deposited germanium film and Ni ₈₀ Fe ₂₀ substrate	61
3-5	High resolution STEM bright field image of the interface between the as-deposited germanium film and Ni ₈₀ Fe ₂₀ substrate	62

3-6	STEM-HAADF image and EDS profile of the interface between the as-deposited germanium film and Ni ₈₀ Fe ₂₀ substrate	63
3-7	XTEM image of a 350 nm amorphous silicon film on a 304 stainless steel substrate.....	64
3-8	OM image of surface roughness.....	64
3-9	OM image of thin film silicon buckling event	65
3-10	Digital photograph of the PECVD silicon film deposited on stainless steel.....	65
4-1	XTEM comparison of the germanium electrodes	78
4-2	STEM bright field images of the current collector interface	78
4-3	Nanoindentation load-depth plots	79
4-4	Measured mechanical properties of the germanium thin film	79
4-5	Top-down SEM images of nanoindentations at 800 μ N	80
4-6	Top-down SEM images for an array of nanoindentations at 800 μ N	80
4-7	XTEM bright field image for an indent at 800 μ N into an as-deposited germanium film with 5 μ m spacing between indents	81
4-8	XTEM bright field image for an indent at 800 μ N into a 10 ¹⁵ Ge ⁺ cm ⁻² implanted germanium film with 1 μ m spacing between indents.....	82
4-9	Galvanostatic cycling of the germanium film at 810 mAhg ⁻¹	83
4-10	Cyclic voltammograms at a sweep rate of 278 μ Vs ⁻¹ for cycles 1, 5, and 20 of the germanium film.....	83
4-11	Cyclic voltammogram at a sweep rate of 278 μ Vs ⁻¹ for cycle 5 of the as-deposited germanium electrode and 10 ¹⁵ Ge ⁺ ion beam-mixed germanium electrode	84
4-12	Cycle life plot of each as-deposited and implanted germanium electrode galvanostatically cycled at 810 mAhg ⁻¹ for 50 cycles	85
4-13	Charge efficiency of select as-deposited and implanted germanium electrodes galvanostatically cycled at 810 mAhg ⁻¹ for 50 cycles	86
4-14	Top-down SEM images of cycled germanium electrodes at 810 mAhg ⁻¹ after 50 cycles	87
4-15	Relationship between cracked surface island size and Ge ⁺ implant dose	88
5-1	XTEM images of virgin Si electrodes prior to electrochemical cycling.....	102

5-2	Galvanostatic cycling of silicon at 4.2 A g ⁻¹	102
5-3	Cyclic voltammograms of silicon at a sweep rate of 417 μVs ⁻¹ for cycles 1, 5, and 20 .	103
5-4	Time resolved cyclic voltammograms of silicon	104
5-5	Cycle life plot of select as-deposited and implanted silicon electrodes galvanostatically cycled at 4.2 A g ⁻¹ for 100 cycles	104
5-6	Low-magnification SEM images observed at an angle of 52° of Si electrodes after galvanostatic cycling at 4.2 A g ⁻¹ for 1 cycle	105
5-7	Top-down SEM images showing the electrode morphology of ion beam-mixed silicon electrodes after galvanostatic cycling at 4.2 Ag ⁻¹ for 100 cycles.....	106
5-8	The relationships between both the average area of islands and calculated interfacial shear stresses against the Si ⁺ dose	107
5-9	Shape descriptors for the fractured silicon islands	107
5-10	Images of a 10 ¹³ Si ⁺ cm ⁻² implanted electrode	108
5-11	XTEM images of the interface between the silicon and substrate for the 10 ¹³ electrode	108
5-12	Micrographs of a 10 ¹⁶ Si ⁺ cm ⁻² implanted electrode	109
5-13	Bright field XTEM images of the 10 ¹⁶ cm ⁻² implanted silicon electrode at cycles 1, 50, and 100	109
5-14	Micrographs of a 10 ¹⁶ Si ⁺ cm ⁻² implanted electrode interface after 100 cycles	110
5-15	Micrographs of a 10 ¹⁶ Si ⁺ cm ⁻² implanted electrode steel particle after 100 cycles	110
5-16	Dark field STEM images of a 10 ¹⁶ Si ⁺ cm ⁻² implanted electrode after 100 cycles	111
5-17	OM images of an as-deposited film cracking during discharge	111
5-18	OM images of an ion beam-mixed film cracking during discharge	112
6-1	XTEM images of virgin Si electrodes prior to electrochemical cycling for various thicknesses	123
6-2	Galvanostatic cycling at 0.84 Ag ⁻¹ for the as-deposited silicon electrode for various thicknesses	124
6-3	Galvanostatic cycling at 0.84 Ag ⁻¹ for the 10 ¹⁶ Si ⁺ cm ⁻² ion beam-mixed silicon electrode for various thicknesses.....	125

6-4	Cyclic voltammogram at a sweep rate of $83 \mu\text{Vs}^{-1}$ for cycles 1, 5, and 20 of the $350 \text{ nm } 10^{16} \text{ cm}^{-2} \text{ Si}^+$ ion beam-mixed silicon electrode	126
6-5	Cyclic voltammogram at a sweep rate of $417 \mu\text{Vs}^{-1}$ for cycles 1, 5, and 20 of the $700 \text{ nm } 10^{16} \text{ Si}^+ \text{ cm}^{-2}$ ion beam-mixed silicon electrode	126
6-6	Typical cycle life data for the 700 nm silicon electrodes cycled at 4.2 A g^{-1}	127
6-7	Typical cycle life data for silicon electrodes of various thicknesses galvanostatically cycled at 0.84 A g^{-1}	127
6-8	Top-down SEM images showing the electrode morphology of the 700 nm thick silicon electrode after 100 cycles at 0.84 A g^{-1}	128
6-9	Top-down SEM images showing different crack morphologies of the $1,100 \text{ nm}$ thick silicon electrode galvanostatically cycled at 0.84 A g^{-1} for 100 cycles.....	128
6-10	Top-down SEM images showing the electrode morphology of ion beam-mixed Si electrodes after various galvanostatic cycling at rates for 100 cycles	129
6-11	Comparison of geometric properties in relation to the cycling rate for the 350 nm ion beam-mixed silicon electrodes	130
6-12	The fractal dimension of the 350 nm ion beam-mixed electrodes cycled at different rates	130
7-1	Gaussian fit to the TRIM implant prediction for Ge^+ into germanium with a nickel-iron interface at 1400 \AA	135
7-2	Fit of Equation 7-4 to the island size data of the cycled 140 nm germanium electrodes from Chapter 4	135
7-3	Gaussian fit to the TRIM implant prediction for Si^+ into silicon with a stainless steel interface at 3500 \AA	136
7-4	Fit of Equation 7-4 to the island size data of the cycled 350 nm silicon electrodes from Chapter 5	136
A-1	Top down ion beam micrographs showing the C-trench procedure	148
A-2	Cross-sectional SEM image of composite SOFC electrode with a platinum cap	148
A-3	Method to calibrate the pixel dimensions to that of the SEM image	149
A-4	Import window for Amira 4.0.....	149
A-5	The AlignSlices procedure from Amira with windows.....	150
A-6	A series of cross-sectional SEM images import for alignment.....	150

A-7	The Shear procedure from Amira with windows.....	151
A-8	Amira properties window for the Sheared output module.....	151
A-9	The LabelField procedure from Amira with windows.....	152

LIST OF ABBREVIATIONS

AFL	Anode Functional Layer
CV	Cyclic Voltammetry (Voltammogram)
CVD	Chemical Vapor Deposition
DMC	Dimethyl Carbonate
EC	Ethylene Carbonate
EDS	Energy-dispersive X-ray Spectroscopy
FIB	Focused Ion Beam
HAADF	High-Angle Annular Dark-Field
IBM	Ion Beam-Mixing
LCM	Lanthanum Cobalt Manganate
LSCF	Lanthanum Strontium Cobalt Ferrite
OM	Optical Microscopy (Microscope)
PDMS	Poly(dimethylsiloxane)
PECVD	Plasma Enhanced Chemical Vapor Deposition
PVD	Physical Vapor Deposition
SAED	Selected-Area Electron Diffraction
SEM	Scanning Electron Microscopy (Microscope)
SCCM	Standard Cubic Centimeters per Minute
SOFC	Solid Oxide Fuel Cell
SRIM	The Stopping and Range of Ions in Matter
SS	Stainless Steel
STEM	Scanning Transmission Electron Microscopy (Microscope)
TPB	Triple Phase Boundary
TEM	Transmission Electron Microscopy (Microscope)

TRIM	Transport of Ions in Matter
VC	Vinylene Carbonate
XRD	X-Ray Diffraction
XTEM	Cross-sectional Transmission Electron Microscopy

Abstract of Dissertation Presented to the Graduate School
of the University of Florida in Partial Fulfillment of the
Requirements for the Degree of Doctor of Philosophy

ION BEAM-MIXED GERMANIUM AND SILICON LITHIUM ION BATTERY ANODES

By

Nicholas Vito

December 2013

Chair: Kevin S. Jones

Major: Materials Science and Engineering

Lithium ion batteries have now become a ubiquitous part of modern society as an energy storage device. Attractive due to the high energy density compared to competing battery technologies, interest in improving performance and lowering cost is high as the interest in electric vehicles increases. Improvements in the cathode, electrolyte, and anode chemistries must all take place to realize the full improvements of any one component. Germanium ($1,637 \text{ mA h g}^{-1}$) and silicon ($4,200 \text{ mA h g}^{-1}$) anode materials have received attention due to their high theoretical gravimetric capacities compared to the common carbon (372 mA h g^{-1}) anode. One major drawback of germanium and silicon electrodes is that to realize its full capacity, the electrode undergoes a volumetric expansion of up to 400%. This expansion will lead to premature failure of the battery due to loss of electrical contact and pulverization.

In this dissertation, ion implantation is investigated as a method to improve the adhesion of germanium and silicon thin films to a substrate. Ion implantation induces ion beam mixing at the anode current collector interface. As the amount of ion beam-mixing increases, improvements in the adhesion are identified in both the electrochemical performance of the cells

and the resulting fracture microstructures. Whereas an as-deposited cell may only last a few cycles at high current densities, the ion beam-mixed electrodes were able to maintain high capacities over 50 to 100 cycles. The thin film fractures into numerous independent islands on the substrate surface with decreasing size as the ion dose increases.

The use of ion beam-mixed templates for successive film growth is investigated to limit the need for MeV or higher implants. The benefits of ion implantation remain even when the thickness of the film is increased from 350 nm to 1,500 nm. Utilizing the superior performance of silicon electrodes implanted at a dose of 10^{16} Si⁺ cm⁻², the fracture characteristics were investigated as a function of current density. A combination of all the experimental results and known theory were used to develop a model to predict the fracture characteristics.

CHAPTER 1

INTRODUCTION

Through the advancement of modern electronics and the need for lightweight, mobile energy storage, rechargeable lithium ion batteries became ubiquitous in society over the past 20 years. While rechargeable lithium ion batteries are most established in portable electronics, the market capitalization for lithium ion batteries is expected to eclipse \$25 billion by 2017 due to emergence in potential markets such as wireless communication, electric vehicles, stationary storage, defense, and microchips [1]. Lithium ion batteries have become the flagship battery technology due to exceptional energy and power densities when compared to lead-acid, Ni-Cd, and Ni-MH technologies [2].

One promising market for lithium ion batteries is the development of electric vehicles, from both an environmental and security standpoint. In 2009, the US Energy Information Administration (EIA) found that fossil fuels are the source of about 99.5% of the energy consumed during transportation [3]. Fossil fuels are relatively inexpensive and have high energy densities but emit air pollutants and greenhouse gases, while convenient reserves are constrained by geographical and political barriers. Electric vehicles may still rely on fossil fuels indirectly since ~64% of electricity is supplied through fossil fuels such as coal, natural gases, or petroleum products as of 2001 [4]; however, the source of electricity generation is flexible as renewable energy technologies continue to advance.

1.1 Lithium Ion Batteries

Lithium metal was identified as an attractive energy storage material due to its high specific capacity ($3,862 \text{ mAh g}^{-1}$) and highly negative electrode potential (-3.04 V vs. standard hydrogen electrode) [5]. Due to many safety concerns, lithium metal has been replaced as an electrode by the less reactive lithium ion technology.

1.1.1 Road to Commercialization

Development of lithium based batteries began in the early 1970s with sulfur/lithium [6] and CF/lithium primary cells. In 1975 Sanyo commercialized the first lithium based primary cell based on MnO₂/lithium. As development of lithium-based secondary batteries progressed through the 1970s, it became evident that lithium metal posed safety hazards due to dendritic Li growth during cycling [7]. By the end of the decade, it was shown that batteries could be operated with lithium only in its ionic states, effectively eliminating safety hazards due to dendritic growth [8] [9]. While the ionic lithium greatly improved the safety of the batteries, cell potential was reduced since the insertion electrode has a higher redox potential than pure lithium. To offset the reduced cell potential, high potential transition metal oxides replaced previous cathode materials [10]. Two important breakthroughs during this time towards the lithium-ion chemistry was Goodenough's patent of LiCoO₂ as a transition metal oxide insertion cathode in 1980 [10], and patents by Ikeda (Sanyo 1981) and Basu (Bell 1982) on the graphite / lithium system in a nonaqueous solvent. These developments culminated with Sony introducing the first commercial battery based on carbon/LiCoO₂ in 1991, which became one of the most popular lithium ion chemistries for the next decade [11-14].

1.1.2 Lithium Ion Battery Chemistry

The typical structure and operation principles of a lithium-ion cell is represented in Figure 1-1. The electrochemically active components of the battery are the cathode, anode, and electrolyte. The separator is an inert, permeable membrane which exists to prevent contact and internal shorting between the cathode and anode. During charging, lithium is oxidized at the cathode and extracted into the electrolyte. At the anode, lithium is reduced and inserted into the anode structure. The reaction is reversed during discharging. Equations 1-1, 1-2, and 1-3 show the corresponding full and half-cell reactions for a LiCoO₂/C lithium-ion battery.





The electrolyte may be an aqueous or non-aqueous solution, polymer, or ceramic material. The role of the electrolyte is to facilitate the transport of Li between the anode and cathode, therefore high ionic conductivity is required. In order to prevent internal shorting, the electrical conductivity of the electrolyte must be negligible. Stability under the potentials of either electrode is also desired to prevent decomposition. Other concerns include toxicity, flammability, temperature range stability, and vapor pressure. Common electrolytes include lithium hexafluorophosphate (LiPF_6), lithium tetrafluoroborate (LiBF_4), lithium hexafluoroarsenate (LiAsF_6), and lithium bis(oxalate)borate (LiBOB) [15].

One important reaction that often occurs in batteries is the formation of the solid electrolyte interphase (SEI). The reactions at the electrode surface can involve the solvent, lithium salt, dissolved oxygen, or other contaminants [Scrosati 2002]. While the SEI layer provides an additional impedance within the cell, the passivation layer is useful to prevent further decomposition of the electrolyte. Additives with higher redox potentials, such as vinylene carbonate (VC), are often combined with electrolytes in order to sacrificially create the passivation layer [16].

The anode and cathode both have similar desired characteristics: high electronic conductivity, high ionic conductivity, high gravimetric capacity, reversibility, and structural integrity. The cathode and anode are defined within a cell as the material with the higher and lower redox potential with respect to lithium, respectively. Electrodes with poor electronic conductivity are often coated or otherwise combined with carbon to offset the detrimental quality at the expense of lower gravimetric capacity. In order to improve structural integrity and reaction kinetics, the electrodes are often designed with nano-sized features. Cathode

chemistries include LiCoO_2 , Li_2MnO_4 , LiFePO_4 , LiFeF_2 , S, and V_2O_5 [17]. Carbon has been the most commercially successful anode; however, other anode chemistries under investigation are TiO_2 -(B), Sn, Ge, and Si [18].

In a lithium ion battery, the capacity of an electrode is directly related to amount of lithium it can react with or store. In order to isolate extrinsic properties of the electrode, gravimetric capacity is widely reported. The theoretical gravimetric capacity of an electrode is determined by the following equation,

$$C_S = \frac{nF}{zM} \quad (1-4)$$

where C_S is the gravimetric capacity, n is the stoichiometric quantity of electrons, F is Faraday's constant, z is the stoichiometric quantity of the electrode species, and M is the molar mass of the electrode species. Therefore the gravimetric capacity of an electrode can be improved by either transitioning to lighter materials or exploring materials that will liberate more electrons per mole.

1.2 Anode Materials for Lithium Ion Batteries

Carbon based anodes have dominated the marketplace since they are inexpensive and not limited by current battery chemistries. Since only one lithium ion and electron can be accommodated by six carbon atoms, the theoretical gravimetric capacity of a carbon electrode is 372 milliamper-hours per gram (mAhg^{-1}). Germanium, silicon, and tin are all from the same group of the periodic table as carbon, but have been shown to react to a Li_{22}M_5 ($M = \text{Ge}, \text{Si}, \text{or Sn}$) stoichiometry. With 4.4 lithium atoms being accommodated by 1 host atom, these alloys show promise as high capacity anodes.

Germanium is often overlooked as an anode material due to its high cost; however, germanium has a gravimetric capacity of about $1,600 \text{ mAhg}^{-1}$ at $\text{Li}_{22}\text{Ge}_5$, which is about four times higher than that of carbon. A downside to the high gravimetric capacity is that the lithium

uptake causes a large volume expansion of ~370% [19]. The volumetric expansion leads to pulverization and loss of electrical contact during cycling, which plagues germanium and similar alloys [20].

Silicon is a promising anode material because it has the highest known theoretical gravimetric and volumetric capacity for the lithium ion chemistry at $4,200 \text{ mAhg}^{-1}$ for the $\text{Li}_{22}\text{Si}_5$ phase. Silicon is also the second most abundant element in the Earth's crust and is widely used in the semiconductor industry. However, silicon also suffers from a large volume expansion of ~400% [21, 22]. The expected delamination process for both germanium and silicon is shown in Figure 1-2. In order to increase the contact area between the electrode and substrate, roughening techniques such as using sandpaper were established immediately for both germanium and silicon thin film electrodes [23, 24]. A 50 nm thick amorphous silicon electrode deposited by low pressure chemical vapor deposition lost all its capacity by cycle fifty when undergoing a full charge cycle but was able to maintain stable capacities corresponding to a $3,200 \text{ mAh g}^{-1}$ discharge level for one hundred cycles and $1,300 \text{ mAh g}^{-1}$ for two hundred cycles [25]. Thicker films of up to 523 nm were grown by magnetron sputtering on a copper substrate and cycled at a C/2 rate. The 121 nm and 312 nm thick films showed a stable capacity of ~3,500 mAh g^{-1} over twenty-five cycles while the 523 nm thick film capacity fell under 1,000 mAh g^{-1} by cycle twenty-five [26]. While thin film electrodes have shown potential, many variables are changed between experiments: substrate, deposition technique, surface cleaning, roughness, thickness, cycling rate, and potential window. While electrode failure was generally attributed to fracture, ex-situ evidence was not always provided.

Improvements for germanium and silicon electrodes has mostly involved a variety of nanostructures to help mitigate the stresses from the insertion and extraction of lithium in recent years. Green et al. investigated nanopillars of silicon which showed no cracking due to cycling over 50 cycles [27]. Germanium and silicon nanowires show good rate capabilities and avoid

pulverization [19, 28]. Zero dimensional hollow germanium spheres attached to a 3D porous germanium assembly and revealed that long-range order of pores and regularity of pore wall thicknesses are key factors for reversible capacity retention [29]. Song et al. investigated hollow nanowires, which better accommodated the volumetric expansion [30].

Silicon and germanium-carbon composites were also investigated to improve electrical conductivity at the expense of a drop in gravimetric capacities due to partial replacement of the silicon by carbon. Many early researchers investigated the composite where the reversible capacities were around $1,000 \text{ mAhg}^{-1}$ or less [31-34]. Recently carbon-coated nanowires, carbon-silicon core-shell nanowires, graphene and fullerene coated anodes, and carbon nanotube composites have all been investigated [35-41].

Few investigations have focused on the interface between the electrode and current collector. Grinding the surface of a copper current collector with $15 \mu\text{m}$ grain sandpaper resulted in doubling the accessible gravimetric capacity of a silicon electrode [24]. An elastomeric poly(dimethylsiloxane) (PDMS) layer acted as a flexible substrate with a gold current collector which successfully prevented deformation of the silicon electrode [42]. A drawback to the PDMS technique is that a large amount of inactive material is added to the battery, lowering the total gravimetric capacity. One promising technique is to use ion beam-mixing (IBM) to improve the adhesion of an electrode to a current collector. It was shown that a $10^{16} \text{ Ge}^+ \text{ cm}^{-2}$ implant into a germanium electrode greatly improve capacity retention [43].

1.3 Ion Beam Mixing

Ion implantation is a common technique used in semiconductor manufacturing as a non-equilibrium method to introduce dopant species to a semiconductor, but a variety of applications for ion beam-mixing have emerged over the past 30 years. Ion beam-mixing has been shown to be able to produce difficult to replicate structures [44]. Ion beam-mixing has also been employed to improve the wear and corrosion resistance of certain metals [45]. Mixing of

semiconductor and metals to form electrical contacts is another application [46]. One interesting application of ion beam-mixing in relation to lithium ion battery electrodes, is the improvement in adhesion across an interface.

1.3.1 Ion Implantation

Ion implantation describes a process where ions are accelerated and bombard a surface of interest. Four important factors associated with ion implantation are the accelerating voltage, implant dose (or fluence), dose rate (or ion flux), and ionic species. With other factors being constant, the accelerating voltage primarily determines the projected range (depth) of the implant species into the substrate. The implant dose describes the quantity of implanted species into the substrate and is generally expressed as the number of ionic species per square centimeter. The dose rate describes how quickly the dose is implanted into the substrate, where a faster rate may lead to more damage. The ionic species affects the chemical, electrical, and structural properties of the substrate to varying degrees.

1.3.2 Concept of Ion Beam Mixing

Ion beam mixing is an ion implantation process where the goal is the physical mixing of phases or interfaces, rather than the electrical or chemical activation of a dopant species. Ion beam-mixing can be described by three primary processes: ballistic mixing, thermolisation mixing, and diffusion processes.

Ballistic mixing is caused as a result of the nuclear stopping mechanism within the substrate. This type of mixing can be further separated into two parts, initial knocked-on mixing and cascade mixing. The implanted ion elastically collides with the initially knocked-on atom and transfers a large amount of energy which displaces the knocked-on atom. This type of mixing is biased in the implant direction and determines the maximum extent of intermixing. As either the ionic species or knocked-on atom loses more energy due to electronic or nuclear stopping, a collision cascade occurs with the remaining energy lost primarily by nuclear

stopping. While the energy transferred and displacements are less per collision, atoms may collide thousands of times before coming to rest. An illustration of the damage from an implant is shown in Figure 1-3.

The accumulation of the collisions and displacements lead to a defective structure with a high energy state which leads to thermolisation mixing. During thermolisation, the substrate and implanted atoms experience a short range diffusion of a few atomic spacings where the atoms fall into a low energy configuration. The end result may lead to a crystalline or amorphous structure of a stable or metastable alloy. If the ion beam mixing event has enough thermal activation, longer range diffusion may progress where structures can form in a more stable state.

Some general characteristics of ion beam-mixing is that significant ion penetration has to occur to mixing to proceed. The mixed profile is generally Gaussian in shape. The amount of mixing is proportional to the implanted dose. The amount of mixing is generally independent of the dose rate. The amount of mixing is proportional to the energy density [47].

1.3.3 Adhesion Improvements due to Ion Beam Mixing

There have been several studies relating ion beam mixing to adhesion improvements, although measurement methods and reasons for improved adhesion vary between experiments. The delamination event between the film and substrate has been expressed as a stress, surface energy, pull-off force, and qualitatively in terms of deformation resistance. The following is a review of previous studies relating the effects of ion beam mixing.

In 1992, Pawel et al. investigated the role of chemical species as adhesion relates to ion beam-mixing. Chromium, nickel, and iron were implanted through an iron film to promote mixing with an alumina substrate. Since the mass of the ions are similar, the dose rate, dose, and energy density were effectively kept constant. Their results show that a chromium implant

improved adhesion of the iron onto the alumina with no failure up to a 40 MPa stress, while the as-deposited film had ~60% failure rate. Meanwhile nickel implants did not improve adhesion, where the failure rate up to 40 MPa was ~75%. Iron implants resulted in a modest improvement with only ~50% failing up to 40 MPa [48].

In 1997, Chang et al. investigated the improvement in adhesion between a copper film and polyimide substrate due to ion beam mixing of nitrogen and argon species. The adhesion of the film to the substrate was measured by a pull-off test. The virgin film can support a critical load of 2.5 g mm^{-1} , while the ion beam-mixed film implanted with $10^{15} \text{ N}^+ \text{ cm}^{-2}$ was able to support a critical load of $\sim 90 \text{ g mm}^{-1}$. Increasing the dose further did not improve the adhesion as the quantity of amide, tertiary amine, and pyridine-like features varied, altering the surface chemistry. Nitrogen was also shown to be more effective than argon in this case [49].

In 2002, Guzman et al. investigated the improvement in adhesion between gold on glass and gold on carbon on glass. In both cases, a layer of carbon was deposited over the gold to reduce sputtering loss at the surface. The films were implanted with xenon, and showed significant adhesion improvement, particularly in the case of gold on glass. Scratching the surface with a force of 1 N was able to chip and delaminate the film of the untreated film, while the implanted film was able to sustain forces of at least 40 N [50].

In 2005, Hong et al. investigated the copper on polyimide chemistry with a different series of implants. Here helium, neon, argon, and xenon were implanted at a $2.0 \times 10^{17} \text{ cm}^{-2}$ dose during growth to provide ion beam-mixing. Whereas the initial untreated adhesion was $\sim 10 \text{ N m}^{-1}$, the implanted adhesion was over 250 N m^{-1} for all species, with a xenon implant achieving at 350 N m^{-1} . The projected range was also varied for the argon implant by varying the ion energy, showing a region of improved adhesion with a lack of improve at too low or high of energy. This characteristic is likely related to the location of the projected range at the interface [51].

In 2013, Sunmog Yeo investigated the adhesion of iron oxide and copper coatings on polyphenylene sulfide. A qualitative improvement in adhesion due to ion beam-mixing was determined by a tape peel-off test, where both of the untreated films were removed by a piece of tape. Using a high frequency oscillator, Yeo determined that the adhesion for the iron oxide was 27.2 kPa while the adhesion is 18.6 kPa; however, no comparison was made to the untreated samples [52].

Also in 2013, Rudawski et al. investigated the improvement in adhesion and lithium ion electrode performance from ion beam-mixed germanium on a nickel-iron substrate. As with Yeo's research, the adhesion was qualitatively compared with a tape test showing that the untreated film peeled off whereas the implanted film did not. Nanoindentation results between the two samples showed a discontinuity at about 150 nm (the film thickness was 140 nm) for the untreated film while the implanted film had no feature. It was suggested that the discontinuity corresponded to the delamination of the film. However, the implanted film showed a remarkable improvement over the untreated film in electrochemical testing with hardly any capacity fade over 20 cycles, while the untreated film failed almost immediately [43].

While ion beam-mixing may improve adhesion in many different systems, the mechanical testing of the films is often overlooked or not relevant to the experiment objective. Results vary in how promising ion beam-mixing is to improve adhesion, with many factors to consider. The most promising result deals with ion implantation of a germanium electrode for a lithium ion battery.

1.4 Objectives and Overview

As described throughout Chapter 1, the current state of lithium ion batteries needs to be improved to meet the demands of high energy and power density applications. While improvement of the cathode material is critical to achieve real gains in concert with improvements in anode performance, this research will focus on anode materials.

The goal of this research is to characterize the effect of ion beam-mixing as it relates to changes in electrochemical performance, adhesion, and mechanical deformation of the silicon or germanium thin film electrodes. The findings of this research may not only improve the knowledge of silicon and germanium thin film electrode, but be applied to other battery chemistries or microstructures to augment the novel electrodes of the future.

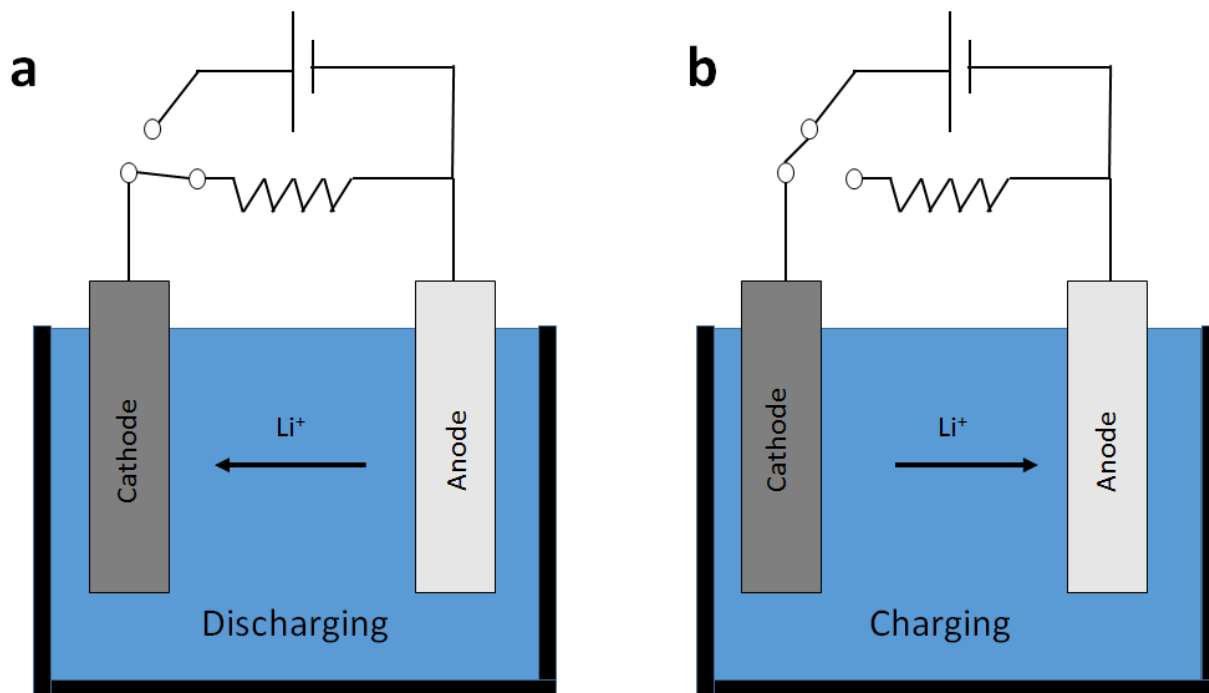


Figure 1-1. A schematic view of the basic battery components and operation during (a) discharging and (b) charging.

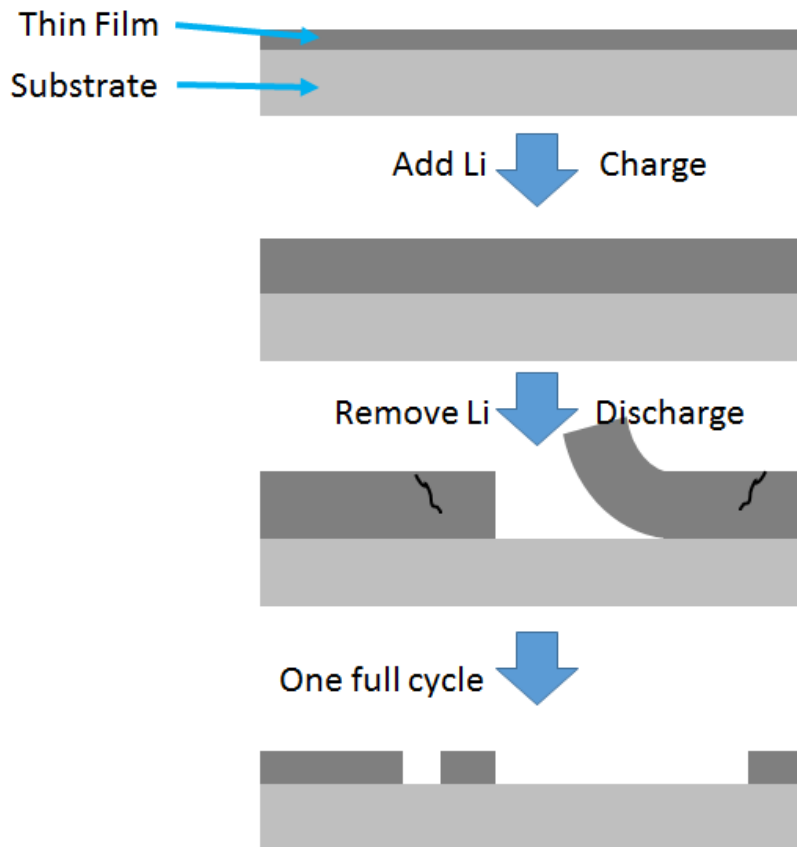


Figure 1-2. Illustration of delamination mechanism for germanium and silicon lithium ion battery electrodes during cycling.

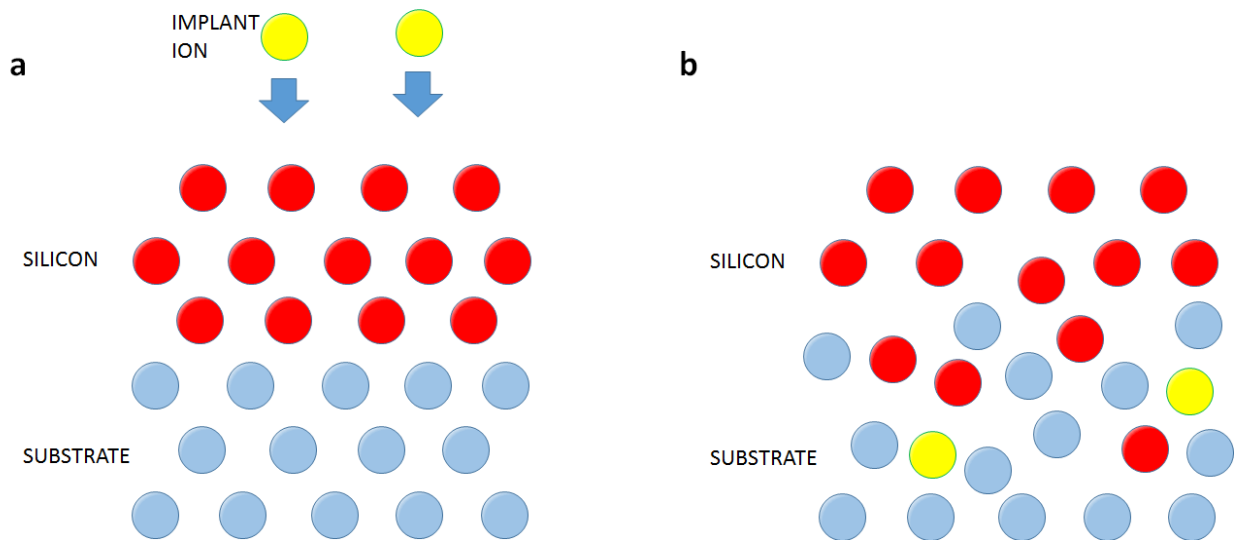


Figure 1-3. Illustration of damage from ion implantation comparing the interface between silicon and a substrate (a) before implant and (b) after implant.

CHAPTER 2

EXPERIMENTAL METHODS

This chapter will review the techniques commonly used or referenced throughout this work. The chapter progresses chronologically in the experiment process starting with the ion implantation of thin films, creation of an electrochemical pouch cell, ex-situ analysis of the electrochemical cell, and ending with the methodology for fracture analysis.

2.1 Methodology for Ion Beam-Mixing

When an ion enters a specimen, the ion experiences energy loss primarily by two mechanisms: electronic and nuclear stopping. Electronic stopping describes an energy loss rate due to inelastic collisions of the incident ion interacting with electrons. An analytical description of interactions or sources of electronic stopping is complex due to a variety of mechanisms that contribute, such as Coulomb ionization, excitation of electrons in the stopping medium or implanted ion, electron exchange, and effective charge. An empirical approach shows that the electronic stopping power scales proportionally with the ion velocity. For ionic velocities greater than the mean orbital velocity of their internal electrons, the ion is considered completely stripped of electrons. The electronic stopping power now decreases with increasing ion velocity since the interaction time of the two particles is so short. In either electronic stopping region, deflections in the path of the incident ion is negligible.

At lower velocities, interactions between the incident ion and nucleus of the stopping medium begin to dominate. These interactions are elastic and often result in atomic displacements in the stopping medium, leading to a collision cascade which is vital for ion beam mixing. Interactions between the ion and host atom are unique for each pair of elements and with the orbital structure of each contributing the interatomic potential. In order to approximate the interatomic potential between any pair of elements, a universal screening was empirically found to be,

$$\mathbf{a}_U = \frac{0.8853\mathbf{a}_0}{Z_1^{0.23} + Z_2^{0.23}} \quad (2-1)$$

where \mathbf{a}_U is the universal screening parameter, \mathbf{a}_0 is the bohr radius, Z_1 refers to the atomic mass of the incident ion, and Z_2 refers to the atomic mass of the stopping medium. With a universal screening length, a universal interatomic potential was developed:

$$\Phi_U(\mathbf{x}) = 0.1818e^{-3.2\mathbf{x}} + 0.5099e^{-0.9423\mathbf{x}} + 0.2802e^{-0.4028\mathbf{x}} + 0.2817e^{-0.2016\mathbf{x}} \quad (2-2)$$

where Φ_U is the universal screening potential and \mathbf{x} is the separation between the ion and host atom normalized by the universal screening length. The empirical function was reviewed by comparing 106 experimentally determined potentials with theoretical ones [53]. The universal screening potential can then be used to calculate the deflection of the incident ion by

$$\Theta = \pi - 2 \int_{x_0}^{\infty} \frac{pdx}{a_U x^2 \sqrt{1 - \frac{Z_1 Z_2 e^2 \Phi_U(x)}{a_U x E_c} - \frac{p^2}{a_U^2 x^2}}} \quad (2-3)$$

where Θ is the scattering angle of deflection, p is the impact parameter which is proportional to the angular momentum, e is the elemental charge of an electron, and E_c is center of mass energy.

2.1.1 Monte-Carlo Ion Simulation

In order to determine an appropriate accelerating voltage for ion beam-mixing at an interface, a software package titled the Stopping and Range of Ions in Matter (SRIM) was used. An important module in the SRIM package is Transport of Ions in Matter (TRIM). TRIM uses a Monte Carlo approach following the history of each individual implanted ion or displaced atom until either the falls below a minimum energy threshold or exits the sample dimensions. Two approximations are made in order to speed up simulation times: a free-flight path is randomly chosen for high energy particles and the deflection from nuclear collisions is approximated by the Magic Formula to avoid evaluation of the integral in Equation 2-3. While electronic energy

loss is computed over the free flight path, negligible or glancing nuclear interactions are avoided where the energy transfer is small but computationally intensive. The Magic Formula is defined as,

$$\cos \Theta = \frac{1}{a_U} \left(\frac{\rho + \rho + \delta}{\rho + r_0} \right) \quad (2-4)$$

where ρ is the sum of the radii of curvatures at closest approach, r_0 is the separation distance at closest approach, and δ is the sum of small correction factors for each particle. The correction factor δ is such that Equation 2-4 reproduces Rutherford scattering as the length normalized center of mass energy becomes sufficiently large [54, 55]. Despite the approximations, the TRIM code matches 69% of experimental data across all ion/substrate combinations to within a 5% error and 86% of the data within a 10% error [56]. To promote ion beam-mixing, an implant energy is chosen to place the projected range of the implant at the interface between the film and substrate, shown in Figure 2-1.

2.1.2 Equipment for Ion Implantation

The equipment used for ion implantation was a National Electrostatics Corporation (NEC) model 5SDH-4 with a SNICS sputter ion source at Australia National University. A schematic of the system is shown in Figure 2-2. The ion source is created through a sputtering process where cesium atoms are ionized through heating and accelerated into the target cathode. The sputtered ions are negatively charged either because of preferential energetics or because the ion picks up electrons from the condensed cesium. An extractor accelerates the anions through a magnetic field where the ions are mass analyzed to remove unwanted species. The anions are then accelerated to a terminal where a nitrogen gas is introduced. The nitrogen gas strips away electrons from the anions, charging them positively. The positive ions are now accelerated away from the terminal through another mass analyzed magnetic field and into the sample surface.

2.2 Pouch Cell Assembly

The pouch cell is comprised of aluminum laminate sheets, stainless steel (SS) contacts, a cathode, an anode, a separator, Kapton® HN polyimide tape with silicone adhesive, and an electrolyte. A schematic of the pouch cell design and completed pouch cell is shown in Figure 2-3. The aluminum laminate sheets are heat sealed together to form the body of the pouch. The laminate forms the heat sealed bond, while the aluminum acts as an environmental barrier, particularly as a vapor barrier. The first heat seal occurs at the stainless steel contacts, which are positioned in a “V” shape so the electrodes can lay over one another. A polypropylene, Celgard model C480 (Celgard Inc., USA), separator is placed between the two contacts and positioned to prevent a short circuit. The separator is held in place with a piece of Kapton® tape to prevent movement during handling. The cathode material, in this case a thin silicon or germanium film on a metal substrate, is then weighed and taped to the angled stainless steel contact.

2.2.1 Windowed Pouch Cell

Figure 2-4 shows an alternative pouch cell design that was used to observe the working electrode surface. In this design a hole was made in the pouch, lithium, and separator in line with each other to allow visibility of the electrode surface. The hole in the pouch was then sealed by epoxy and a thin glass cover slide. The epoxy was allowed to cure before progressing to the next step of the pouch cell preparation within the glove box. The rest of the cell was designed similarly to the standard pouch cell, with care to avoid blocking visibility.

2.2.2 Electrode Mass Calculation

The mass of the active thin film electrode is estimated from the areal density and mass of its substrate. Samples of either substrate were cut into various shapes and sizes in order to determine the areal mass density. The area and mass of each substrate sample was measured shown in Figure 2-5. The thickness of the thin films was confirmed via transmission electron

microscopy and the density of film was found in literature from similar films. The density is estimated from reported values. The total mass of the electrode films ranged between 10 – 20 μg .

2.2.3 Glove Box

An MBraun UniLab glove box with an argon atmosphere was utilized to provide an inert environment for the remaining cell construction. Generally, the water vapor level in the glove box atmosphere was at or below one part per million since the electrolyte and anode, in this case lithium, are air-sensitive. A lithium ribbon was partitioned into pieces slightly larger in area than the cathode. The surface of the lithium was scraped away to remove the passivated surface before being taped to the other stainless steel contact. Two of the remaining three side of the pouch are sealed within the glove box using another heat sealer. As the pouch is allowed to cool, a solution of 1M LiPF_6 in 1:1 DMC:EC solvent is flooded into the cell. Care is taken to ensure the electrodes are submerged in the electrolyte, and the final side of the pouch is sealed while the pouch is tilted to prevent spilling.

2.3 Electrochemical Characterization

The following techniques were used to evaluate the electrochemical performance of the fabricated electrodes. Both techniques were performed using an Arbin BT2000 battery tester. The test equipment has 16 channels on the primary device and an additional 8 channels on the auxillary device, allowing for simultaneous testing of 24 batteries.

2.3.1 Galvanostatic Cycling

Under galvanostatic testing conditions, a constant current is maintained across the electrochemical cell during the discharge and charge cycles. The magnitude of the current is the same for both cycles, but the direction of the current is reversed. The magnitude of the current is determined based on the working electrode mass, calculated in section 2.2.2. The

capacity of each cycle can be conveniently calculated by a product of the cycling time and current.

2.3.2 Cyclic Voltammetry

Cyclic voltammetry (CV) is a technique that provides information about reactions occurring in or on an electrode. A constant voltage step rate is applied across the electrochemical cell to measure the current response. Spikes in the current indicate that an electrochemical reaction has taken place at the specified voltage.

2.4 Material Characterization

The following techniques were used to characterize the microstructure and chemical composition of the silicon and germanium electrodes before and after all experiments.

2.4.1 Optical Microscopy

Optical microscopy (OM) is a light imaging technique where one or more lenses produce a magnified image of an object. OM has a variety of applications including identifying phases, homogeneity, morphology, and refractive indices with resolutions typically on the order of a few hundred nanometers to several micrometers. A schematic of an optical microscope is shown in Figure 2-6. The resolution of a microscope is bounded by a diffraction limit and can be described by the Rayleigh criterion

$$d = \frac{1.22\lambda}{n_{\text{obj}} \sin \theta_{\text{obj}} + n_{\text{con}} \sin \theta_{\text{con}}} \quad (2-5)$$

where λ is the wavelength of the light source, n_{obj} and n_{con} are the refractive indices of the medium between the respective lenses and specimen, and θ_{obj} and θ_{con} are the half-angles for the maximum cone of light that can enter or exit the respective lens. The product of the refractive index and sine of the collection half-angle is also referred to as a numerical aperture (N. A.). Other sources of distortion in image quality can arise from alignment and lens aberrations. Two types of aberrations are chromatic and spherical aberrations. Chromatic

aberration is defined by the failure of a lens to focus different wavelengths of light to the same point, while spherical aberrations is similarly defined as the failure of a lens to focus incident light from different radial locations to the same point. Both types of aberrations are illustrated in Figure 2-7.

Two common imaging techniques used in microscopy are bright field and dark field microscopy. Under bright field conditions, contrast in the image originates from absorbance of light by the specimen. Under dark field illumination, part of the illuminating beam is blocked in order to view only the scattered or diffracted light. Dark field imaging provides better contrast and structural details than bright field imaging, at the expense of a lower intensity of collected light. Both illumination conditions are shown in Figure 2-8. In this experiment, a reflective Olympus light microscope was utilized under bright field conditions.

2.4.2 Scanning Electron Microscopy

Scanning Electron Microscopy (SEM) is an electron imaging technique where a beam of electrons is scanned across a sample surface provide illumination. Electron microscopy provides a large advantage over light microscopy in terms of resolution since the wavelength of the accelerated electrons is much smaller than that of visible light according the relationship in Equation 2-5. The wavelength of any particle can be calculated by

$$\lambda = \frac{h}{\sqrt{2m_0eV}} \quad (2-6)$$

where h is Planck's constant, m_0 is the relativistic mass of the particle, e is the elementary charge, and V is the potential difference between the source and specimen. For an electron accelerated across a potential difference of 10 kV, the wavelength is approximately 12 pm, much smaller than the range of 400 to 700 nm for visible light. Despite the small wavelength, aberrations and even magnetic noise from the thermal activation of currents in the metallic components provide barriers to the theoretical limit [57-59].

Outside of costlier instrumentation, disadvantages of SEM can arise from a more involved sample considerations. Although environmental SEMs exist, specimens must generally be stable under a vacuum since it is required for electrons to have a large mean free path, as opposed to interacting and scattering from gas particles. Due to the charge of an electron, samples should be electrically conductive to prevent an accumulation of charge at the specimen surface which will interact with the incoming beam. Samples are often grounded by means of a conductive carbon tape or a thin film coating of carbon, gold, or other metals.

Two common types of electron detection methods are backscatter and secondary electron detection. Backscattered electrons (BSE) interact with the specimen atoms through an elastic collision. Since the probability of an elastic collision event scales with the mass of the specimen atom, BSE images provide contrast between regions of differing atomic mass. When an electron interacts inelastically with a specimen atom, there is a local ionization. An electron is emitted as radiation when returning to the ground state. The term secondary electron is due to the fact that the electron is collected as radiation and not from the primary incident beam. Secondary electrons originating near the specimen have a higher probability of emission from the surface than those formed deeper into the specimen, so substantial information about the topography of the specimen can be obtained using a secondary electron detector (SED).

SEM images were obtained using one of two microscopes: the SEM column of a FEI dual-beam Strata DB235 focused ion beam or a JOEL SEM 6400. Both instruments are resources at the Major Analytical Instrumentation Center (MAIC) at the University of Florida.

2.4.3 Focused Ion Beam

Focused ion beam (FIB) microscopy is analogous to scanning electron microscopy except that an ionized particle is accelerated rather than an electron. While imaging a surface with ions is possible, the heavier mass of the ion in comparison to an electron may cause significant damage to the specimen surface. The damage is utilized to create structures on the

specimen surface through ablation. Site-specific ablation revolutionized sample preparation for cross-sectional transmission electron microscopy (XTEM), where electron transparent samples can be milled from a specimen.

In preparing a XTEM sample using a FIB, the first step is to deposit a thin layer of carbon on the surface as a sacrificial layer to protect the specimen surface during alignment processes. Once the site of interest and beams are properly aligned, a needle is inserted near the site of interest emitting an organometallic platinum gas. The precursor gas interacts with ion beam and deposits a platinum layer on the specimen surface [60]. The protective platinum layer is a protective mask for the subsequent milling. The XTEM sample is thinned by incrementally milling towards the site of interest from opposite sides. Once the XTEM thickness approaches one micrometer, the stage is tilted so the ion beam is no incident to the cross-sectional surface and the specimen is cut free at the base and one side. A diagram of the process is shown in Figure 2-9. At this point, the XTEM sample may be further thinned for an ex-situ transfer to a sample grid, or transferred via a micromanipulator to a sample grid in-situ.

The in-situ transfer process utilizes an OmniProbe micromanipulator to mechanically transfer the XTEM sample by bonding the surfaces together by deposition of a platinum layer. The XTEM sample is then adhered to the sample holder via the same process, albeit on the other side of the XTEM sample. Once adhered, the OmniProbe micromanipulator is freed from the XTEM sample through ablation of the XTEM sample and platinum bond. At this point, thinning of the sample proceeds by incrementally milling from opposite sides in order to achieve a thickness of 100 nm or less. The final step is to remove damage to the surface parallel to the beam by milling at a low accelerating voltage [61].

The FIB used in this study was a FEI dual-beam Strata DB235 FIB as a resource of MAIC. The FIB stage is able to tilt between -10 and 56° , with the electron and ion beams separated by an angle of 52° . XTEM samples were generally milled to dimensions of

approximately 10 μm x 2 μm x 100 nm. The protective platinum layer was deposited to the dimensions of 10 μm x 1 μm x 2 μm using a 300 pA aperture. The XTEM structure was milled at a 30 kV accelerating voltage using a gallium source at currents ranging between 100 – 5,000 pA. As the sample was thinned, a 4° off-axis tilt from either side was applied to the sample to preserve the platinum layer. The cleaning step involved stepping down the accelerating voltage to 7 kV and using a 300 pA aperture.

2.4.4 Transmission Electron Microscopy

Whereas SEM collects information about a specimen through reflected electrons, transmission electron microscopy (TEM) collects information about a specimen through transmitted electrons. Since electrons travel through a specimen, structural information such as crystal structure, lattice spacing, and composition can be extracted due to the sample dimensions for electron transparency. The beam alignment for bright field TEM is such that the electron beam is parallel and illuminates the entire area of interest simultaneously.

Another feature often included with a transmission electron microscope is the ability to perform scanning transmission electron microscopy (STEM). With STEM, the electron beam is converged to a point on the specimen surface and scanned across the area of interest, similar to a scanning electron microscope. Also like SEM, since the beam position is known while scanning, site specific chemical analysis by either energy dispersive x-ray spectroscopy (EDS) or electron energy loss spectroscopy (EELS) can easily be performed with the appropriate detectors.

TEM and STEM images were obtained using one of two microscopes: a JOEL 2010F TEM or a JOEL ARM-200F. The JOEL 2010F is a resource of MAIC. The JOEL ARM-200F is a resource of the National High Magnetic Field Laboratory (NHMFL) at Florida State University. The JOEL ARM-200F has additional lensing installed to correct for spherical aberration.

2.4.5 Energy Dispersive X-Ray Spectroscopy

Energy dispersive x-ray spectroscopy (EDS) can be used to characterize the chemical composition of a specific region on a sample through radiated x-rays. When a high energy source, in this case an electron beam, interacts with the sample, electrons may be excited to higher energy electron shells. Electron shells are labeled K, L, M, N, O, P, and Q where the ground state configuration is related to each row in the periodic table. Each element has a unique energy signature based on the energy differences between the electron shells. The radiation is labeled by the destination shell with a Greek letter denoting the position of the source shell. For example, radiation emitted from an electron dropping from the M shell to the K shell is labeled as $K\beta$ radiation. Within each shell, differences in binding energy can be additionally indexed by a number.

EDS was performed on the JOEL SEM 6400 and JOEL TEM 2010F at MAIC, along with the JOEL ARM-200F at NHMFL. Although the probe size of a TEM is smaller than an SEM, the most significant gain in EDS resolution using a TEM is due to the sample dimensions. Since the TEM sample needs to be electron transparent, the additional interaction volume from the characteristic tear drop shape is avoided.

2.4.6 Selected Area Electron Diffraction

Selected area electron diffraction (SAED) is a site specific diffraction technique used to extract crystallographic information. The back focal plane allocates portions of the transmitted, diffracted beam at different angular positions. The back focal plane becomes the new object plane where those angular positions map out the reciprocal lattice structure. If the specimen is a single crystal, the reciprocal lattice contains an arrangement of discrete points. A polycrystalline specimen will show an arrangement of points in a ring around the transmitted beam. An amorphous specimen shows a diffuse pattern since there is no preferred scattering direction.

SAED was performed on the JOEL TEM 2010F at MAIC.

2.4.7 Nanoindentation

Nanoindentation is a method of probing mechanical properties from a small volume of the specimen. Traditionally indentation experiments required optical or other microscopy techniques to evaluate the area of the impression for calculation of mechanical properties. Through developments of a continuous measurement system, confirmation through microscopy was no longer required and indentations were able to scale down to the nanometer range. The primary mechanical property that is measured through indentation is the hardness of a material. Hardness is defined the resistance to deformation and is related to the yield strength of a material. The hardness of a material can be calculated through,

$$H = \frac{P_{\max}}{A_P} \quad (2-7)$$

where P_{\max} is the maximum applied load and A_P is the projected area of the residual impression. To avoid imaging nano-sized impressions, in 1992 Oliver and Pharr established techniques used in most nanoindenters today [62]. Using Equation 2-7, a calibration sample is used to calibrate and determine the area function of the tip,

$$A_P = f(h_c) \quad (2-8)$$

where h_c is the contact depth. The contact depth is not equal to the depth at maximum load since there are contributions from both elastic and inelastic deformation in the sample while loading, as shown in Figure 2-10. An elastic response dominates during unloading. The contact stiffness, S , is defined by the change in load per change in depth for the upper part of the unloading curve. Extrapolating a line based on the contact stiffness allows the contact depth to be estimated by,

$$h_c = \epsilon \frac{P_{\max}}{S} \quad (2-9)$$

where ϵ is a fitting parameter based on the indenter geometry. The reduced modulus, E^* , can also be calculated through a relationship with the contact stiffness and contact area by,

$$E^* = \frac{S}{2\beta} \sqrt{\frac{\pi}{A_P}} \quad (2-10)$$

where β is another fitting parameter based on the indenter geometry. The elastic modulus of the specimen can then be derived from the reduced modulus by,

$$\frac{1}{E^*} = \frac{1-\nu_i^2}{E_i} + \frac{1-\nu_m^2}{E_m} \quad (2-11)$$

where ν_s and ν_i are Poisson's ratio for the specimen and indenter, respectively.

Although nanoindentation techniques have been developed to avoid the need for microscopy, with the help of microscopy the fracture toughness of a material can also be determined through nanoindentation. The fracture event can be identified during loading as a "pop-in" event, where the additional penetration does not increase the load. Chen et al. developed a W_r -dp method where the energy related to the fracture can be extracted from the pop-in event [63]. Once the fracture energy is known, the fracture toughness can be calculated as:

$$K_{IC} = \sqrt{\frac{EU_f}{2\pi N h a (1-\nu^2)}} \quad (2-12)$$

where a_L is the crack length, h is the film thickness, N is the number of chips or cracks, and U_f is the fracture energy. The crack length and number of chips or cracks are determined using microscopy.

In this experiment, a Hysitron Triboindenter was utilized for nanoindentation experiments. The tip used was a diamond cube corner with an effective radius of 40 nm. The diamond tip has an elastic modulus of 1140 GPa and Poisson's ratio of 0.07. A 3-axis motor controlled stage allows for close proximity indents. The stage is vibrationally isolated within an

acoustic enclosure passively by springs and actively by electro-dynamic transducers. The TriboScope transducer has a force resolution of 1 nN, a displacement resolution of 40 pm, and a noise floor of 200 pm.

2.5 Fracture Analysis

Knowledge of the mechanism of failure and mechanical properties of thin films deposited on substrates is essential in modern society. The fundamental processes resulting in thin film cracking is not unlike cracking in bulk materials counterparts, except there is an emphasis on the adhesive strength between the film substrate. Cracks formed at the exposed surface of the thin film may either propagate through into the substrate, become arrested at the interface, or deflect to propagate along the interface in any number of directions. Three failure modes that will be emphasized in this work are buckling, through-thickness cracking, and debonding. Buckling is a failure mode from a compressive stress where the film remains continuous but a crack propagates along the interface between the thin film and substrate. Through-thickness cracking is a failure mode from a tensile stress where the film remains in contact with the substrate, but interfaces are formed when a crack propagates through the thickness of the film. Debonding is a failure mechanisms that can include compressive and tensile histories where a region of the film is fragmented from the both the substrate and itself. The work of adhesion across an interface was described in 1869 by Dupre as,

$$W_{ad} = \gamma_s + \gamma_f - \gamma_{sf} \quad (2-13)$$

where a γ_s , γ_f , and γ_{sf} define the surface energies between the substrate and a free surface, the film and a free surface, and between the substrate and the film.

Stresses in the thin film may arise mechanically from an external load, thermally, or intrinsically. The thermal and intrinsic stresses are commonly referred to as residual stresses. Intrinsic stresses may arise from deposition methodology, film morphology, or non-thermal film

treatments. Thermal stresses arise from differences in the coefficients of thermal expansion (CTE) between the film and substrate.

2.5.1 Electrode Cracking

During lithiation the silicon and germanium electrodes would experience a large volumetric expansion as explained in section 1.2. Since the film is constrained by the substrate, an in-plane compressive stress develops since there is only one free surface for expansion at the top of the film. When the polarities of the electrodes are switched and current flows in the opposite direction, lithium extraction from the electrode leads to an in-plane tensile stress and often through-thickness cracking. Graetz showed that extremely thin films may avoid cracking since the film thickness is below the critical crack size [64]:

$$a_c = \frac{2K_{IC}^2}{\pi\sigma^2} \quad (2-14)$$

The observed crack spacing for the cycled silicon and germanium electrodes cannot be explained by the conventional theories of thin film fracture. Many of the conventional theories predict crack spacing to be on the order of the film thickness. Those theories are generally consistent with experimental observations in engineering coatings. The crack morphology in cycled electrodes also resembles that of drying mud. However cracks in drying mud also exhibit crack spacing comparable to their depth [65].

In 2011, Xiao et al. proposed a model to describe the crack spacing in cycled electrodes, specifically for silicon [66]. The methodology follows that crack formation forms via local plastic strains between two neighboring cracks and the intent is to determine the minimum spacing to avoid crack formation. From the model, the force corresponding to the constrained expansion is balanced by the bonding at the interface, shown in Figure 2-11. The critical crack separation length can be defined by,

$$a_c = \frac{2h\sigma_Y}{\tau_i} \quad (2-15)$$

where h is the film thickness, σ_Y is the yield stress of the film, and τ_i the interfacial shear stress between the film and substrate. Therefore reducing the thickness of a film or improving the interfacial shear stress will lead to small crack spacing. The interfacial shear stress is bounded by the lower of either the shear strength between the film and substrate and the bulk shear flow stress of either the film or substrate.

2.5.2 Fracture Measurement

Extension of Equation 2-14 into three dimension results in circular islands where the critical crack spacing is equal in any direction through the center of mass. In real systems, the thin film islands resulting from film fracture have a variety of shapes and may not be symmetric. A convenient approach is to quantitatively compare the area, A_i , of each fractured island. An estimate of the crack spacing can then be determined through a circular approximation:

$$a_c = \sqrt{\frac{4A_i}{\pi}} \quad (2-16)$$

ImageJ, an image processing software, was used to make area measurements. Images with high contrast between the fractured islands and substrate, such as backscattered images due to Z-contrast, can be made binary by setting a grayscale threshold limit. The area and perimeter can easily be measured after calibrating the appropriate physical dimension per pixel. The Analyze Particles functions allows the user to exclude edges, ignore stray points by inputting a minimum area, and label each island shown in Figure 2-12. For low contrast images, each island was individually mapped using a polygon tool and overlay. After enclosing each island in a polygon, the area and perimeter can be measured using to the same method above.

2.5.3 Shape Descriptors

One useful shape descriptor for characterization of fractured surfaces is the fractal dimension. The fractal dimension provides a relationship to how a structure changes with relation to the scale of measurement. Two important characteristics of an island, its area and perimeter, can be related to a fractal dimension as follows,

$$p = kA^D \quad (2-17)$$

where **p** is the perimeter, **k** is a proportionality constant, and **D** is the fractal dimension.

Another useful shape descriptor is the circularity of a feature since a circular approximation is used in Equation 2-16. The circularity of an object is defined by the ratio of the perimeter and area to that of a circle, expressed in the following equation.

$$c = \frac{4\pi A}{p^2} \quad (2-18)$$

A circle would have a circularity of 1 and a square would have a circularity of 0.785 or $\pi/4$.

2.5.4 Statistical Analysis

All measurements made were not able to be reproduced to an exact level. In order to describe the random processes, measurements are reported with a confidence interval unless otherwise noted. The confidence intervals are reported so that type-I error or α -level is 0.05. The confidence interval for a measurement is expressed as follows,

$$CI = \frac{t_{n-1}S}{\sqrt{n-1}} \quad (2-19)$$

where **n** is the number of measurements, **S** is the sample standard deviation of the measurements, and t_{n-1} is the t-value for the sample population at **n** - 1 degrees of freedom.

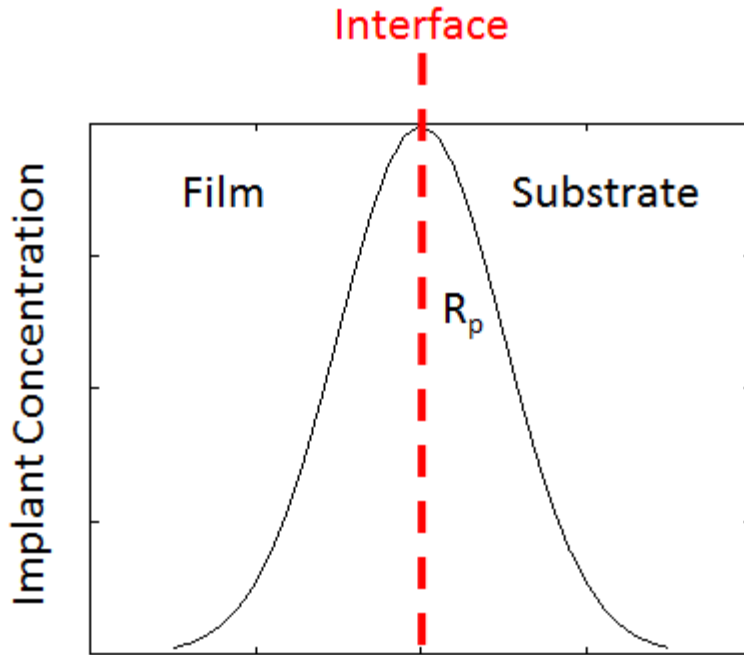


Figure 2-1. Implant profile for an idealized system to promote ion beam-mixing at the current collector interface.

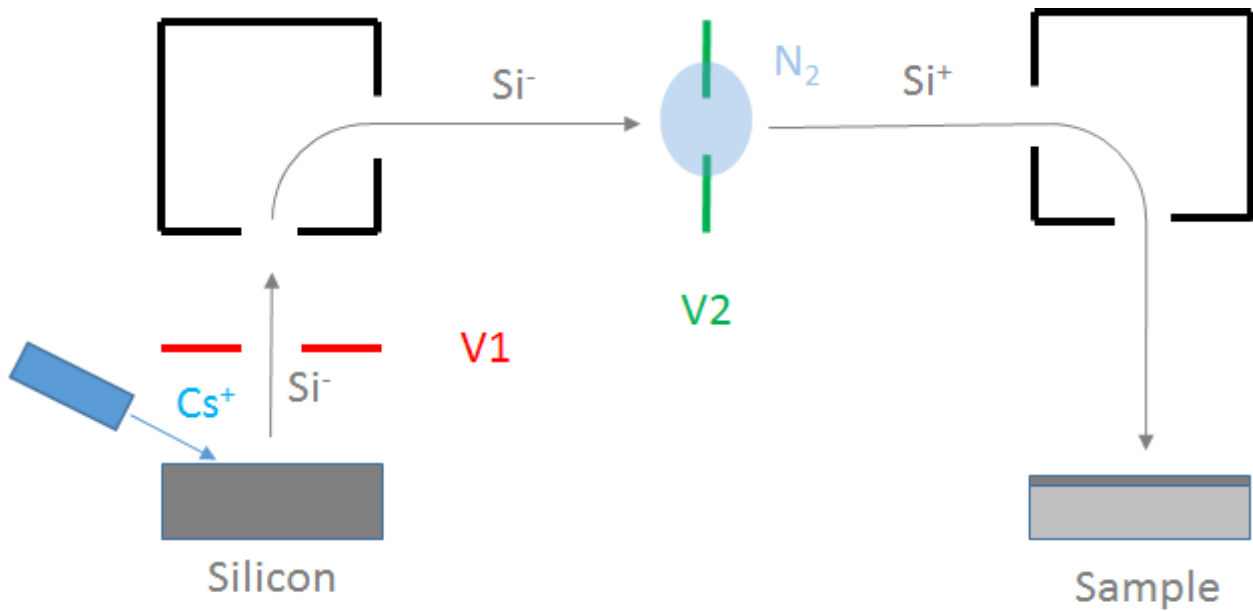
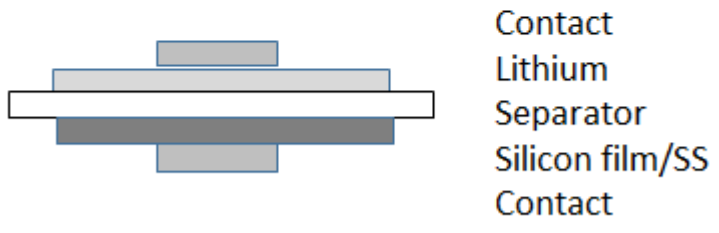
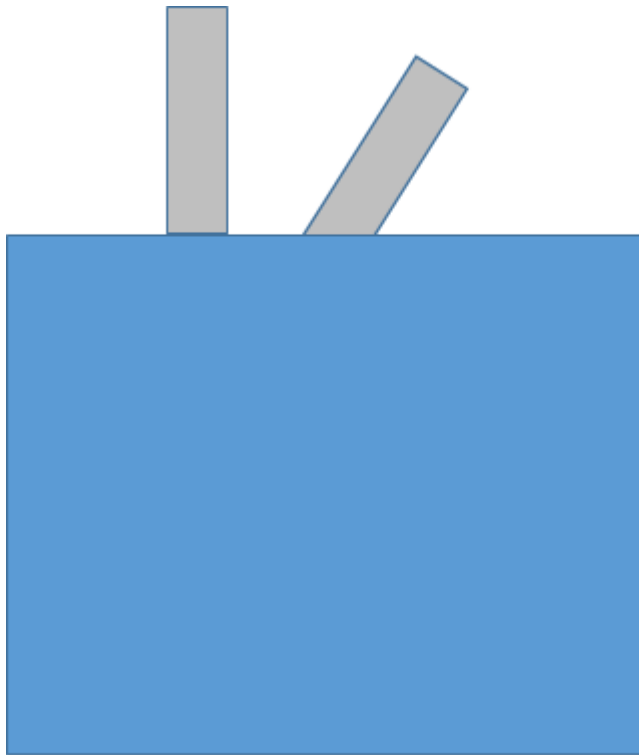
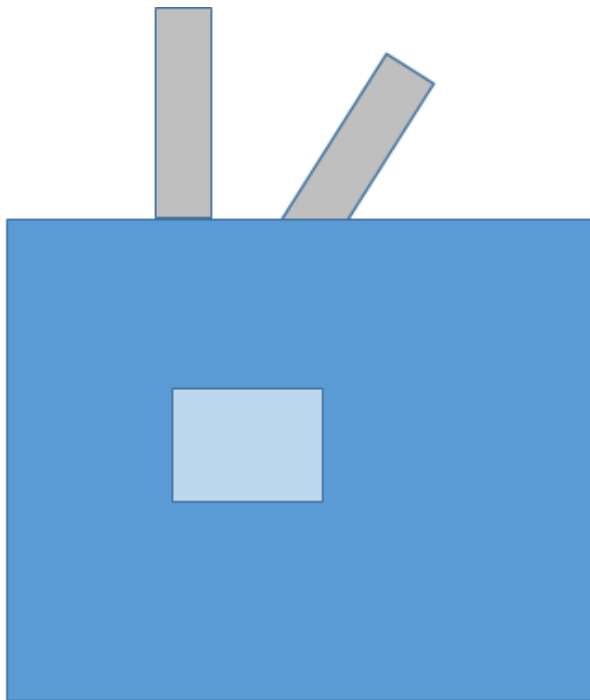


Figure 2-2. Schematic of the NEC model 5SDH-4 with a SNICS sputter ion source.



Contact
Lithium
Separator
Silicon film/SS
Contact

Figure 2-3. Exterior and cross-sectional view of a pouch cell.



Contact
Lithium
Separator
Silicon film/SS
Contact



Figure 2-4. Exterior and comparison cross-sectional views of the standard and windowed pouch cell.

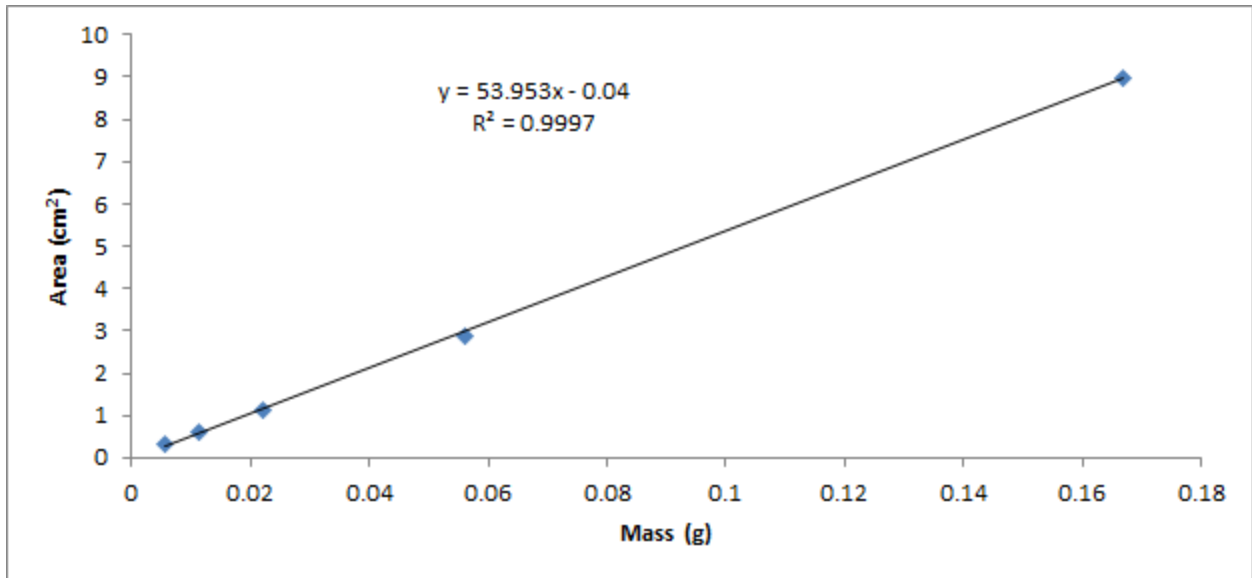


Figure 2-5. Plots to determine the areal mass density of the substrates: (a) nickel-iron and (b) 304 stainless steel.

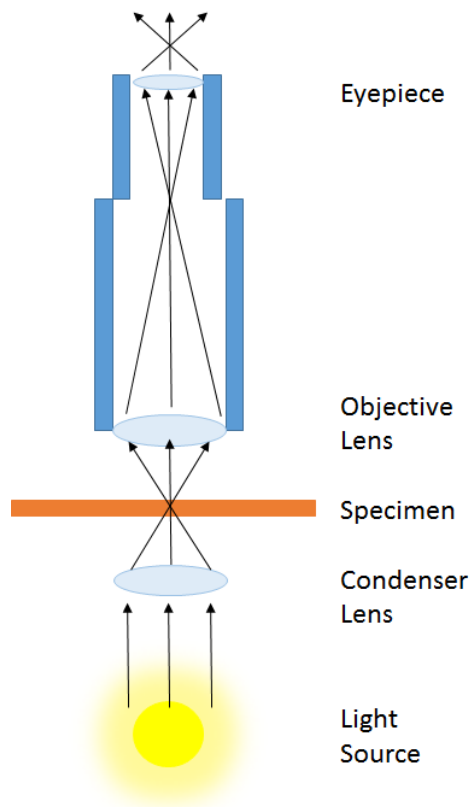


Figure 2-6. Schematic and optics of a light microscope under bright field conditions.

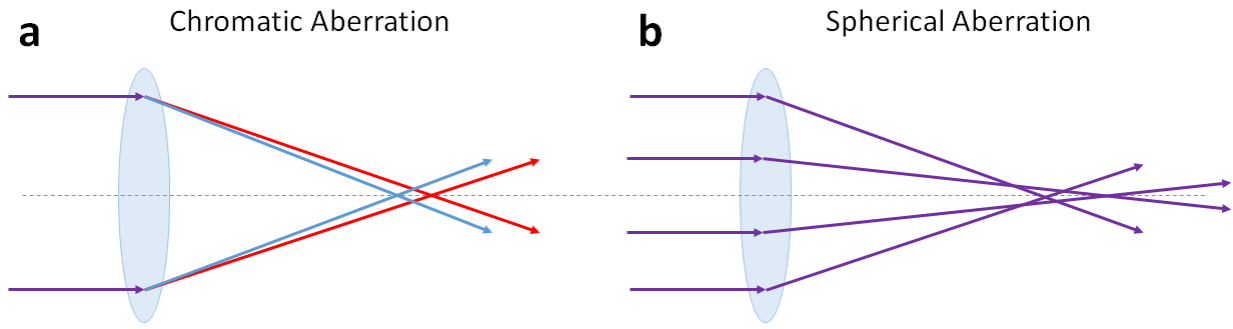


Figure 2-7. Optical ray diagram depicting different types of aberration: (a) chromatic and (b) spherical.

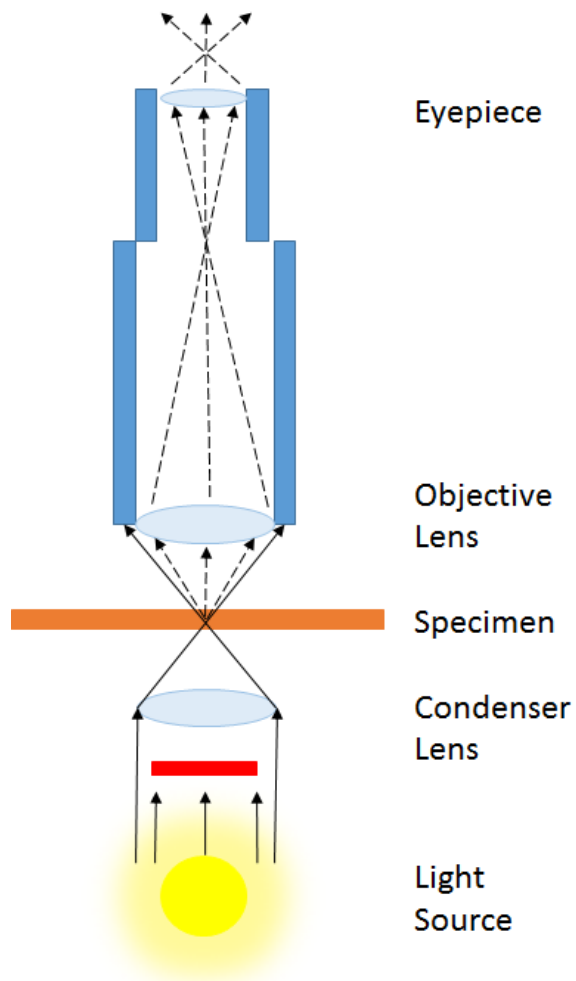


Figure 2-8. Schematic and optics of a light microscope under dark field conditions.

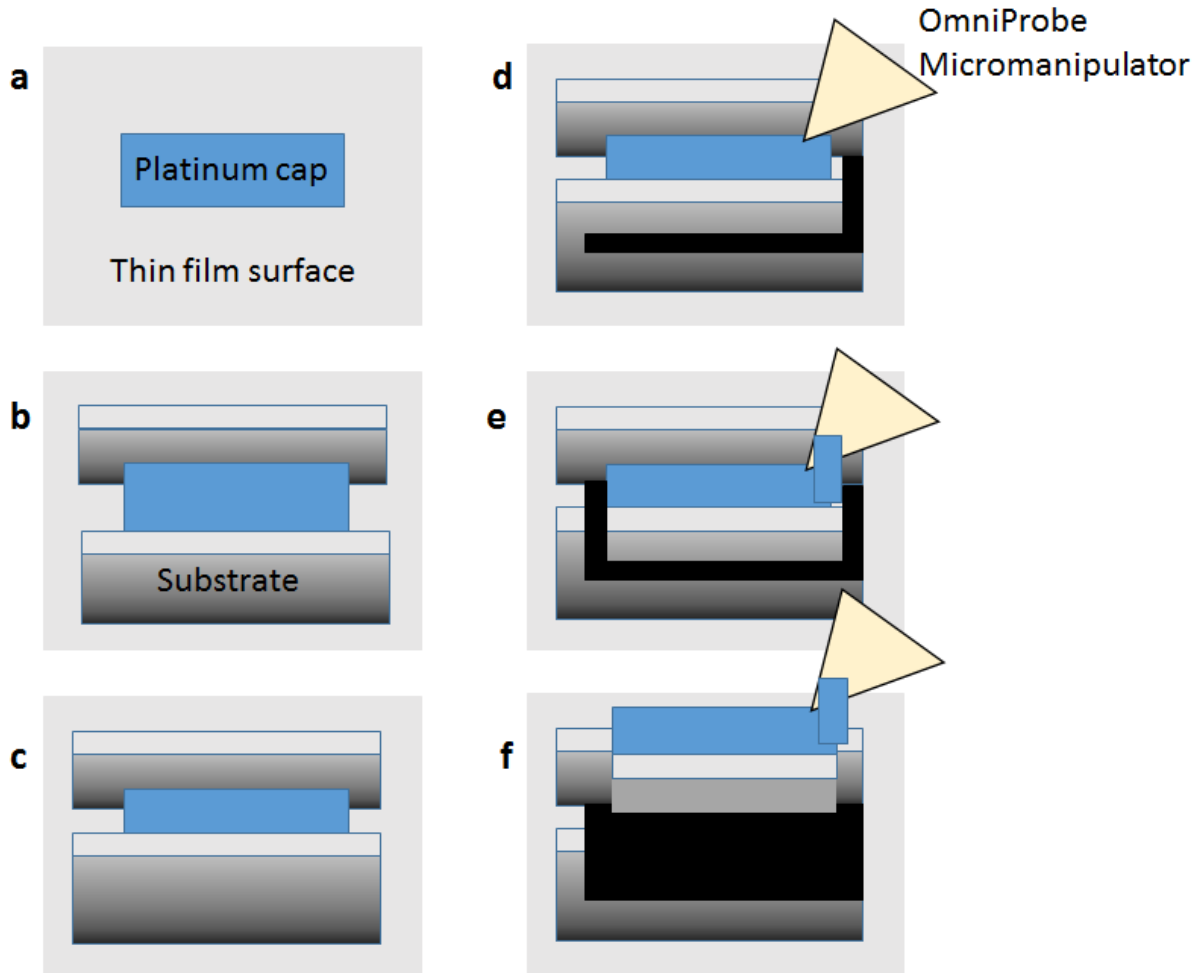


Figure 2-9. Methodology for XTEM sample preparation via FIB viewed at an angle. (a) Initially a protective platinum layer (blue) is deposited on to the specimen surface. (b) Trenches are cut on both sides of the platinum layer. (c) The sample is thinned further by incremental milling. (d) One sidewall cut and an undercut is made while the probe needle is inserted. (e) The XTEM specimen is attached to the micromanipulator by a platinum layer and the remaining sidewall is milled away. (f) The XTEM specimen is lifted from the sample and moved to a copper TEM grid.

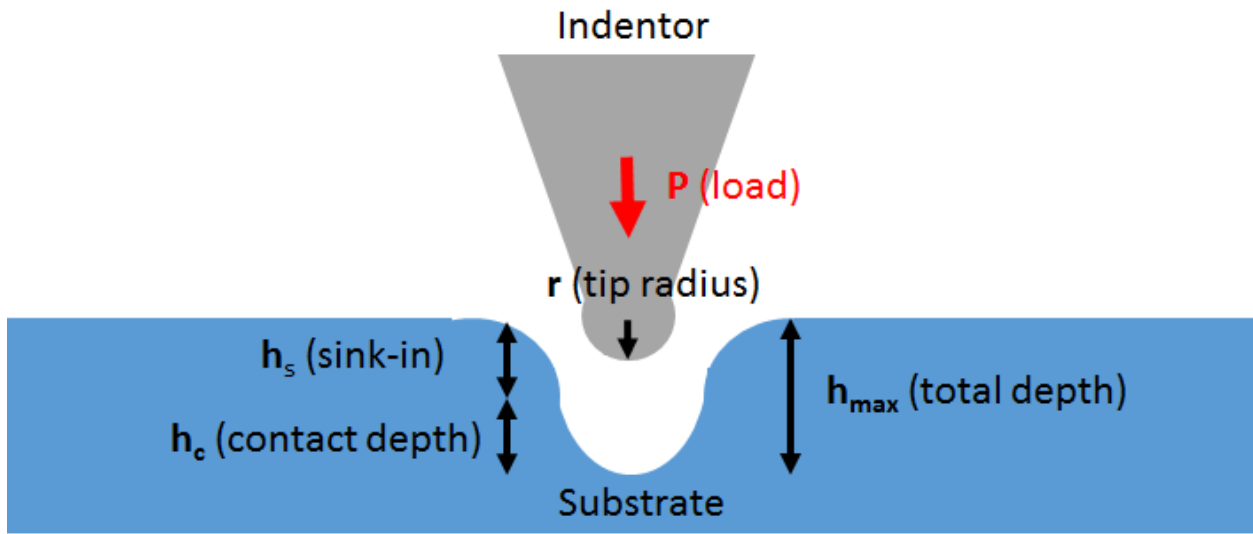


Figure 2-10. Cross-sectional illustration of nanoindentation induced surface deformations.

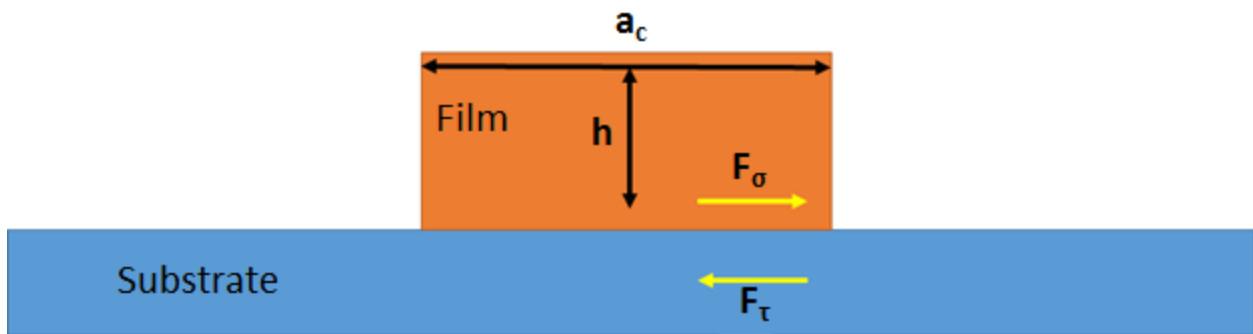


Figure 2-11. Cross-sectional illustration of the electrode cracking model.

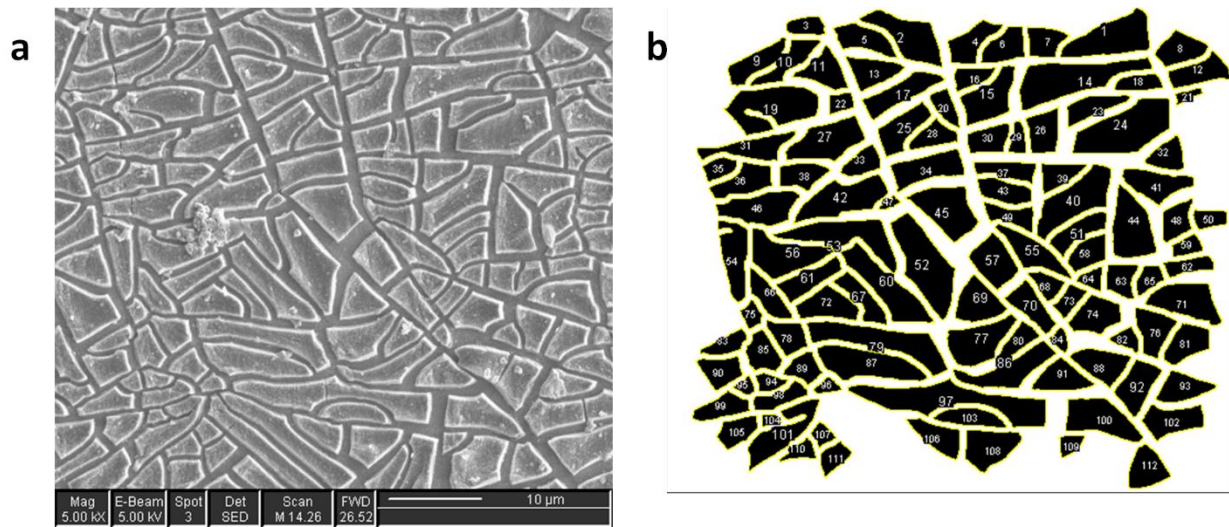


Figure 2-12. Labeling and island identification for a cracked electrode surface: (a) original SEM image and (b) numbered island masks through ImageJ.

CHAPTER 3

DEPOSITION AND IMPLANTATION OF GERMANIUM AND SILICON THIN FILMS

Thin film coatings are important to many industries and devices ranging from communications, sensors, optics, satellites, automobiles, and airplanes [67]. Thin film coatings can be deposited by a variety of techniques through deposition of a solid, liquid, or vapor phase. Two common vapor phase techniques are electron beam physical vapor deposition and plasma enhanced chemical vapor deposition. This chapter will investigate vapor phase deposition techniques to deposit thin film amorphous films of germanium and silicon.

3.1 Thin Film Deposition Techniques

3.1.1 Electron Beam Physical Vapor Deposition

Electron beam physical vapor deposition (EBPVD) is a type of physical vapor deposition where the source is heated by an electron beam under high vacuum. The source evaporated or sublimates in accordance with its vapor pressure and coats everything in the chamber within line of sight. A schematic of the EBPVD process is shown in Figure 3-1. The deposition rate of EBPVD is proportional to the pressure of the vapor phase.

In this experiment an electron beam heated a germanium source to induce a vapor species for deposition onto a 50 μm thick $\text{Ni}_{80}\text{Fe}_{20}$ substrate. The $\text{Ni}_{80}\text{Fe}_{20}$ substrate was cleaned with water, ethanol, acetone, and isopropyl alcohol before deposition to remove surface contamination. The chamber was evacuated to 10^{-7} torr. The electron beam slowly heated the target up to 15% power during a ramp up over 5 minutes. The power was held for 2 minutes. Afterwards, a 40% ramp up over 2 minutes occurred, with a hold for 1 minute. A shutter was then open to allow deposition on the substrate, where the deposition rate was $6 \text{ nm}\cdot\text{min}^{-1}$. After a film thickness of 140 nm was achieved, the electron source went to 0% power over a 5 minute ramp down.

3.1.1 Plasma Enhanced Chemical Vapor Deposition

Plasma enhanced Plasma enhanced chemical vapor deposition (PECVD) is a commonly used technique for the deposition of hydrogenated amorphous silicon (a-Si:H) for applications such as image sensors, solar cells, electrophotography, and active matrix displays. PECVD utilizes a plasma to access dissociation, ionization, and excitation reactions that would otherwise require high temperatures, such as with chemical vapor deposition (CVD). The benefit of lower temperature is a large selection of substrates. Relatively high deposition rates and good sidewall coverage are benefits that PECVD has over physical vapor deposition (PVD), another low temperature deposition process.

A schematic of a PECVD system is shown in Figure 3-2. To create the plasma, a potential bias is applied across to the two electrodes which ionizes a gas through inelastic collisions called the "Townsend avalanche". Because of the light mass and high velocity of electrons, charge separation causes the plasma potential to be higher than either electrode while the energy transfers during collisions range between zero to tens of electron volts. The positive ions in the plasma are accelerated to either electrode across the plasma sheath, a thin space charge region where almost all of the potential drop occurs.

Film deposition relies on a variety of parameters including pressure, electrode spacing, substrate temperature, power density, gas flow rate, and frequency. Increasing the power density or plasma pressure can increase deposition rate, increase total dissociation and ionization, and increase secondary reactions. At higher pressures and power densities, powder formation may be favored over film growth since the reactants are unable to diffuse to the surface and reactions with higher order byproducts.

In this experiment, amorphous silicon was deposited on a 25 μm thick 304 stainless steel substrate (Trinity Brand Inc.). The stainless steel substrate was cleaned with water, ethanol, acetone, and isopropyl alcohol before deposition to remove surface contamination.

The PECVD film was deposited with an rf-frequency of 13.56 MHz at a power of 30 W. The substrate temperature was kept constant at 573 K. Silane was supplied for deposition at 46 ± 1 standard cubic centimeters per minute (sccm) with Ar (450 ± 5 sccm) and N₂ (2250 ± 10 sccm) carrier gases where the variability is indicative of the observed fluctuation range. The chamber pressure during deposition was constant at 750 mTorr. A 350 nm amorphous silicon film was deposited after 37 minutes, resulting in a film growth of 0.158 nms^{-1} ($\sim 10 \text{ nm-min}^{-1}$).

3.2 Thin Film Characterization

3.2.1 Amorphous Germanium

Using methods outlined in Chapter 2.4.3, an XTEM sample was made from the germanium film shown in Figure 3-3. The film thickness is measured to be 140 nm. The film is deposited with no detectable morphology defects or internal porosity. Figure 3-4 shows STEM images of the interface between the germanium and Ni₈₀Fe₂₀ substrate under both dark and bright field conditions. The dark field image shows a region with low contrast between the germanium film and substrate, suggesting that either the region is preferentially thinned during processing or elements with a lighter mass are located within the region. The bright field image shows the transition between the crystalline substrate and amorphous film at the same location as the dark field image. A portion of the bright field image can be seen at a higher magnification in Figure 3-5.

EDS was used to investigate the low contrast region as shown in Figure 3-6. A line scan was initiated in the germanium film, across the low contrast region, and into the Ni₈₀Fe₂₀ substrate. The EDS spectrum at locations along the line show the emergence of an oxygen K α peak, which has a characteristic x-ray energy of 0.525 keV. A line plot with values corresponding to the number of counts for Ge K α (9.874 keV), Ni K α (7.471 keV), and O K α alternatively reveals the increased concentration of oxygen at the interface between the germanium and Ni₈₀Fe₂₀ substrate.

The germanium film was also characterized by poor adhesion to the $\text{Ni}_{80}\text{Fe}_{20}$ substrate. A piece of tape was able to remove the portion of the film that was in contact. The film otherwise conformed to the surface morphology of the $\text{Ni}_{80}\text{Fe}_{20}$. The only other unusual occurrence with the film was the formation of blisters when heated on a hot plate. The heating was not a normal part of preparation for battery cycling, but used as a method to mount samples for nanoindentation via Crystal-Bond.

3.2.2 Amorphous Silicon

An XTEM sample was made from the silicon film shown in Figure 3-7. The film thickness is found to be 350 nm. As with the germanium film, the silicon film has no detectable morphology defects or internal porosity. A top-down OM image shows the surface morphology of the steel and silicon coated steel in Figure 3-8. The surface is rough, but the film conforms to all the surface features. Upon cooling, the silicon film develops a compressive residual stress from the differences in coefficients of thermal expansion (CTE) between the stainless steel substrate and the amorphous silicon. The CTE for 304 SS is on the order of $10 - 20 \times 10^{-6} \text{ K}^{-1}$ [68]. The CTE of amorphous silicon can vary between $3.0 - 4.5 \times 10^{-6} \text{ K}^{-1}$ with a biaxial modulus of $130 - 150 \text{ GPa}$ [69]. Over a temperature drop of 280 K, it is expected that the film experiences a compressive stress on the order of a few GPa. Buckling in amorphous silicon thin films is expected to occur at a compressive stress at 1.2 GPa, a value that was certainly exceeded from the differences in thermal expansion [70].

The compressive stress is enough to cause the film to buckle and fracture, shown in Figure 3-9. The buckling shows a fractal pattern. The film buckling did not occur across the entire sample surface, but at discrete regions scattered across the surface, as seen in Figure 3-10. The discoloration around the edges of the deposited region is due to thickness variations since the region was partially masked. Except for the region of buckled film, the silicon film was

not able to be delaminated with a piece of tape. Pristine regions without any film buckling were selected for electrode preparation or ion implantation.

3.3 Concluding Remarks

EBPVD and PECVD were used to deposit amorphous thin films of germanium and silicon, respectively. Both films conformed to the morphology of the substrate surface, and neither showed any internal porosity. Germanium films were deposited with a thickness of 140 nm and silicon films with a thickness of 350 nm. The germanium films were marked by poor adhesion to the $\text{Ni}_{80}\text{Fe}_{20}$ substrate, while the silicon films were plagued by buckling from residual thermal stresses.

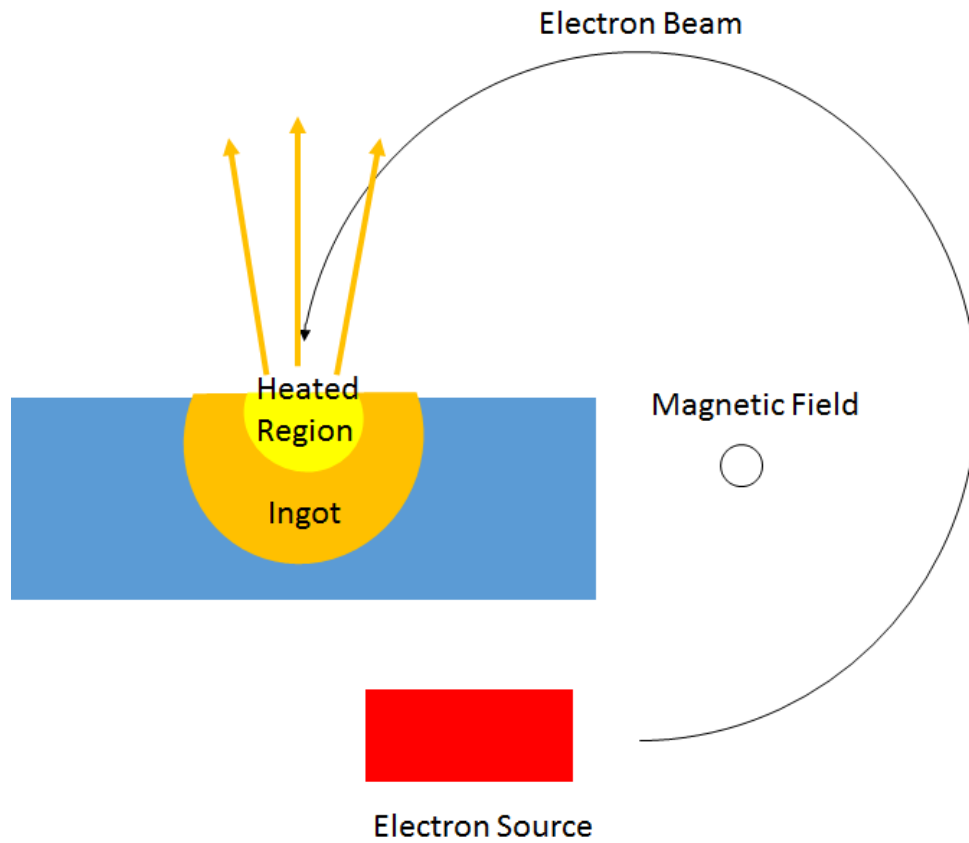


Figure 3-1. Schematic of an EBPVD system.

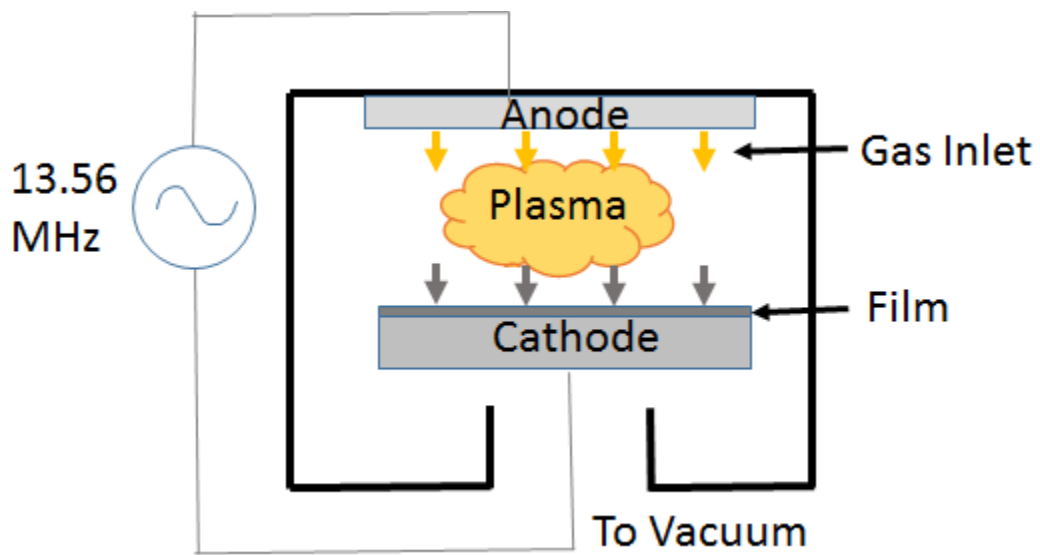


Figure 3-2. Schematic of a PECVD system.

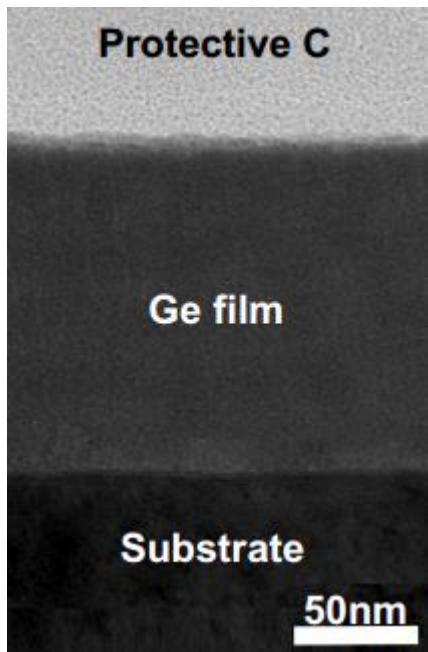


Figure 3-3. XTEM image of a 140 nm germanium film on a nickel-iron substrate.

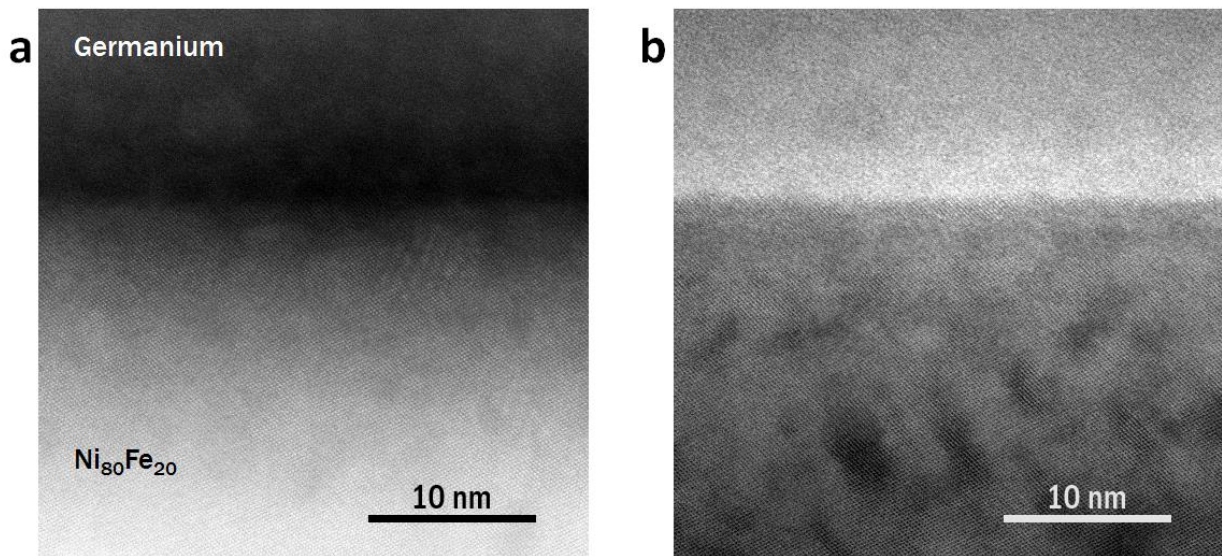


Figure 3-4. STEM images of the interface between the as-deposited germanium film and $\text{Ni}_{80}\text{Fe}_{20}$ substrate under (a) HAADF and (b) bright field conditions.

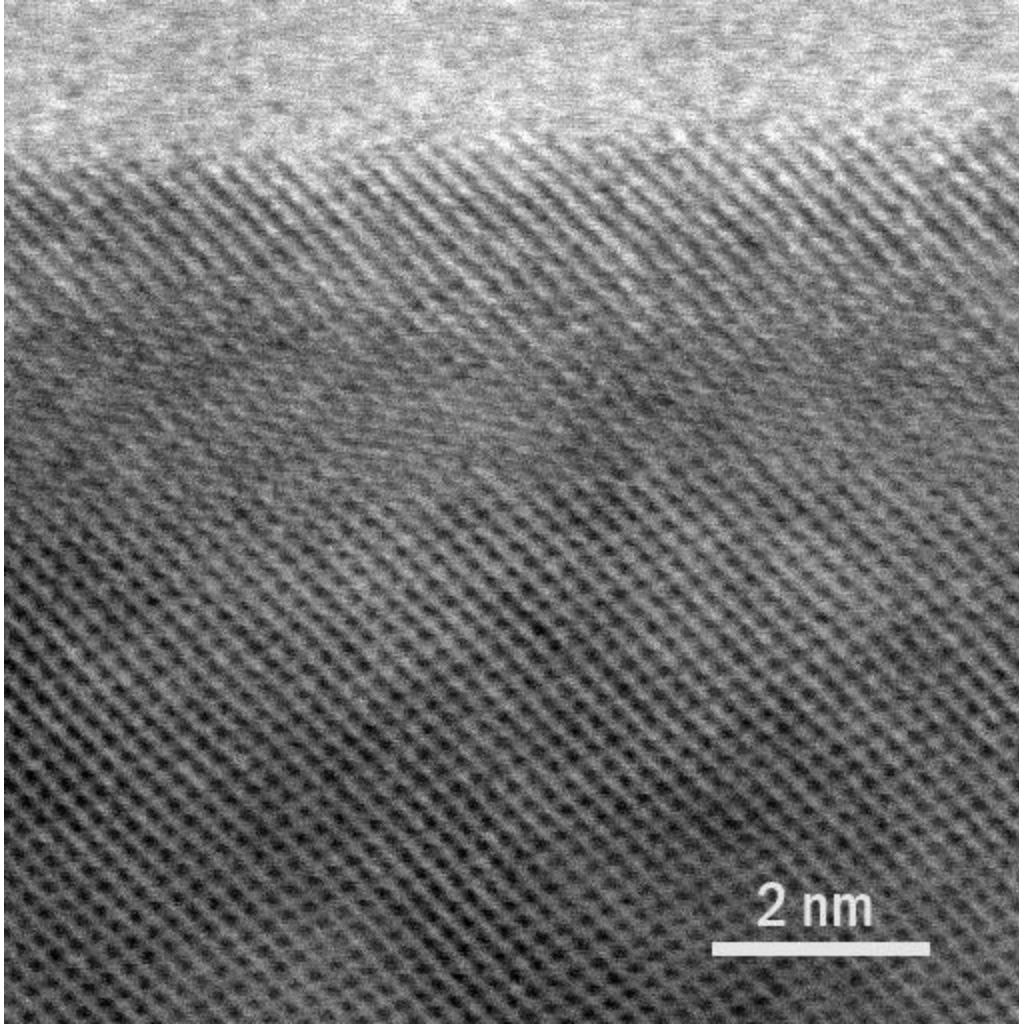


Figure 3-5. High resolution STEM bright field image of the interface between the as-deposited germanium film and $\text{Ni}_{80}\text{Fe}_{20}$ substrate.

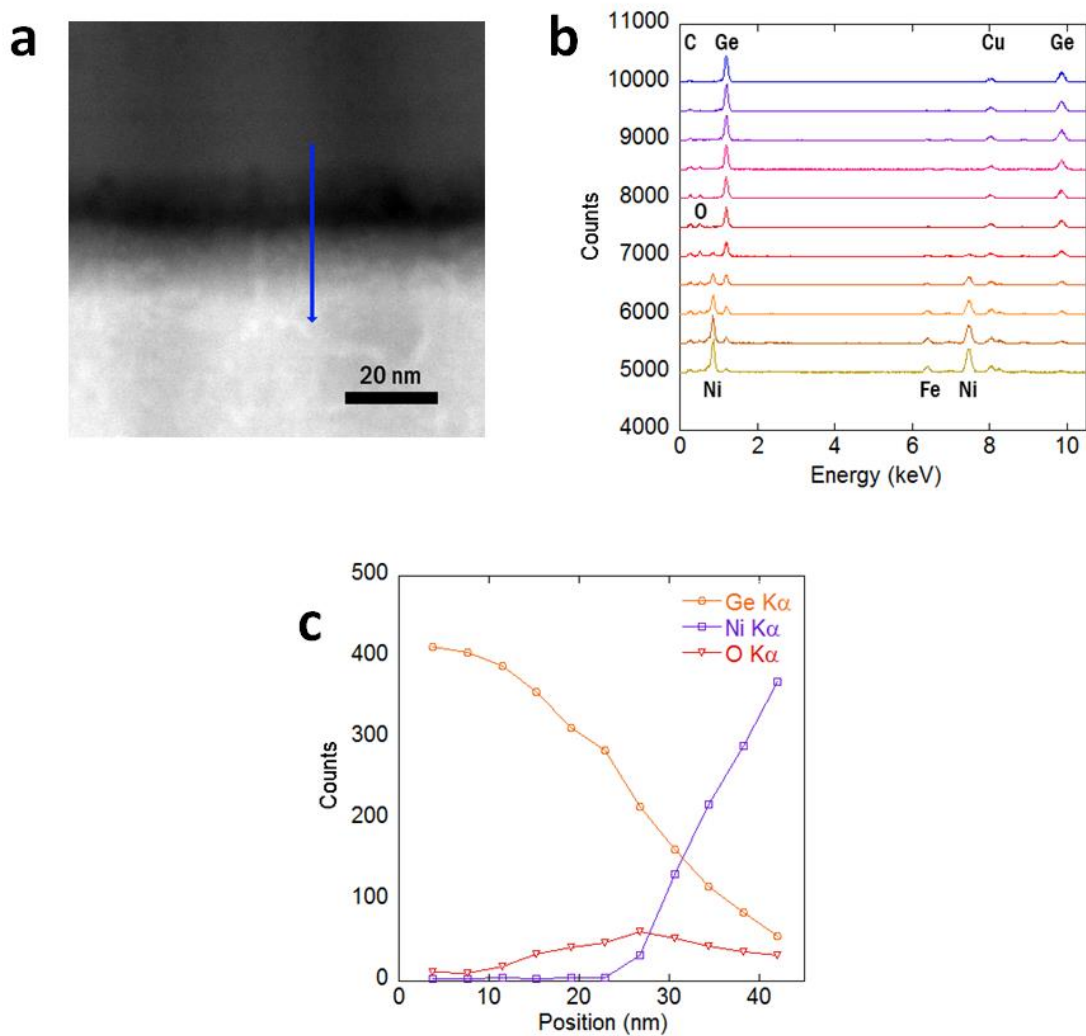


Figure 3-6. STEM-HAADF image and EDS profile of the interface between the as-deposited germanium film and $\text{Ni}_{80}\text{Fe}_{20}$ substrate. The scan line (a) is shown crossing three regions with the EDS profile shown for each point along the line in (b). Part (c) depicts the concentration profile of germanium, nickel, and oxygen along the scan length.

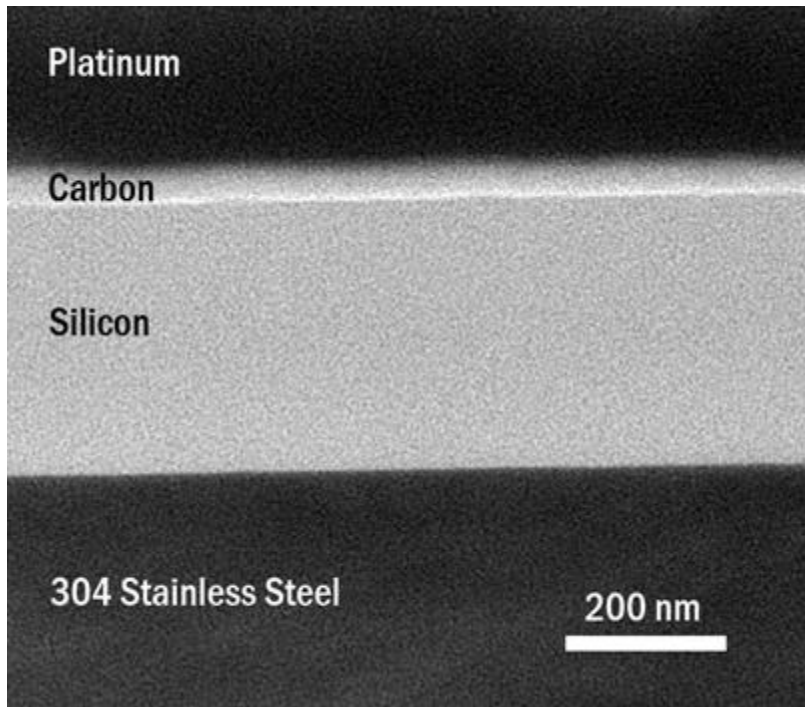


Figure 3-7. XTEM image of a 350 nm amorphous silicon film on a 304 stainless steel substrate.

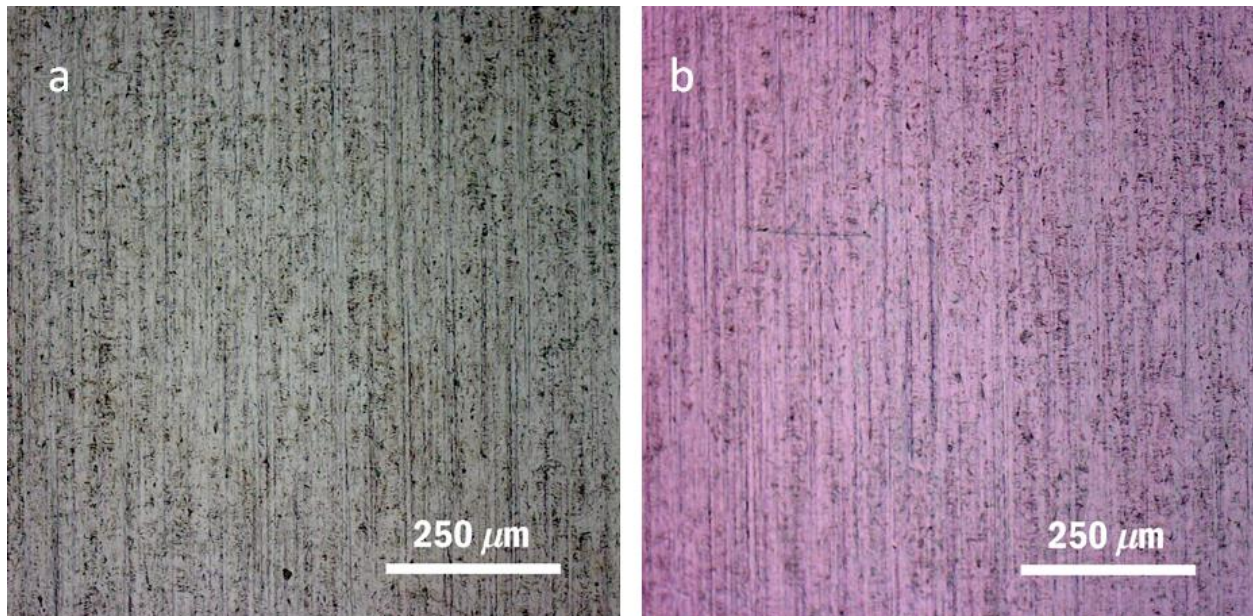


Figure 3-8. OM image of surface roughness for the (a) stainless steel and (b) silicon coated steel surface. The thin film conforms to the surface features.

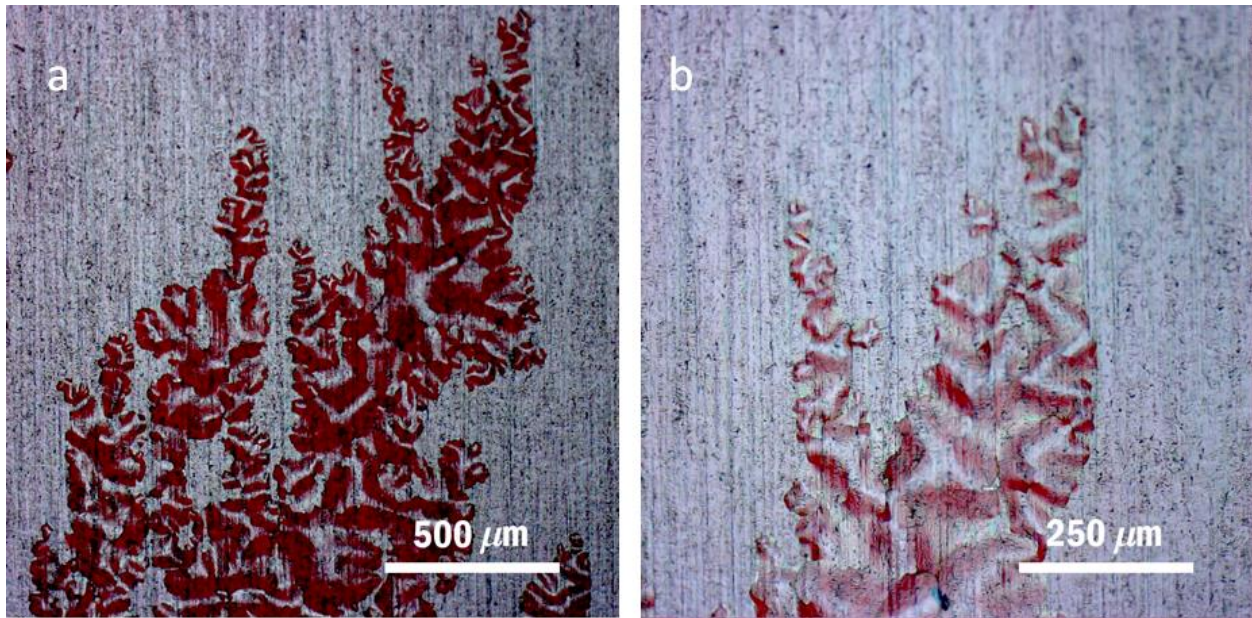


Figure 3-9. OM image of thin film silicon buckling event at (a) low magnification and (b) high magnification.

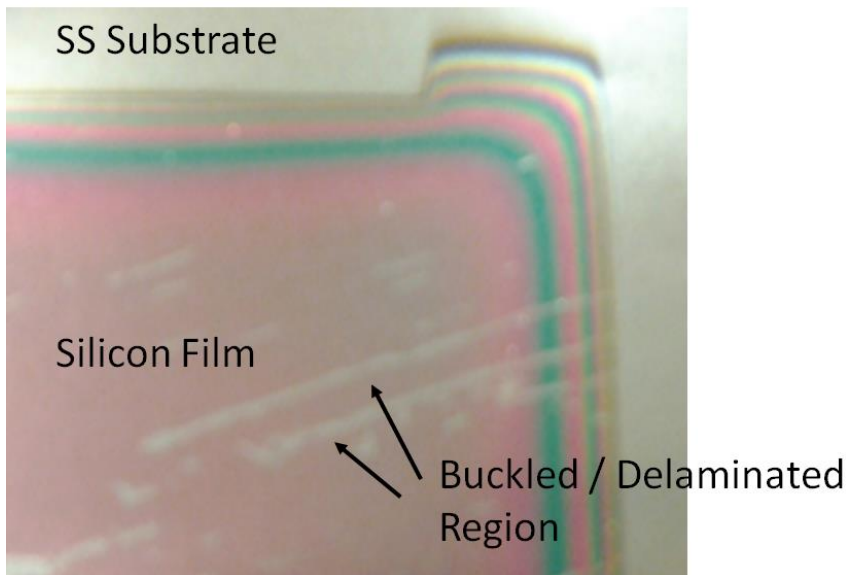


Figure 3-10. Digital photograph of the PECVD silicon film deposited on stainless steel. The buckling is not continuous across the entire surface, leaving a large area of pristine film. The discoloration around the edges is due to thickness variations since the region was partially masked.

CHAPTER 4

ION BEAM-MIXED GERMANIUM ELECTRODES

Germanium electrodes for a lithium ion battery were first investigated in the early 1980s for the molten salt battery [71]. While the lithium-aluminum electrodes suffered from morphological changes and volumetric expansion [72], the primary problem with lithium-silicon electrodes was the corrosive behavior towards common electrode contacts, such as stainless steel [73]. Germanium was sought out due to its position on the periodic table, being similar to lithium, but perhaps avoiding the corrosive behavior. High temperature charge-discharge and coulometric titration experiments revealed several reaction plateaus, corresponding to LiGe , Li_9Ge_4 , $\text{Li}_{16}\text{Ge}_5$, $\text{Li}_{15}\text{Ge}_4$, and $\text{Li}_{22}\text{Ge}_5$ [71]. Furthermore, the high cost of germanium and interest in room temperature batteries limited further investigation of germanium as an electrode.

It was not until 2004 that nanostructured germanium was shown to be a viable electrode for room temperature lithium ion batteries [23]. The germanium films were deposited at thicknesses between 60 and 250 nm and cycled fifty times at a C/4 rate (375 mA g^{-1}) between 0 and 1.5 V vs Li^+/Li . The ballistically deposited film lost 60% of its initial capacity by cycle fifty; however, the evaporated germanium film lost only about 30% of its initial capacity after the first cycle and remained stable over fifty cycles [23]. The nanostructured germanium was necessary due to the poor diffusivity of the electrode ($2.14 \times 10^{-7} \text{ cm}^2\text{s}^{-1}$ at 633 K, $6.4 \times 10^{-12} \text{ cm}^2\text{s}^{-1}$ extrapolated to 300 K), which was offset by the high temperatures in the molten salt cell [74]. The diffusivity of germanium was experimentally verified as between $5 \times 10^{-12} \text{ cm}^2\text{s}^{-1}$ and $1.75 \times 10^{-10} \text{ cm}^2\text{s}^{-1}$ depending on the fraction of lithium in to the germanium and doping [75]. While investigating germanium nanowires, the bond between the nanowire and substrate was emphasized, as opposed to nanowires scattered in random orientations within a conductive binder [28]. The emphasis on adhesion was taken one step further in the first study on ion beam-mixing on a thin film germanium electrode in 2013, where a dose $10^{16} \text{ Ge}^+ \text{ cm}^{-2}$ was

shown tremendously increase cycling performance over the as-deposited electrode [43]. In this chapter, the role of the implanted self-ion dose will be investigated in relation to cycling performance. The improvement in adhesion will also be investigated through nanoindentation and fracture analysis.

4.1 Experiments

4.1.1 Sample Preparation

A 140 nm thin film of amorphous germanium was deposited on a $\text{Ni}_{80}\text{Fe}_{20}$ substrate using EBPVD. The thin film was implanted with ion doses of $10^{13} - 10^{16} \text{ Ge}^+ \text{ cm}^{-2}$. Germanium was chosen as the implant species to prevent doping which could improve electrical conduction of the germanium. The only effect of the implanted ion should be towards ion beam-mixing. The implant voltage was 260 kV with a beam current of 500 nAcm^{-2} . At a 260 kV accelerating voltage, the peak of the Ge^+ implant profile would be approximately at the interface between the germanium film and substrate. The implant temperature was 77 K to avoid unwanted nanostructures which form at higher temperatures from ion implantation [76-79]. While the nanostructures should increase the rate capability of the electrode due to the increased surface area and provide better stress mitigation, the impact of morphology changes and improved adhesion would be conflated. The electrodes were prepared in the pouch cell configuration as described in Chapter 2.2.

4.1.2 Nanoindentation

Since the as-deposited germanium film was able to be removed with a piece a tape, nanoindentation was used in order to attempt to quantify the adhesion strength between germanium and the $\text{Ni}_{80}\text{Fe}_{20}$ substrate. The as-deposited and ion beam-mixed germanium films were indented at loads of 20, 200, 450, and 800 μN . All indents has a 5 second load time, 2 second hold time, and a 2 second unloading time. The 20 μN load was used to gain insight on the mechanical properties of the film without influence of the substrate. The 800 μN load

corresponds to a through-thickness indent in order to induce fracture. The footprint of the indents were no larger than 500 nm across at 800 μN and were spaced 5 μm apart in order to avoid any influence from nearby indents. A tighter 8 x 15 array of indents with 1 μm spacing was tested to observe the influence of nearby indents and induce fracture.

4.1.3 Electrochemistry

The as-deposited and implanted films were galvanostatically tested for 50 cycles between the voltage range of 0.01 – 1.5 V. The applied current was equal to 810 mA g^{-1} , which corresponds to a cycling rate of 0.5C for the $\text{Li}_{22}\text{Ge}_5$ endpoint or approximately a 0.6C rate for the $\text{Li}_{15}\text{Ge}_4$ endpoint. The samples were also tested with cyclic voltammetry with a sweep rate of 278 μVs^{-1} across the same 0.01 – 2.0 V range. The microstructure of cycled electrodes were observed under SEM to determine the average fractured island size.

4.2 Results

4.2.1 Thin Film Characterization

An XTEM image of the implanted and as-deposited germanium thin film is compared in Figure 4-1. The implanted sample shows no detectable differences with the as-deposited sample, confirming that implantation at 77 K avoided the creation of a porous, nanostructured surface. An estimate of the ion implantation profile simulated from the TRIM code is also overlaid for comparison. The highest concentration of the implanted Ge^+ ions are located at the interface between the germanium film and $\text{Ni}_{80}\text{Fe}_{20}$ substrate.

The STEM bright field images of Figure 4-2 are useful to compare the impact of the ion beam-mixing at the interface. The as-deposited sample substrate shows a defect density that is roughly independent of depth into the substrate. In the $10^{15} \text{ Ge}^+ \text{ cm}^{-2}$ ion beam-mixed sample, a damaged region can be seen at the surface of the substrate. This damaged region extends approximately 70 - 80 nm in depth, which corresponds to a concentration of about $6.0 - 20.0 \times 10^{17} \text{ Ge}^+ \text{ cm}^{-3}$ according to the TRIM simulation. It also noted that the surface of the germanium

electrode appears lighter in the top 20 nm of the film compared to the rest of the germanium film.

Unlike the as-deposited thin films, the ion beam-mixed germanium films could not be peeled off by a piece of tape. This was true even for the low implant dose of $10^{13} \text{ Ge}^+ \text{ cm}^{-2}$, which is less than the implant of one atomic layer worth of atoms.

4.2.2 Nanoindentation

A series of representative load-depth plots are shown in Figure 4-3, comparing the as-deposited film to the $10^{15} \text{ Ge}^+ \text{ cm}^{-2}$ ion-mixed germanium film. The loading characteristics show no significant differences except at the through-thickness depth where there is a discontinuity or “pop-in” in the as-deposited sample. The mechanical properties of the germanium film can be seen in Figure 4-4 as a function of indent depth. The properties at shallow depths are poorly defined; however, the measurements of the as-deposited and implanted germanium film generally overlap each other, suggesting minimal differences in mechanical properties. At large indent depths properties are convoluted due to the pop-in event for the as-deposited film. Shallow indentation of the as-deposited germanium film yielded a Young’s modulus of $80.5 \pm 4.5 \text{ GPa}$ and a hardness of $6.64 \pm 0.67 \text{ GPa}$. Shallow indentation of the $10^{15} \text{ Ge}^+ \text{ cm}^{-2}$ implanted film yielded a Young’s modulus of $95.4 \pm 17.1 \text{ GPa}$ and a hardness of $7.41 \pm 1.02 \text{ GPa}$. Indentation of the $\text{Ni}_{80}\text{Fe}_{20}$ substrate yielded a Young’s modulus of $142 \pm 6 \text{ GPa}$ and a hardness of $3.23 \pm 0.25 \text{ GPa}$.

Representative impressions from nanoindentations at $800 \mu\text{N}$ are shown in Figure 4-5, when indents are spaced $5 \mu\text{m}$ apart. The as-deposited germanium film shows a radial crack that protrudes 650 nm from the indent impression. The $10^{13} \text{ Ge}^+ \text{ cm}^{-2}$ implanted germanium film shows a radial crack that protrudes 425 nm from the indent impression. The $10^{15} \text{ Ge}^+ \text{ cm}^{-2}$ implanted germanium film does not show any evidence of a radial crack. In some situations, cracks would propagate out of two vertices instead of just one as shown; however, no cracks

were observed to propagate from all three vertices. Out of twenty observed indents, the as-deposited germanium film was accompanied by fracture all twenty times. Sample statistics for the indents into the as-deposited germanium film show an average crack length for the as-deposited film is 597 ± 76 nm. The 10^{13} Ge⁺ cm⁻² implanted germanium film fractured for twenty-four out of the fifty indents. Although only twenty-four fractures were observed, the loading curves showed significant pop-in events for thirty-five of the indents. Sample statistics for the indents into the 10^{13} Ge⁺ cm⁻² implanted germanium film show an average crack length for the as-deposited film is 421 ± 37 nm. The 10^{15} Ge⁺ cm⁻² implanted germanium film never fractured in fifty indents. An array of indents is shown in Figure 4-6 where a significant difference in film response can be seen. The as-deposited sample shows a completely cracked surface. The 10^{15} Ge⁺ cm⁻² implanted germanium film exhibits no failure mode from the array of indents, even when indents are positioned nearly on top of each other.

In Figure 4-7, the XTEM image shows an 800 μ N indent into an as-deposited germanium film where the indent spacing was 5 μ m. The through-thickness indent is verified, and substrate yielding is evident both from the deformation at the interface and the volume of dislocations within the substrate underneath the indent. Fracture along the interface nearby the indent appears to have initiated when comparing the contrast locally to the rest of the film. A similar indent is shown in Figure 4-8 for the 10^{15} Ge⁺ implanted film. The XTEM image shows plastic deformation of the substrate with no observable delamination of the ion beam-mixed germanium film.

4.2.3 Electrochemistry

The charge and discharge curves of the as-deposited germanium electrode and 10^{15} Ge⁺ cm⁻² ion-mixed electrode cycled at the 810 mA g⁻¹ rate are shown in Figure 4-9. The as-deposited germanium electrode shows a reduction in capacity during cycling. The ion beam-mixed electrode does not exhibit any systematic capacity fade after fifty cycles. The charge and

discharge curves are not entirely reproducible as cycling progresses. During the first charge cycle, the potential drops below 0.4 V vs Li/Li⁺ before returning to characteristics that are reproduced in every other charge cycle. The drop in potential is likely due to a diffusion limited impedance and was random from sample to sample. The discharge profile for cycle fifty is also unique due to the lower voltage at which lithium extraction begins, as opposed to the plateau potential of approximately 0.5 V vs Li/Li⁺.

The CV profiles of the first, fifth, and twentieth cycles of an as-deposited germanium electrode and a 10¹⁵ Ge⁺ cm⁻² ion beam-mixed germanium electrode can be compared in Figure 4-10. In the as-deposited sample, the first cycle shows a single oxidation peak at 0.62 V that decreases to 0.59 V after five cycles and 0.57 V vs Li/Li⁺ after 20 cycles. The reduction peaks in the first cycle are at voltages of 0.45 V, 0.36 V, and 0.10 V vs Li/Li⁺. By the fifth cycle, the distinct reduction peak at 0.45 V vs Li/Li⁺ is lost. The reduction in current from the first to twentieth cycles mirrors the loss in capacity in the life-cycle testing. In the ion beam-mixed sample, the first cycle shows a single oxidation peak at 0.63 V that decreases to 0.62 V after 5 cycles and 0.59 V vs Li/Li⁺ after twenty cycles. The reduction peaks in the first cycle are at voltages of 0.47 V, 0.34 V, and 0.10 V vs Li/Li⁺ which are retained after twenty cycles with minor voltage shifts. A comparison between the fifth cycles of both electrodes can be seen in Figure 4-11.

The cycle life behavior of the as-deposited and all ion beam-mixed germanium electrodes can be seen in Figure 4-12. The as-deposited germanium electrode fails rapidly, losing over 70% of its total capacity with ten cycles. The 10¹³ Ge⁺ implanted electrodes are not significantly better than the as-deposited electrode, also losing its capacity rapidly. These electrodes are only able to last two cycles at a gravimetric capacity above 1,400 mAhg⁻¹. The 10¹⁴ Ge⁺ implanted electrodes are able to last five to ten cycles above 1,400 mAhg⁻¹ before a rapid decline in capacity. The 10¹⁵ and 10¹⁶ Ge⁺ implanted electrodes exhibit a relatively

constant capacity for all fifty cycles. Across all samples, the charge efficiency of the first cycle is $85.9 \pm 4.6 \%$ with an average charge capacity of $1,707 \pm 156 \text{ mAhg}^{-1}$ and an average discharge capacity of $1,454 \pm 47 \text{ mAhg}^{-1}$. The charge efficiency across all fifty cycles can be seen in Figure 4-13. The as-deposited and 10^{13} Ge^+ implanted electrodes show drop in efficiency corresponds to the drop in capacity previously shown. The 10^{14} Ge^+ implanted electrode shows similar behavior, except that the loss of efficiency is not so drastic. Interestingly, the 10^{15} Ge^+ implanted electrode shows a constant decline in efficiency, but it does not correspond to a loss in capacity. The 10^{16} Ge^+ implanted electrode has an inefficient first cycle, but a relatively stable efficiency of about $96.2 \pm 0.37\%$ across the next forty-nine cycles.

4.2.4 Cycling Induced Fracture

After fifty cycles, the remaining amount of germanium film still adhered to the substrate correlated with the capacity measurements. The as-deposited, 10^{13} , and 10^{14} Ge^+ implanted electrodes had small regions of well adhered film with some scattered islands. The 10^{15} and 10^{16} Ge^+ implanted electrodes almost had complete surface coverage on the substrate. The fractured microstructure of cycled germanium electrodes can be seen in Figure 4-14. The as-deposited electrode did not have a well-defined crack spacing or island shape, so no measurements were made. Based off of measurements of 33 islands, the average island area for the $10^{13} \text{ Ge}^+ \text{ cm}^{-2}$ ion-mixed electrode is $70.9 \pm 16.6 \mu\text{m}^2$. Based off of measurements of 49 islands, the average island area for the $10^{14} \text{ Ge}^+ \text{ cm}^{-2}$ ion-mixed electrode is $24.6 \pm 5.4 \mu\text{m}^2$. Based off of measurements of 75 islands, the average island area for the $10^{15} \text{ Ge}^+ \text{ cm}^{-2}$ ion-mixed electrode is $17.6 \pm 1.7 \mu\text{m}^2$. Based off of measurements of 75 islands, the average island area for the $10^{16} \text{ Ge}^+ \text{ cm}^{-2}$ ion-mixed electrode is $8.2 \pm 0.9 \mu\text{m}^2$. The island size and implant dose relationship is shown in Figure 4-15.

4.3 Discussion

4.3.1 Effect of Ion Implantation on Fracture Toughness

Measurements of the elastic modulus and hardness of the as-deposited and germanium films were inconsistent from sample to sample, especially in the case of the ion beam-mixed film. A worn out tip with numerous asperities may have given rise to the variations in measurement. Although the average modulus and hardness was higher the ion beam-mixed film, the large errors make the measurements not significantly different than the as-deposited germanium film. Previous nanoindentation experiments suggest that the hardness of a germanium film is not significantly dependent on the ion implantation dose compared to a relaxed amorphous structure across an implant range of 1.0×10^{14} to $5.0 \times 10^{15} \text{ Ge}^+ \text{ cm}^{-2}$ [80]. The biaxial modulus was previously reported to range between 83 GPa and 120 GPa for rf-sputtered amorphous germanium films [69, 81]. Using $\nu = 0.2$ for polycrystalline germanium, the biaxial moduli relate to a range of 66 to 96 GPa for the Young's modulus [82]. At deep penetration the hardness and Young's modulus approach that of the substrate for the $10^{15} \text{ Ge}^+ \text{ cm}^{-2}$ implanted film. Due to the pop-in event, the measurements from deep indentation cannot be physically attributed to the film or substrate.

Phase transformation from the amorphous to a crystalline phase at pressures of 6 – 7 GPa, either the β -Sn structure (Ge-II) or a tetragonal Ge-III structure, can be a source of the pop-in event seen in Figure 4-3 [83]. Figures 4-7 and 4-8 show no alternative phase in the germanium film, so the discontinuity is expected to be due to the film fracture seen in Figure 4-5. Since the approximate radius of the indenter tip is 40 nm and the germanium film thickness is 140 nm, the germanium is expected to avoid phase transformation and deform by shear flow [84]. With no significant differences in elastic properties or phase change, the ion implantation is not expected to have altered the film in any way outside of improving the strength of the interface.

Giant pop-ins caused by indentation of crystalline germanium by a spherical indenter have been largely attributed to lateral cracking beneath the impression [85]. Lateral cracking would likely be induced along the germanium and Ni₈₀Fe₂₀ interface, which is confirmed in Figure 4-6 where the as-deposited film contains a large number of delaminated surfaces. However, evidence of lateral cracking shown by XTEM in Figure 4-7 for the as-deposited germanium film is not very convincing. The germanium films does have clear evidence of radial cracking from Figure 4-5, the likely source of the pop-in event for indentations spaced significantly far apart.

Since the substrate is clearly elastically and plastically deforming during the deep indentation that causes fracture, the W_{t-dp} method is used to eliminate the influence of the deformation [63]. Analyzing the pop-in events for the as-deposited germanium film resulted a fracture energy of 4.82 ± 0.70 pJ ($4,820 \pm 700$ μNnm). The same analysis for the 10^{13} Ge⁺ cm⁻² implanted film yielded a fracture energy of 4.19 ± 0.44 pJ. Using Equation 2-12, the fracture toughness of the as-deposited electrode is calculated to be approximately 0.80 MPam^{-1/2} while the fracture toughness for the implanted sample at least 0.90 MPam^{-1/2}. For the calculation the variables were assigned as $E = 80$ GPa, $\nu = 0.2$, and $N = 1.2$. The value for the number of cracks is estimated from observation; however, since the number indents that had pop-in events was greater than the number of observable fractured indents, it is possible that N is larger. A larger of number of cracks would serve to lower the calculated fracture toughness. Both values for the fracture toughness are larger than what was previously reported for germanium, ranging between $0.5 - 0.6$ MPam^{-1/2} [86, 87].

Radial cracks fracture the germanium through its thickness, so there are two possible mechanisms for the improved fracture toughness. One is that the damage in the implanted sample allows the shear flow to preferentially proceed before fracturing. The second mechanism is that the ion beam-mixing improves the shear strength between the germanium

film and Ni₈₀Fe₂₀ substrate. The substrate is able to constrain the film until the stress is exceeded, where the film slips along the surface or delaminates.

4.3.2 Effect of Ion Implantation on Electrochemical Properties

The ion beam-mixing did not appear to alter in any electrochemical characteristics of the germanium electrode as the cycled electrodes in this study match well with results from other studies [23, 75, 88]. The additional reduction peak that remains just below 0.5 V in Figure 4-11 for the 10¹⁵ Ge⁺ cm⁻² implanted electrode may be attributed to the constant formation of an SEI layer. The as-deposited germanium only exhibits that peak during the first cycle, from Figure 4-10, and it is clear that the ion beam-mixed electrodes experience continual fracture and morphological changes that increase surface area each cycle [43]. The loss of the efficiency for the 10¹⁵ Ge⁺ cm⁻² implanted sample can be explained by the increasing reactive surface area and SEI formation, but it is unclear why the 10¹⁶ Ge⁺ cm⁻² does not behave similarly with respect to efficiency.

All electrodes were able to cycle at least once at comparable capacities, so any influence of the germanium ions doping or otherwise providing better electronic conduction through the oxide layer is minimal at the chosen cycling rate. There is a marked improvement in the cyclability of the germanium electrodes as the implant dose increases with a critical transition occurring somewhere between an implant dose of 10¹⁴ Ge⁺ cm⁻² and 10¹⁵ Ge⁺ cm⁻² from Figure 4-13. A reversible capacity of ~1,600 mAhg⁻¹ is close the theoretical maximum capacity of 1,623 mAhg⁻¹ for Li₂₂Ge₅. There is some debate as to whether the Li₂₂Ge₅ forms during room temperature cycling. Yoon et al. have reported the existence of Li₂₂Ge₅ based on a single x-ray diffraction peak, suggesting that Li₁₅Ge₄ and Li₂₂Ge₅ form together [89]. Baggetto et al. however only identified x-ray diffraction peaks and an extended x-ray fine structure corresponding to the Li₁₅Ge₄ phase [88, 90].

4.3.3 Effect of Ion Implantation on Electrode Failure

Ion beam-mixing both improved the adhesion of the germanium electrode to the substrate and altered the fracture characteristics of the germanium electrode. As the dose increases, the fractured island size decreases. According to Equation 2-12, since the yield stress of germanium and the film thickness are not expected to significantly change from implantation, the decrease in crack spacing is inversely proportional to an increase in interfacial shear strength. Little is known about the yield point for a germanium film undergoing lithiation or delithiation. The yield stress of silicon during lithiation and delithiation has been reported to be approximately 1 – 1.5 GPa, measured using a wafer curvature system [91]. Due to the similar lithiation process between silicon and germanium, location on the periodic table, and mechanical relationships [92], the mechanical properties for delithiation of germanium will be estimated to be 800 MPa, 80% of the value for silicon. Inputting that value of yield stress into Equation 2-15 along with the measured film thickness and approximate crack spacing result in the calculated interfacial shear stress shown in Figure 4-15. Since mechanical information about the lithiation of germanium is uncertain, comparisons between the $10^{13} \text{ Ge}^+ \text{ cm}^{-2}$ and $10^{16} \text{ Ge}^+ \text{ cm}^{-2}$ doses result in an increase of interfacial shear stress by 195%.

4.4 Concluding Remarks

The electrochemical performance of the ion beam-mixed germanium electrodes was investigated. It was shown that increasing ion dose resulted in a concomitant improvement in the cycle life behavior as compared to electrodes not subjected to ion beam-mixing. The ion beam-mixed germanium electrode had better interfacial strength and fractured with smaller crack spacing as the dose increased. The ion beam-mixed films displayed greater peel-off strength compared to the as-deposited film since a similar tape test was not able to remove the ion beam-mixed film from the substrate. Nanoindentation experiments also revealed that the ion beam-mixed films had higher fracture toughness as the dose increased, likely due to the

improved bonding characteristics of the mixed interface. Film fracture could be completely avoided in the $10^{15} \text{ Ge}^+ \text{ cm}^{-2}$ ion beam-mixed film under the experimental conditions, even when indents were nearly on top of each other.

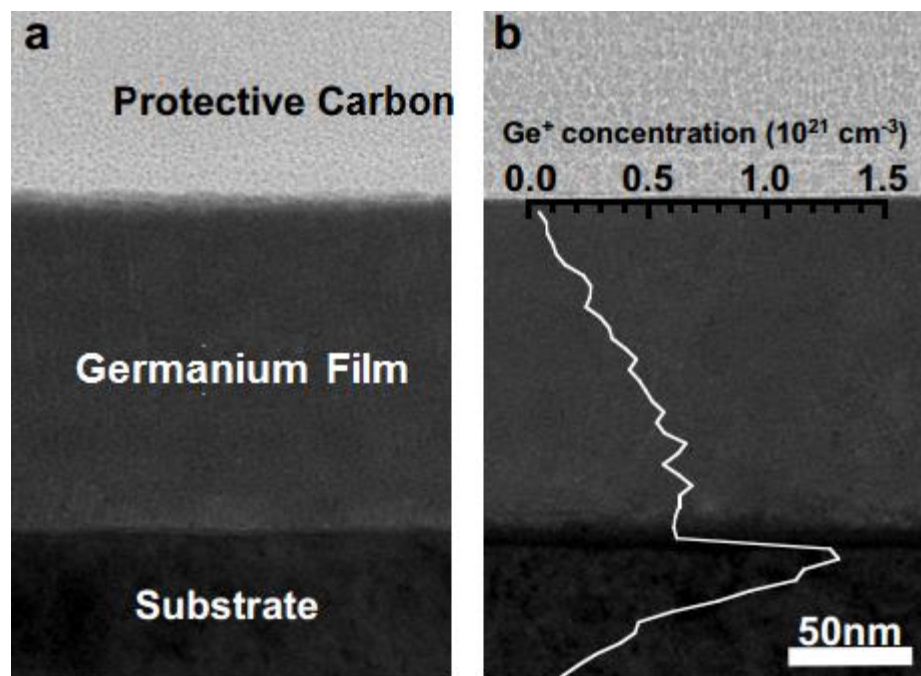


Figure 4-1. XTEM comparison of the germanium electrodes: (a) as-deposited and (b) 10^{15} Ge^+ cm^{-2} ion implanted. The ion implantation profile as predicted from the TRIM code is overlaid in (b).

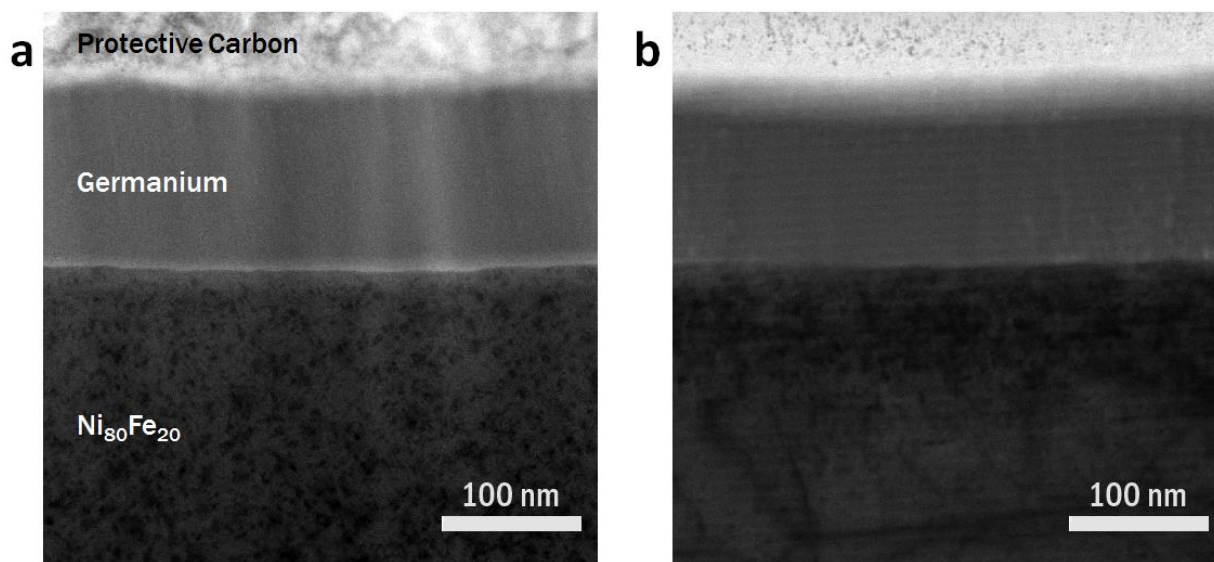


Figure 4-2. STEM bright field images of the current collector interface for the (a) as-deposited and (b) 10^{15} Ge^+ implanted germanium films.

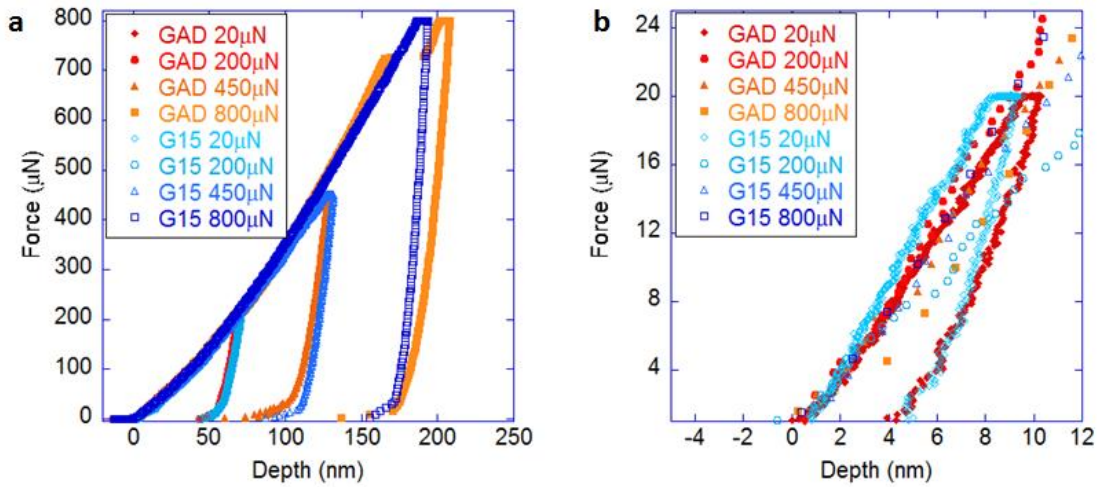


Figure 4-3. Nanoindentation load-depth plots for (a) as-deposited Ge and $10^{15} \text{ Ge}^+ \text{ cm}^{-2}$ implanted Ge film with the shallow indents highlighted in (b).

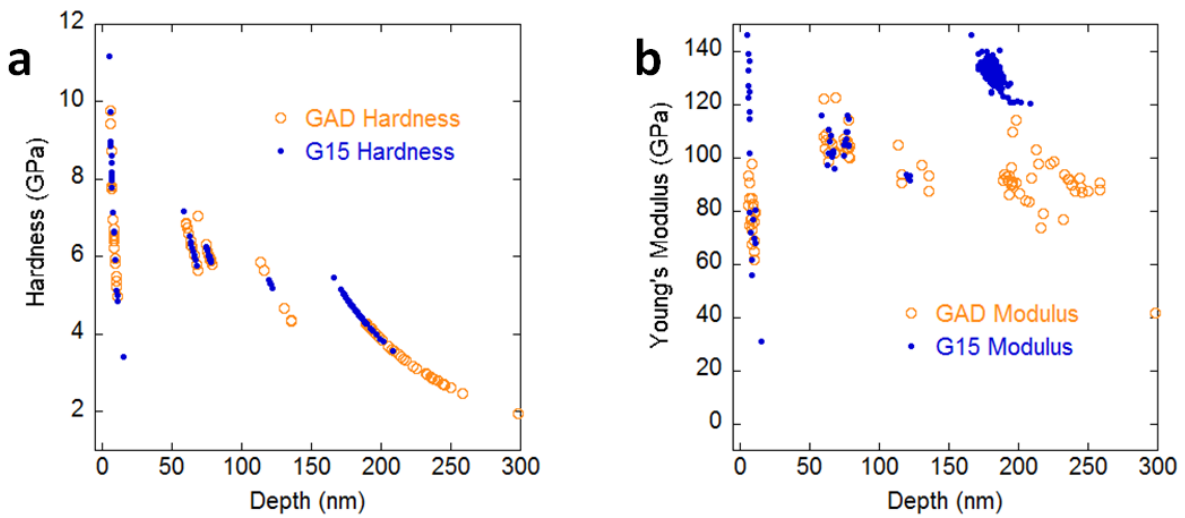


Figure 4-4. Measured mechanical properties of the germanium thin film: (a) hardness and (b) Young's modulus. The as-deposited and $10^{15} \text{ Ge}^+ \text{ cm}^{-2}$ implanted germanium film properties were determined using nanoindentation techniques.

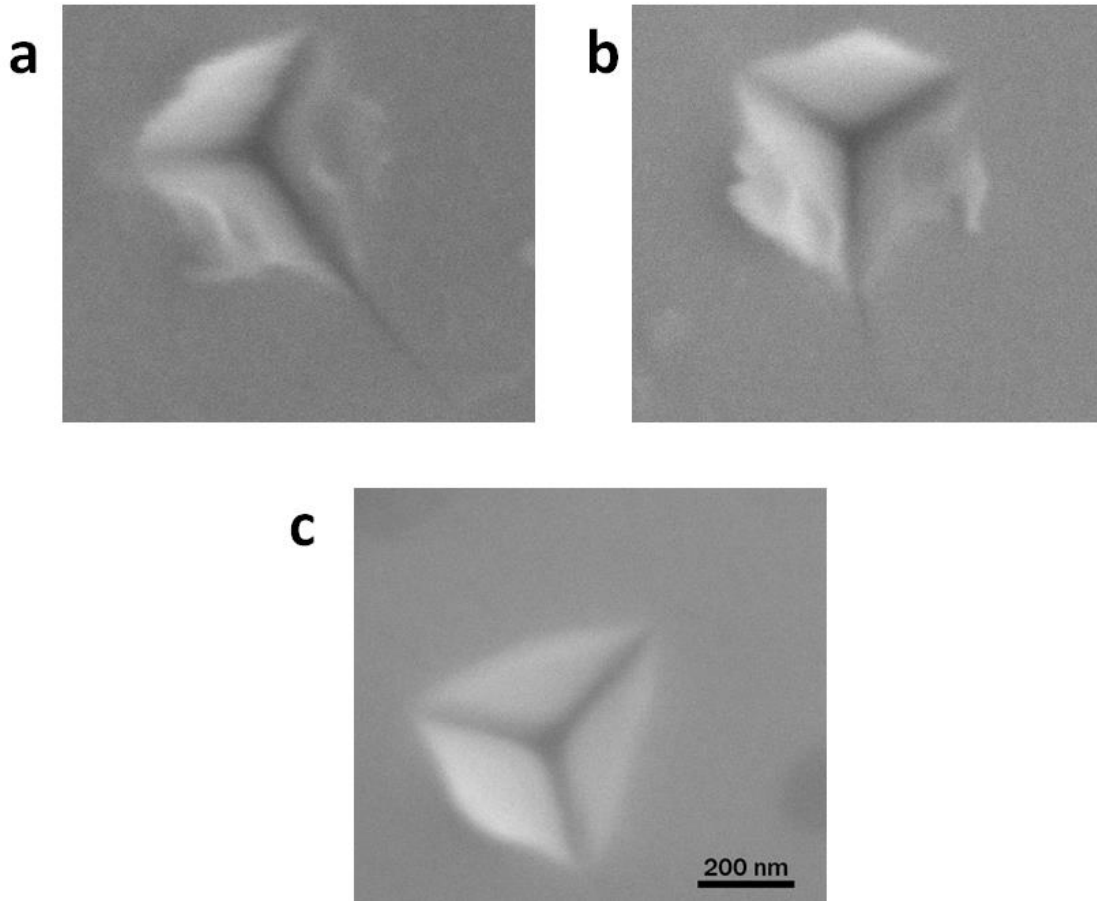


Figure 4-5. Top-down SEM images of nanoindentations at 800 μN for (a) as-deposited Ge, (b) $10^{13} \text{ Ge}^+ \text{ cm}^{-2}$ implanted Ge, and (c) $10^{15} \text{ Ge}^+ \text{ cm}^{-2}$ implanted germanium.

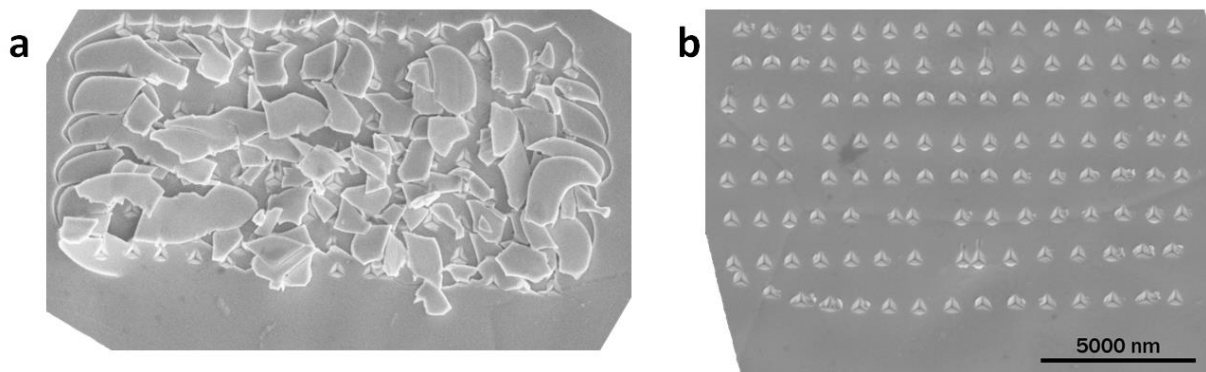


Figure 4-6. Top-down SEM images for an array of nanoindentations at 800 μN for (a) as-deposited Ge and (b) $10^{15} \text{ Ge}^+ \text{ cm}^{-2}$ implanted germanium. There are 120 indents in each 8×15 array with 1 μm expected spacing between indents.

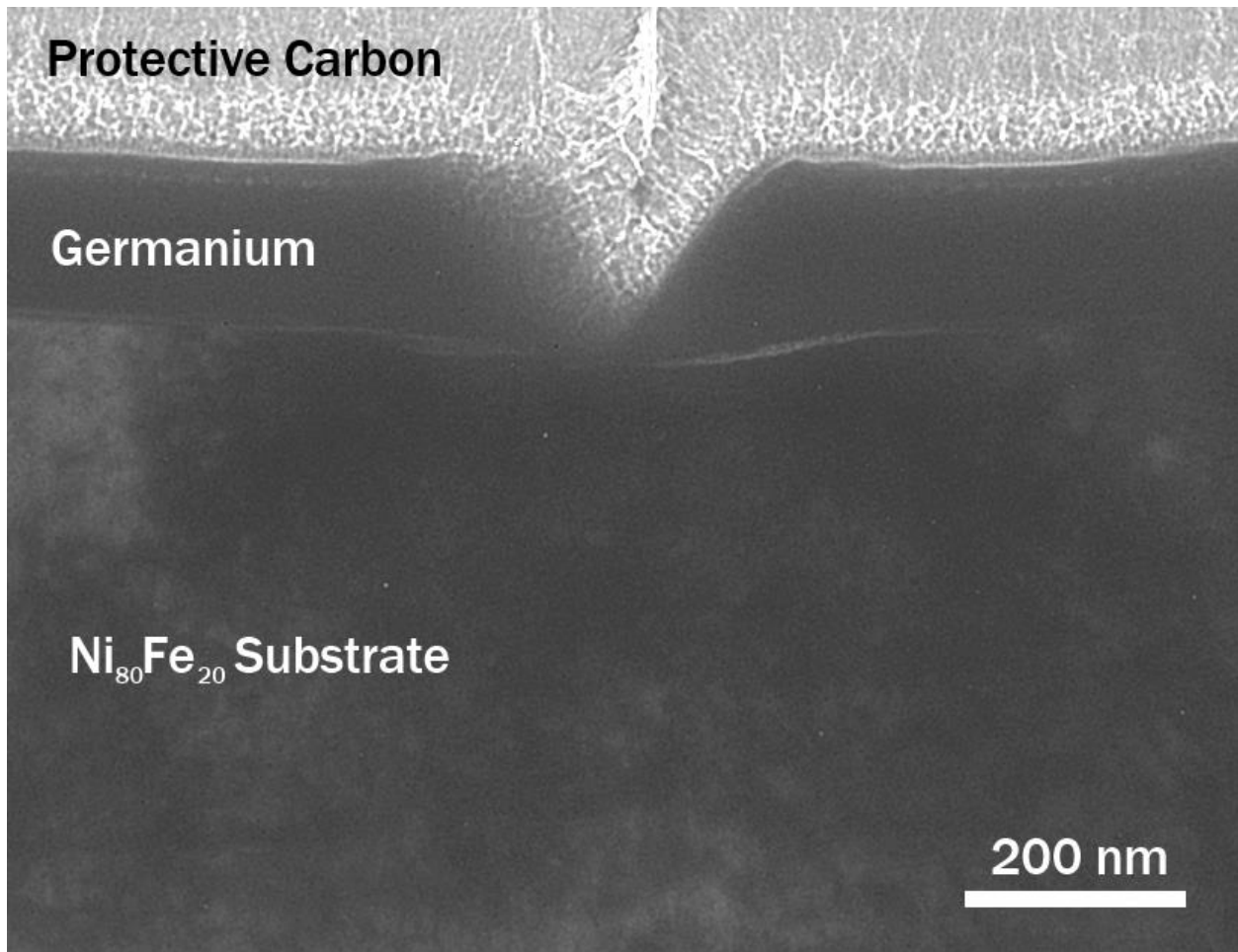


Figure 4-7. XTEM bright field image for an indent at 800 μN into an as-deposited germanium film with 5 μm spacing between indents.

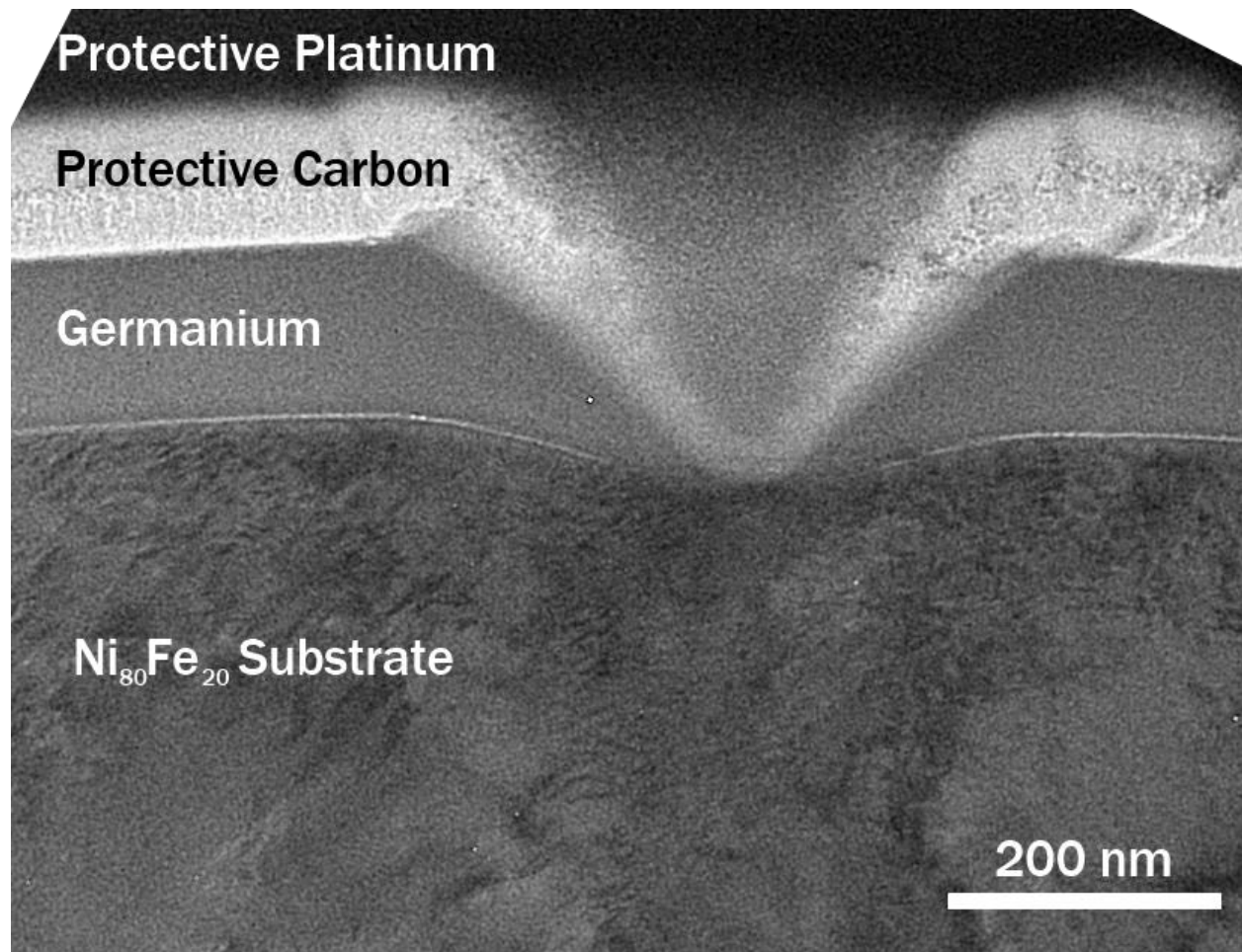


Figure 4-8. XTEM bright field image for an indent at 800 μN into a $10^{15} \text{ Ge}^+ \text{ cm}^{-2}$ implanted germanium film with 1 μm spacing between indents.

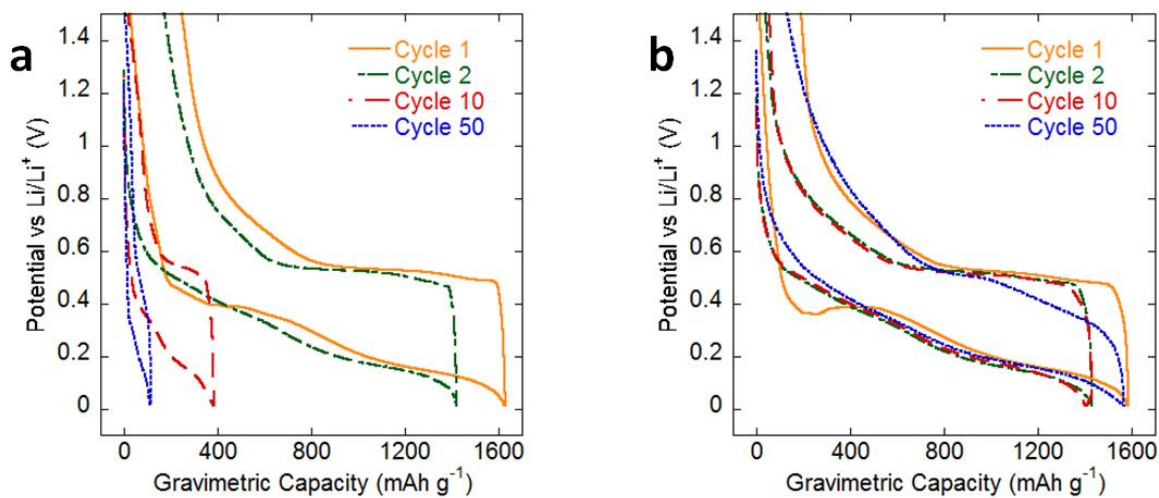


Figure 4-9. Galvanostatic cycling of the germanium film at 810 mAhg^{-1} for (a) as-deposited electrode and (b) 10^{15} Ge^+ ion beam-mixed electrode.

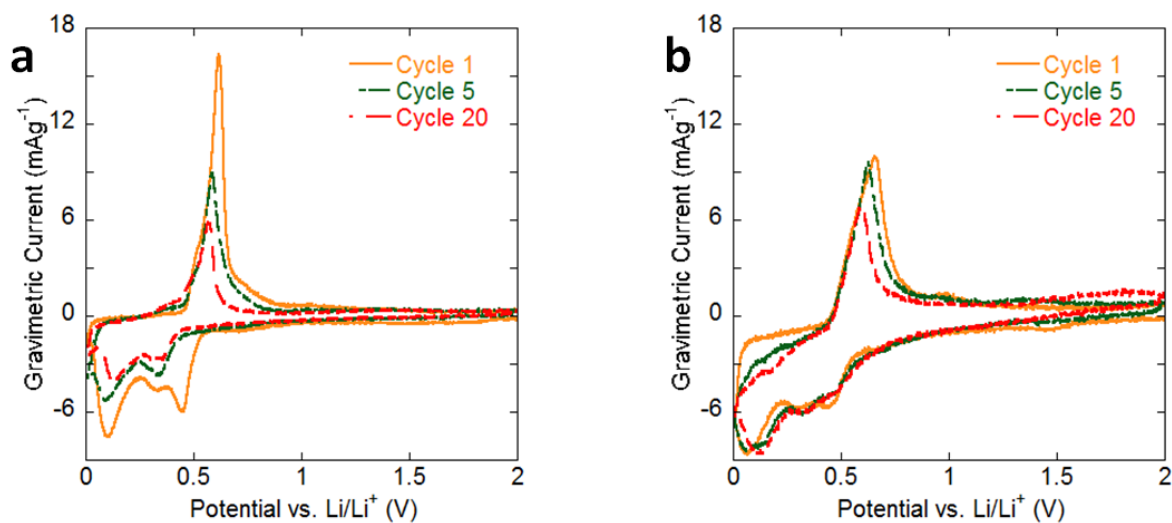


Figure 4-10. Cyclic voltammograms at a sweep rate of $278 \mu\text{Vs}^{-1}$ for cycles 1, 5, and 20 of the germanium film: (a) as-deposited electrode and (b) 10^{15} Ge^+ ion beam-mixed electrode.

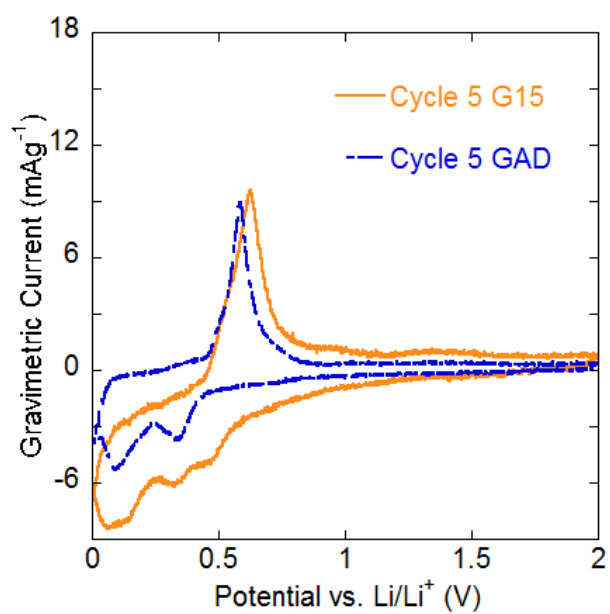


Figure 4-11. Cyclic voltammogram at a sweep rate of $278 \mu\text{Vs}^{-1}$ for cycle 5 of the as-deposited germanium electrode and 10^{15} Ge^+ ion beam-mixed germanium electrode.

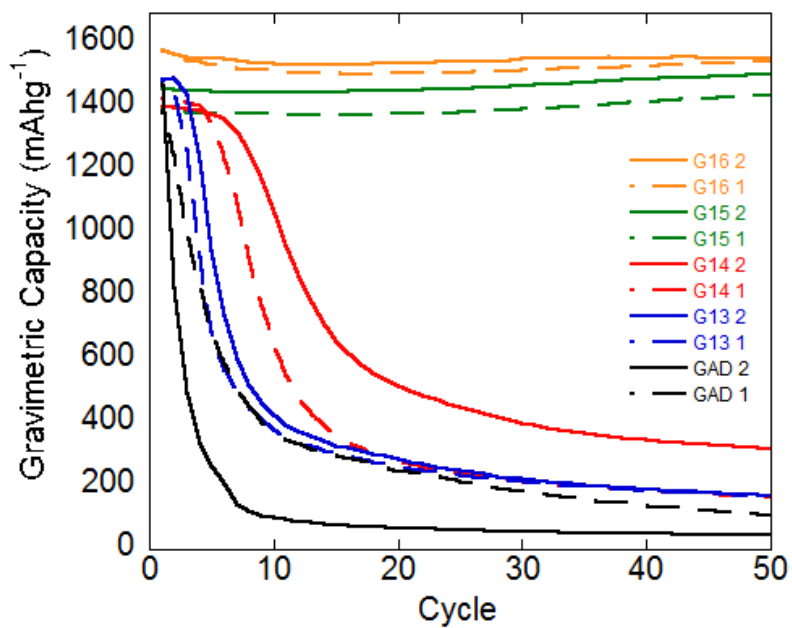


Figure 4-12. Cycle life plot of each as-deposited and implanted germanium electrode galvanostatically cycled at 810 mAhg^{-1} for 50 cycles. Only the discharge capacities are shown for each sample.

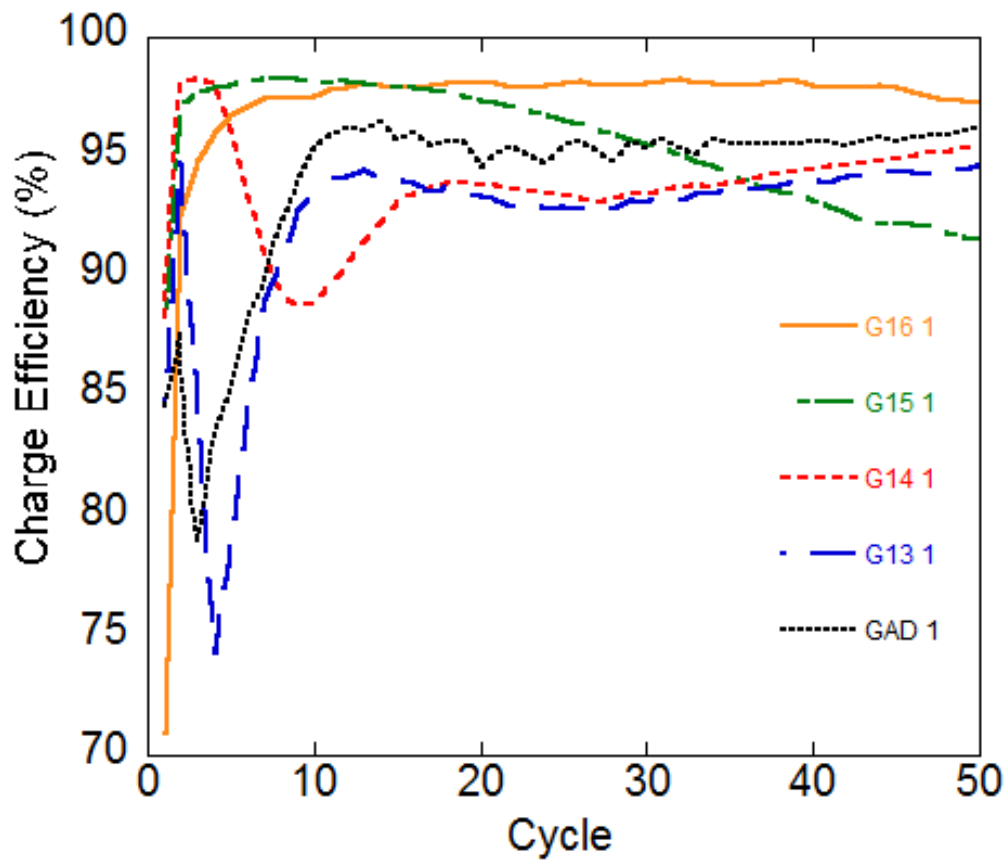


Figure 4-13. Charge efficiency of select as-deposited and implanted germanium electrodes galvanostatically cycled at 810 mAhg^{-1} for 50 cycles. The charge capacity was greater than the discharge capacity for all cycles and samples.

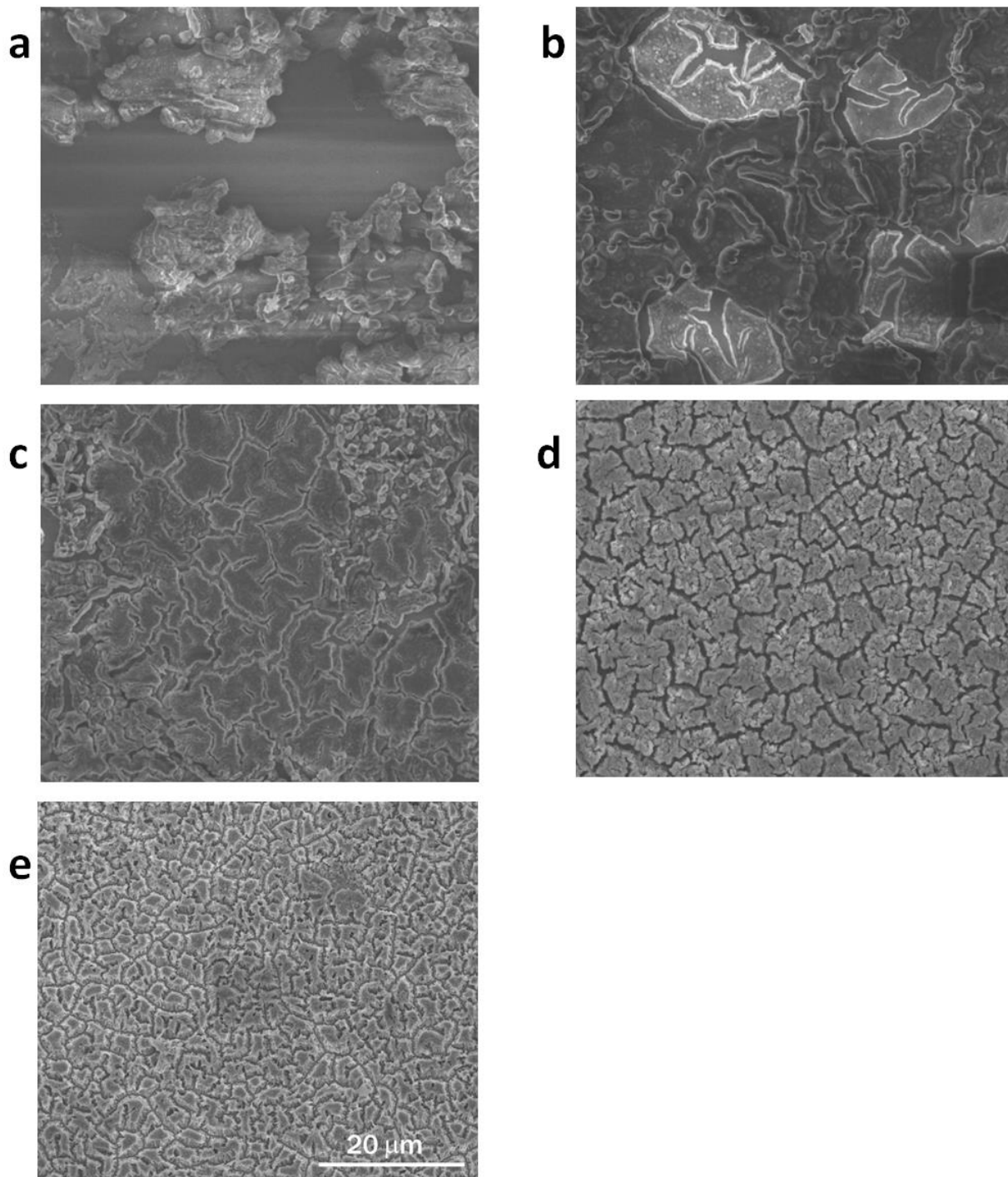


Figure 4-14. Top-down SEM images of cycled germanium electrodes at 810 mAhg⁻¹ after 50 cycles: (a) as-deposited germanium electrode, (b) 10¹³ Ge⁺ cm⁻² implanted electrode, (c) 10¹⁴ Ge⁺ cm⁻² implanted electrode, (d) 10¹⁵ Ge⁺ cm⁻² implanted electrode, and (e) 10¹⁶ Ge⁺ cm⁻² implanted electrode.

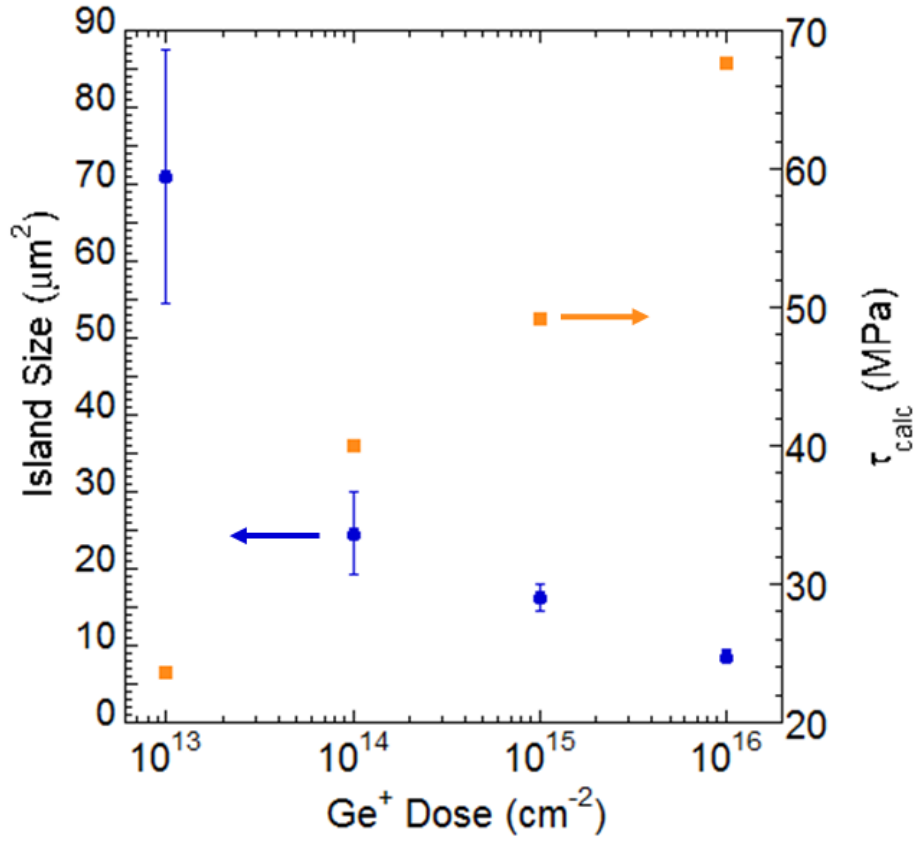


Figure 4-15. Relationship between cracked surface island size and Ge⁺ implant dose. The interfacial shear stress is estimated from the average island size.

CHAPTER 5

ION BEAM-MIXED SILICON ELECTRODES

The investigation of silicon as a possible anode material for secondary lithium ion batteries began in 1976 as Sharma and Seefurth studied the $\text{Li}_x\text{Si}/\text{FeS}_2$ molten salt battery [93]. One primary problem with lithium-silicon electrodes was corrosion of common electrode contacts, such as stainless steel [73]. In 1981, Boukamp et al. identified the formation of the $\text{Li}_{12}\text{Si}_7$, $\text{Li}_{14}\text{Si}_6$, $\text{Li}_{13}\text{Si}_4$, and $\text{Li}_{22}\text{Si}_5$ stoichiometries and stabilities [94]. As the development of room temperature Li-ion chemistries progressed, silicon fell out of favor due to the low Li-ion diffusivity at room temperature with reported values ranging between $10^{-12} - 10^{-14} \text{ cm}^2\text{s}^{-1}$, with a typically accepted value of $10^{12} \text{ cm}^2\text{s}^{-1}$ [64, 74, 95].

Amorphous silicon was first showed potential as a stand-alone anode at room temperature in 1999, when a 1.2 μm thin film deposited by CVD onto a porous nickel substrate showed a reversible capacity of $\sim 1,000 \text{ mAhg}^{-1}$ for three cycles at a C/2 rate [96]. Thin films of silicon approximately 100 nm and nanoparticles were shown to avoid fracture and cycle at a reversible capacity of $\sim 2,000 \text{ mAhg}^{-1}$ over 50 cycles [64]. A large volume expansion of $\sim 400\%$ during lithium insertion [94] pushed further silicon research to the nanoscale to address the problems of high internal stresses and creating structures that were smaller than the critical fracture dimensions. Research of silicon at the nanoscale has led to a better understand of the lithiation process, but studies of the interface between silicon and the current collector often concerns binders in composite systems [97-100]. While it is generally understood that better adhesion to a current collector would improve cyclability, the interfaces in non-binder systems are often overlooked or underreported.

One technique to improve adhesion and minimize fracture is to use a porous current collector [96, 101-103]. Substrate grinding and an elastomeric substrate from Chapter 1 have also shown improvements. Silicon multilayer stacks with iron, yttrium, and carbon have been

shown to relieve the strain due to expansion and improve cyclability and rate capability [104-106]. Patterned silicon films beneath a certain size can also avoid fracture as the islands could either plastically or elastically slip along of the surface of the substrate [66, 107, 108]. In this chapter, the role of the ion dose will be investigated in relation to cycling performance and adhesion through fracture analysis.

5.1 Experiments

5.1.1 Sample Preparation

A 350 nm thin film of amorphous silicon was deposited on a 304 SS substrate using PECVD. The thin film was implanted with ion doses of $10^{13} - 10^{16} \text{ Si}^+ \text{ cm}^{-2}$. Silicon was chosen as the implant species to prevent doping which could improve electrical conduction of the silicon. The only effect of the implanted ion should be towards ion beam-mixing. The implant voltage was 250 kV with a beam current of 500 nAcm^{-2} . At a 250 kV accelerating voltage, the peak of the Si^+ implant profile would be approximately at the interface between the silicon film and substrate. The implant performed at room temperature. The electrodes were prepared in the pouch cell configuration as described in Chapter 2.2.

5.1.2 Electrochemistry

The as-deposited and implanted films were galvanostatically tested for 100 cycles between the voltage range of 0.01 – 1.5 V. The applied current was equal to 4.2 Ag^{-1} , which corresponds to a cycling rate of C/1 for the $\text{Li}_{22}\text{Si}_5$ endpoint or $\sim 1.2\text{C}$ for the $\text{Li}_{15}\text{Si}_4$ endpoint. The samples were also tested with cyclic voltammetry with a sweep rate of $417 \mu\text{Vs}^{-1}$ across the same 0.01 – 1.5 V range. The microstructure of cycled electrodes were observed under SEM to determine the average fractured island size. The microstructure of the cycled electrodes were also observed using XTEM and STEM. A modified pouch cell explained in Chapter 2.2.1 was also designed to allow the investigation of film fracture through OM. These electrodes were also galvanostatically cycled between 0.01 – 1.5 V at 4.2 Ag^{-1} .

5.2 Results

5.2.1 Sample Characterization

An XTEM image of the implanted and as-deposited silicon thin film is compared in Figure 5-1. The implanted sample show no detectable differences with the as-deposited sample. An estimate of the ion implantation profile use the TRIM code is also overlaid for comparison.

5.2.2 Electrochemistry

The charge and discharge curves of the as-deposited silicon electrode and $10^{16} \text{ Si}^+ \text{ cm}^{-2}$ ion-mixed electrode cycled at the 4.2 Ag^{-1} rate are shown in Figure 5-2. The as-deposited silicon electrode shows a reduction in capacity during cycling and large irreversible capacity loss during the first cycle. For this sample, the first cycle discharge (charge) capacity is 1656 (3485) mAhg^{-1} , yielding a charge efficiency of 47.5%. The second cycle has a discharge (charge) capacity of 1370 (1848) mAhg^{-1} with a charge efficiency of 74.1%. For cycle twenty the discharge (charge) capacity was 426 (421) mAhg^{-1} with a charge efficiency of 101%. For cycle one hundred, the discharge (charge) capacity was 328 (326) mAhg^{-1} with a charge efficiency of 101%.

The ion beam-mixed electrode also exhibits capacity fade over the one hundred cycles but a reduced rate. The ion beam-mixed electrode also has a large irreversible capacity loss during the first cycle. For this sample, the first cycle discharge (charge) capacity is 2,819 (4,279) mAhg^{-1} , yielding a charge efficiency of 65.9%. The second cycle has a discharge (charge) capacity of 2,772 (3,009) mAhg^{-1} with a charge efficiency of 92.1%. For cycle twenty the discharge (charge) capacity was 2,680 (2,723) mAhg^{-1} with a charge efficiency of 98.4%. For cycle one hundred, the discharge (charge) capacity was 1,802 (1,840) mAhg^{-1} with a charge efficiency of 97.9%. The charge and discharge curves are not entirely reproducible as cycling progresses. During the first charge cycle for each electrode, the electrode has a plateau shape

between 0.1 and 0.2 V vs Li/Li⁺ before while cycles after the first show a constant gradient this reproduced.

The CV profiles of the first, fifth, and twentieth cycles of an as-deposited silicon electrode, a 10¹³ Si⁺ cm⁻², and a 10¹⁶ Si⁺ cm⁻² ion beam-mixed silicon electrode can be compared in Figure 5-3. In the first cycle of all of the electrodes, the current characteristics appear suppressed with a small reduction peak at 0.74 V vs Li/Li⁺ and another from 0.01 – 0.3 V vs Li/Li⁺. The reduction peak at 0.74 V vs Li/Li⁺ vanishes as cycling continues. The first cycle of each electrode also shows a broad oxidation peak at 0.5 V vs Li/Li⁺, which is consistent with the delithiation of silicon. The as-deposited sample retains a similar shape of the first cycle during the second cycle but at an increased current. As cycling progresses, the twentieth cycle has a decreased current response and the delithiation peak is shifted to 0.36 V vs Li/Li⁺. The ion beam-mixed electrodes have more similar characteristics. In both samples, the magnitude of the gravimetric current increases as cycling progresses. Whereas the 10¹³ Si⁺ cm⁻² implanted electrode exhibits peak broadening, the 10¹⁶ Si⁺ cm⁻² implanted electrode clearly forms dual peaks. The peak locations are at 0.016 and 0.16 V vs Li/Li⁺ during lithiation. During delithiation the peaks are at 0.38 and 0.51 V vs Li/Li⁺. The shoulders of the dual peaks can be seen in the 10¹³ Si⁺ cm⁻² implanted silicon electrode, suggesting that evolution might progress as with the 10¹⁶ Si⁺ cm⁻² implanted electrode. The magnitude of the current response is plotted against the testing time in Figure 5-4. The as-deposited sample reached a peak current magnitude during cycle three and is followed by a decrease. The ion beam-mixed samples also reach a peak current magnitude during cycle three but is stable for the following cycles.

Representative cycle life behavior of the as-deposited and ion beam-mixed silicon electrodes can be seen in Figure 5-5. The as-deposited silicon electrode fails rapidly, losing over 70% of its total capacity within ten cycles. The 10¹³ – 10¹⁵ Si⁺ cm⁻² implanted electrodes are significantly better than the as-deposited electrode up to about cycle forty, then also losing

its capacity rapidly. While the plotted 10^{15} Si⁺ cm⁻² implanted electrode retains of modest capacity over 1,000 mAhg⁻¹ for the rest of its cycle life, other electrodes of that batch failed similarly to the plotted 10^{13} and 10^{14} Si⁺ cm⁻² implanted electrodes. The 10^{16} Si⁺ cm⁻² implanted electrode does not exhibit any drastic failure mode over one hundred cycles, although the capacity does gradually decline.

Across all samples, the initial charge capacity did not systematically vary from implant dose and had a gravimetric capacity of $3,386 \pm 361$ mAhg⁻¹. In comparing the fourth cycle charge capacity to the first cycle charge capacity for the ion beam-mixed electrodes, there was an average loss of 837 ± 242 mAhg⁻¹. The as-deposited electrodes had an average charge efficiency of $54.4 \pm 8.2\%$ during the first cycle. The efficiencies improved to $98.5 \pm 0.5\%$ after the third cycle although the capacity was drastically decreased. The ion beam-mixed electrodes had an average charge efficiency of $75.1 \pm 10.3\%$ during the first cycle. The efficiencies improved to $95.8 \pm 1.7\%$ after the third cycle. The average capacity decays rates from the ion beam-mixed samples from cycles four to thirty in order of ascending ion dose were $0.83 \pm 0.28\%$, $0.54 \pm 0.43\%$, $0.07 \pm 0.06\%$, and $0.03 \pm 0.07\%$. The decay rate during the sharp decline of the ion beam-mixed samples peak at 6% per cycle. As a point of average, the cycle at which the average electrode drops under 2,000 mAhg⁻¹ were cycles two, thirty-six, forty-two, forty-seven, and one hundred in order of ascending ion dose.

5.2.3 Cycling Induced Fracture

The delamination and film fracture was verified using SEM as shown in Figure 5-6, which presents low-magnification images of as-deposited and ion beam-mixed electrodes after galvanostatic cycling for 1 cycle at 4.2 Ahg⁻¹. In the as-deposited case there is large-scale delamination of the electrode from the current collector. In contrast, for the case of an ion beam-mixed electrode Si⁺-implanted to a dose of 10^{16} cm⁻², the electrode exhibits coarse through-thickness cracking, but remains in contact with the current collector.

The finer structure of the ion beam-mixed electrodes Si⁺-implanted to doses of 10¹³, 10¹⁴, 10¹⁵, and 10¹⁶ cm⁻² after galvanostatic cycling at 4.2 Ag⁻¹ for one hundred cycles was investigated using top-down SEM as shown in Figure 5-7. The as-deposited electrode did not have a well-defined crack spacing or island shape, so no measurements were made. Based off of measurements of 1,616 islands, the average island area for the 10¹³ Si⁺ cm⁻² ion-mixed electrode is 39.6 ± 2.4 μm². From the measurements of 1,233 islands, the average island area for the 10¹⁴ Si⁺ cm⁻² ion-mixed electrode is 31.6 ± 1.1 μm². Based off of measurements of 657 islands, the average island area for the 10¹⁵ Si⁺ cm⁻² ion-mixed electrode is 21.8 ± 1.2 μm². From the measurements of 523 islands, the average island area for the 10¹⁶ Si⁺ cm⁻² ion-mixed electrode is 15.3 ± 0.7 μm². The island size as a function of implant dose is plotted in Figure 5-8. Additionally, the measured perimeters were 29.3 ± 0.4, 25.3 ± 0.8, 19.5 ± 1.3, and 14.6 ± 0.4 μm in order of ascending ion dose. The circularity shape descriptors were 0.570 ± 0.007, 0.577 ± 0.009, 0.559 ± 0.001, and 0.611 ± 0.011 in order of ascending ion dose, which is shown in Figure 5-9.

A cross-section of a discharged 10¹³ Si⁺ cm⁻² implanted silicon electrode can be seen in the XTEM image of Figure 5-10 after ten cycles. A high resolution image of the amorphous silicon reveals a unique nanostructure, although the film remains amorphous. The region of the silicon film near the interface appears to be of a lower density than the rest of the film and porous. A high resolution image of the interfacial layer and silicon can be seen in Figure 5-11. The silicon also has a porous nanostructure with pore diameters of approximately 5 – 10 nm. An EDS line scan reveals that the surface oxide of the steel has been delaminated and resides within that region, however the silicon signal is negligible.

Figure 5-12 shows a XTEM image of a discharged 10¹⁶ Si⁺ cm⁻² implanted silicon electrode and a corresponding EDS line scan. This and following samples were coated with a Au/Pd protective layer rather than carbon in order to provide better clarity about of the location

of the island interfaces. The XTEM image shows that the island heights do not vary much from island to island. The EDS line scan once again shows the presence of an oxide at the interface between the silicon film and substrate. The porous interlayer previously seen exists all around the silicon island. The expansion of the cycled $10^{16} \text{ Si}^+ \text{ cm}^{-2}$ implanted silicon electrodes can be seen in Figure 5-13. After one complete cycle, the silicon has a thickness of 500 nm which corresponds to an expansion of 42.9%. After fifty cycles, the silicon has a thickness of 870 nm which corresponds to a growth rate of approximately 7.6 nm per cycle. After one hundred cycles, the silicon has a thickness of 1400 nm which corresponds to a growth rate of approximately 10.6 nm per cycle from cycle fifty. The growth rate is estimated to be approximately 9.1 nm per cycle from the first cycle to last.

Unlike the previous observed electrodes, the $10^{16} \text{ Si}^+ \text{ cm}^{-2}$ implanted silicon electrode cycled one hundred times shows a considerable growth of the porous interlayer in Figure 5-14. The EDS line scan reveals a faint silicon, carbon, and oxygen signal as the collected counts are low in general. Also unlike the previous observed electrodes, there is no delaminated oxide layer at the interface. A similar analysis of the neighboring island can be seen in Figure 5-15. This island shows a variation in constant across its entire thickness, although an oval shaped feature stands out. An EDS line scan across that features reveals iron and chromium from the 304 SS substrate. Between the 304 SS substrate and oval-shaped particle is a lower density silicon layer. The nanostructure of the cycled island is also characterized in Figure 5-16 by dark field STEM. The center of the island is eroded in the shape of circular pockets with a filament structure protruding out the edges. The center of the silicon island also reveals nanoporosity.

5.2.4 In-situ Optical Microscopy

The fracture of the as-deposited electrode is shown through time lapse images during discharge in Figure 5-17. These electrodes were cycled under the same conditions as the rest of the experiment, between 0.01 V – 1.5 V at 4.2 A g^{-1} . The crack pattern progresses

continuously. Compared to the crack pattern of the 10^{16} Si⁺ cm⁻² ion beam-mixed electrode in Figure 5-18, the crack spacing is large for the as-deposited electrode. During cycling these islands bow away from the surface along the edges. During charging, both electrodes expand to form a near continuous surface again.

5.3 Discussion

5.3.1 Effect of Ion Implantation on Electrochemical Properties

The ion beam-mixing did not appear to alter any electrochemical characteristics of the silicon electrode, in terms of introducing new reactions. The large first cycle inefficiency is typical amongst silicon electrodes, and has been attributed to the reaction of lithium with the native oxide on silicon, formation of an SEI layer, or structural changes from the initial state of the material to one that accommodates lithiation [64, 109]. Part of the inefficiency can also be attributed to the loss of electrode material during fracture, specifically for the as-deposited silicon film.

One interesting difference between the first and later charge cycles is the plateau and sloping regions shown in Figure 5-2. The plateau suggests a two phase lithiation process while the sloping region relates to a single phase process. While there has been debate as to the whether amorphous silicon proceeds via a one or two phase reaction mechanism, recent in-situ TEM experiments revealed a phase boundary between Li_xSi and amorphous silicon [110, 111]. After the first cycle, a single phase reaction method proceeded. Structural changes due to delithiation or residual lithium left in the silicon may make it easier to break the silicon matrix [110].

The CV profiles of the ion beam-mixed electrodes match well with results from other studies [19, 109, 112]. The dual peak structure corresponds to the low and high voltage insertion or extraction of lithium with an amorphous lithium silicide [112]. Increasing the sweep rate in the CV experiment causes the high voltage lithium extraction to become more prominent

[109]. That results indicates a kinetic limitation that could explain why the peak is larger at the early stages of cycling in Figure 5-3, and the lower voltage peak becomes more prominent in the later stages of cycling due to the increased surface area from fracture and nanoporosity. That also explains why the 10^{16} Si⁺ cm⁻² implanted electrode has the most prominent low voltage extraction peak since its average island size is the smallest. The increase in the current amplitude can also be described by the microstructural changes [27].

The reduction peak around 0.7 V could be attributed to reduction of the surface oxide of silicon, as silica has a reduction potential of 0.69 vs Li/Li⁺ [113]. A thin film SiO₂ electrode had a prominent reduction peak at 0.77 V vs Li/Li⁺ [114]. This layer likely contributes to an increased cell impedance. Regarding the interfacial oxide layer, α -Fe₂O₃ was reported to have reduction peaks at 0.63 and 1.2 V and oxidation peaks at 1.0 and 1.8 V vs Li/Li⁺ [115]. The reduction peaks are not well defined, which may be expected considering both the low mass and requirement of lithium diffusion through silicon. There is a small oxidation peak around 1.0 V vs Li/Li⁺ which cannot be explained by silicon alone. Reports of pitting of the stainless steel current collector and self-discharge of lithium-sulfur cells have been reported, although no figure was provided [116]. Figure 5-14 may support pitting since the curvature of the 304 SS substrate matches that of the reacted plume of the interlayer. A small steel burr is also seen near the reacted area where the local steel surface appears lower than its surroundings. Corrosion of SS from a coin cell casing when held at high potentials was attributed to the breakdown of the LiPF₆ electrolyte with trace water content to form HF [117]. While it is possible that such a mechanism occurs during cycling, the layer still contains oxygen. A reacted LDX 2101 SS electrode developed a structure of an SEI layer at the surface, a (Cr, Fe) fluoride layer below the SEI layer, a hydroxide layer (Cr) underneath, an oxide layer (Fe, Cr, Mo), and then the metal substrate [118]. A fluorine signal from any EDS line scan gives an ambiguous result since the peak position of fluorine is K α = 0.677 keV while iron has a L α peak at 0.705 keV.

The silicon electrodes also showed poor performance in terms of current response for the first cycle during the CV tests of Figure 5-3, while the cycled electrodes generally exhibited their highest capacity during the galvanostatic testing of Figure 5-2. The suppressed features could be explained by incomplete lithiation. The as-deposited (-7.2 Ag^{-1}) and $10^{13} \text{ Si}^+ \text{ cm}^{-2}$ (-6.2 Ag^{-1}) implanted electrodes both were charging at a rate beyond the galvanostatic rate (-4.2 Ag^{-1}) at low voltages, and two-phase reaction may be been diffusion limited under those conditions. A similar behavior was occasionally seen in the galvanostatic tests where an electrode would remain inactive for a number of cycles before starting. These “delayed start” electrodes were not included in the measurements and analysis, only those at began cycling as expected during the first cycle. The delayed start electrodes could remain dormant from anywhere between one and seven hundred cycles. Other electrodes were never able to be cycled, or at least attempts were halted before they could. There has only been one reported incidence of the delayed start electrode in the literature [119].

The role of the oxide at the interface between the silicon film and 304 SS substrate does not prevent the as-deposited or ion beam-mixed electrodes from attaining full lithiation. There is a marked improvement in the cyclability of the silicon electrodes as the implant dose increases with one of two critical transition occurring somewhere between as-deposited and a dose of $10^{13} \text{ Si}^+ \text{ cm}^{-2}$. The second transition occurs somewhere between doses of $10^{15} \text{ Si}^+ \text{ cm}^{-2}$ and $10^{16} \text{ Si}^+ \text{ cm}^{-2}$. The results are consistent with the prevention of the loss of electrical contact due to improved adhesion. The average first cycle charge capacity of $\sim 3390 \text{ mAhg}^{-1}$ is 94.4% of the theoretical gravimetric capacity for the $\text{Li}_{15}\text{Si}_4$ phase, the highest lithiated phase reported for amorphous silicon [94].

5.3.2 Effect of Ion Implantation on Electrode Failure

Ion beam-mixing resulted in improved adhesion of the silicon electrode to the 304 SS substrate, similar to the improvements of the silicon electrode from Chapter 4. Using Equation

2-15, the estimated value for interfacial shear stress due to ion beam-mixing can be seen in Figure 5-8. A yield stress of 1 GPa was used in the calculation, since that was the stress measured during lithium extraction [91]. An average yield stress of 720 MPa was also measured by an in-situ tensile test on a lithiated nanowire of the $\text{Li}_{15}\text{Si}_4$ composition [120]. The additional metallic Li – Li and weak ionic Li – Si bonds result in a much lower Young's modulus than silicon, with weak shear resistance and ability to accommodate more plastic strain [121, 122].

Li et al. have previously characterized fractured surfaces of thin film silicon electrodes of varying thickness deposited by sputtering on a 430 SS substrate and galvanostatically cycled at a C/10 rate. The average island area of the silicon electrodes decreased as the film thickness decreased, as expected from Equation 2-15. The average island area for a 350 nm was between 10 – 20 μm^2 , which corresponds to electrodes ion beam-mixed at doses of 10^{15} to 10^{16} $\text{Si}^+ \text{cm}^{-2}$ in this study. It is unclear if the differences arise from sample preparation, the deposition method, or cycling rate. The fractal dimension was also reported for the cracked electrode surface, where a dimension of 2.0 was approached for thicker films and a value of 1.57 for a 200 nm film [123]. Figure 5-9 shows the relationship between the perimeter and the island area from this study which has a fractal dimension of ~ 0.52 , using Equation 2-17. The ion beam-mixed electrodes retain a similar shape whether the crack separation distance is large or small. The best-fit fractal dimensions for each implant are 0.473, 0.522, 0.532, and 0.547 in order of ascending dose.

Another descriptor for the island shape is its circularity using Equation 2-18. The mean circularity of the islands across the range of implant doses is plotted in Figure 5-9. Outside of the 10^{15} $\text{Si}^+ \text{cm}^{-2}$ dose, the circularity appears to increase as the dose increases. Although a circular shape was estimated from an approximate calculation of the interfacial shear stress, it is clear from both the circularity measurement and visual interpretation that the islands are not

well approximated by circles. On average the islands have a rectangular shape from both a top-down and cross-sectional projection. With crystalline silicon, anisotropy arises as a result of an interface limited reaction with different rates at different crystal planes, so that nanopillars with different axial directions can create with cross, ellipse, or hexagonal shapes [124-127]. Such anisotropy should not be expected in an amorphous silicon film.

While the effect of ion implantation is evident, the role it plays after the first cycle is questionable. In Figures 5-17 and 5-18 the electrodes are shown to fracture into different sized features during the first discharge cycle, likely governed by the increased adhesion due to the ion beam-mixing. As cycling continues, the XTEM images of Figures 5-10, 5-11, 5-12, and 5-13 show that the silicon is no longer in contact with the substrate and replaced with an unidentified interlayer. This interlayer likely allows the islands to easily expand and contract on the surface of the 304 SS without catastrophic failure along the interface. If that is the case, the role of ion beam-mixing is just to modulate the fracture dimensions. Buckling, bowing, or further fracture of the silicon film may lead to delamination of the interlayer or progressively weaken the contact through fatigue.

5.3.3 Deformations at the Nanoscale

The most curious feature of the cycled electrodes is the presence of the metallic inclusion of steel within the silicon film. One problem with XTEM samples is the incredibly small sampling volume, so it is possible that the metal inclusion exists simply as a cross-section of a larger particle that was sitting on the steel surface. There was no indication that the silicon island was propped up to an exceptional height when selecting a site using the FIB/SEM. Other cycled samples also contained steel related features within the silicon film, usually associated with a variation in contrast within the silicon islands. For example, in Figure 5-12 the silicon exists as a rectangular cross-section of a uniform contrast with a reacted region along the perimeter. In Figure 5-14, the silicon region is no longer rectangular but still of a fairly uniform

contrast. Figure 5-15 however contains the steel inclusion and has band-like contrast variations. Bulk diffusion or electromigration of the iron and chromium into the silicon seems unlikely at room temperature and at the small currents. It is currently unclear what is the source or mechanism of formation for the steel inclusions.

Nanoporosity of silicon has been reported previously but is not well understood. Porosity was evident in silicon nanowires during an in-situ tensile stress experiment where they were ascribed to have formed from either void nucleation during loading or partial delithiation under tension [120]. Porosity has also been reported to form during the delithiation of silicon nanowires cycled with in-situ TEM [128]. The suggested mechanism that atomic diffusion of silicon is slow so pores are formed as a metastable structure [128]. The pore generation can explain the increase in the thickness of the cycled electrodes from Figure 5-13. Since only a single cross-section was imaged, it is unknown if the pores are discrete spherical objects or form a channel network through the silicon. If all the pores are connected then that can act as a fast transport pathway for further cycling.

5.4 Concluding Remarks

The electrochemical performance of the ion beam-mixed silicon electrodes was investigated. It was shown that increasing ion dose resulted in a concomitant improvement in the cycle life behavior as compared to electrodes not subjected to ion beam-mixing. The ion beam-mixed silicon electrode had better interfacial strength and fractured with smaller crack spacing as the dose increased. Cross-section TEM images revealed a porous nanostructure within the silicon film and a reacted interlayer around the whole surface of the silicon film. The surface of the electrode, specially the surface oxide, was fractured and absorbed into the interlayer, presumably an SEI layer. While ion beam-mixing did appear to improve the adhesion of the film to the substrate, it is likely that the smaller island dimensions was a significant factor in the long term cyclability of the silicon electrodes.

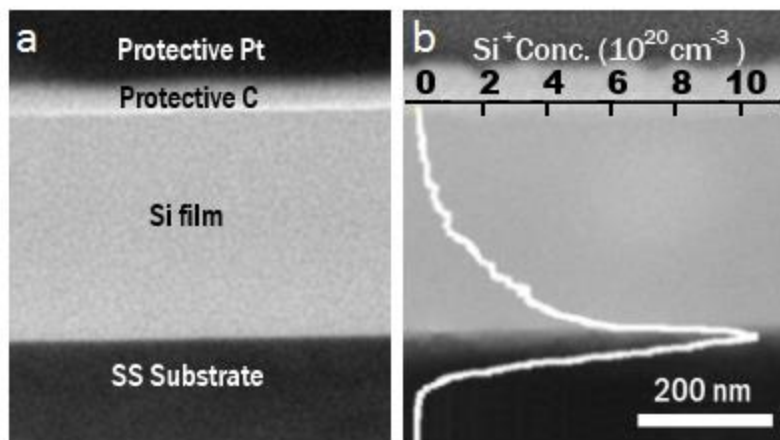


Figure 5-1. XTEM images of virgin Si electrodes prior to electrochemical cycling: a) 350 nm-thick as-deposited electrode and (b) 350 nm-thick ion beam-mixed electrode Si⁺-implanted at 250 keV to a dose of 10¹⁶ cm⁻².

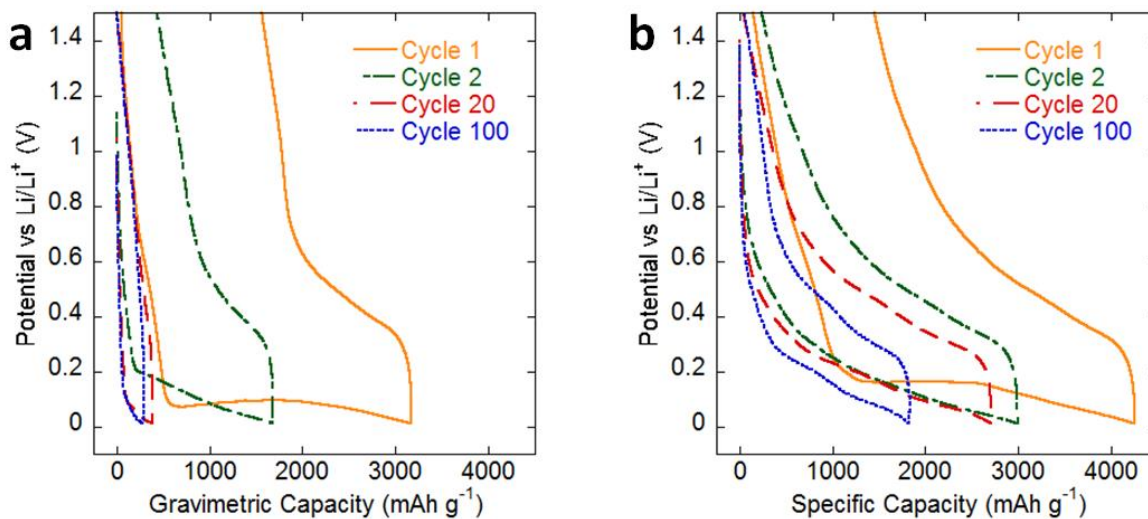


Figure 5-2. Galvanostatic cycling of silicon at 4.2 A g⁻¹ for the (a) as-deposited electrode and (b) 10¹⁶ Si⁺ ion beam-mixed electrode.

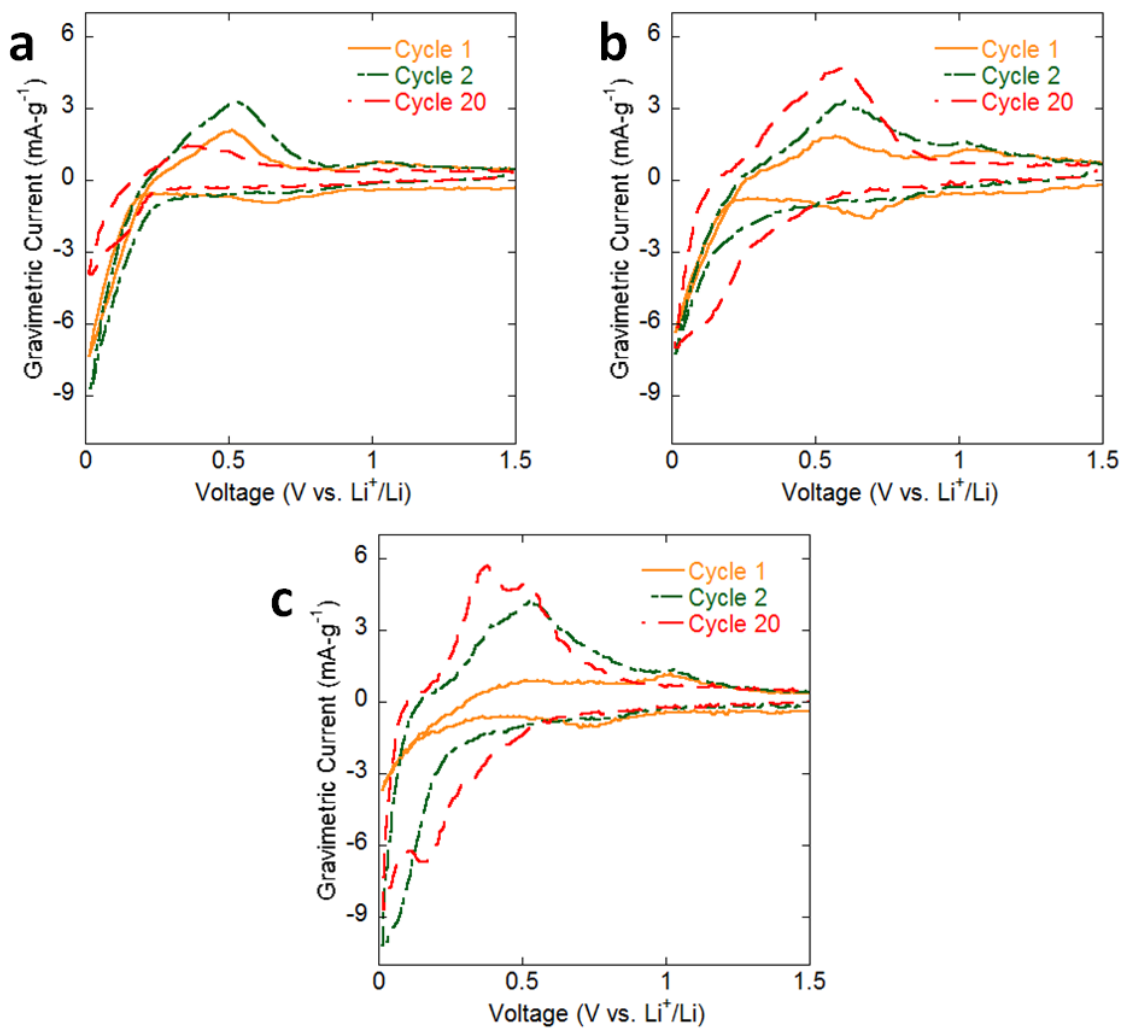


Figure 5-3. Cyclic voltammograms of silicon at a sweep rate of $417 \mu\text{Vs}^{-1}$ for cycles 1, 5, and 20 of the (a) as-deposited electrode, (b) 10^{13} Si^+ , and (c) 10^{16} Si^+ ion beam-mixed electrode.

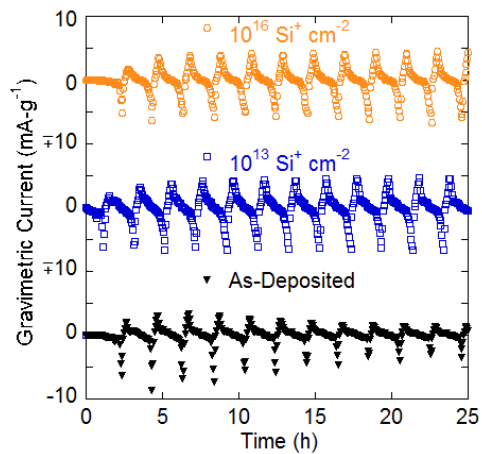


Figure 5-4. Time resolved cyclic voltammograms of silicon at a sweep rate of $417 \mu\text{Vs}^{-1}$ for cycles 1, 5, and 20 of the as-deposited electrode, 10^{13}Si^+ , and 10^{16}Si^+ ion beam-mixed electrode.

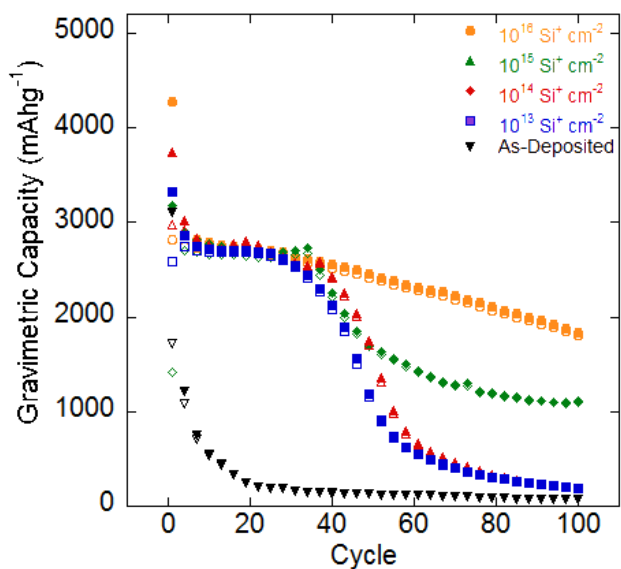


Figure 5-5. Cycle life plot of select as-deposited and implanted silicon electrodes galvanostatically cycled at 4.2A g^{-1} for 100 cycles. The solid and open symbols represent charge and discharge capacities, respectively.

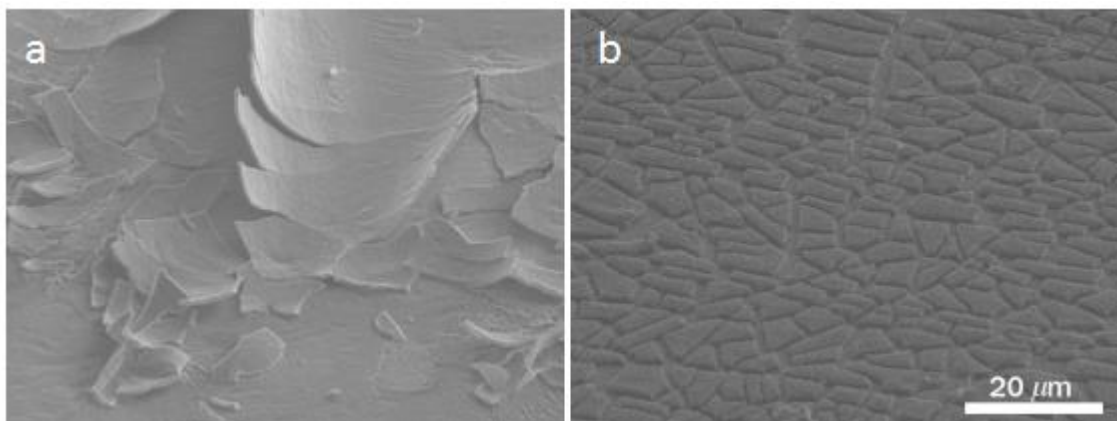


Figure 5-6. Low-magnification SEM images observed at an angle of 52° of Si electrodes after galvanostatic cycling at 4.2 A g^{-1} for 1 cycle: a) an as-deposited electrode showing large-scale delamination of the electrode from the SS current collector and b) an ion beam-mixed electrode Si^+ -implanted to a dose of $1.0 \times 10^{16} \text{ cm}^{-2}$ showing the electrode remains in contact with the SS current collector.

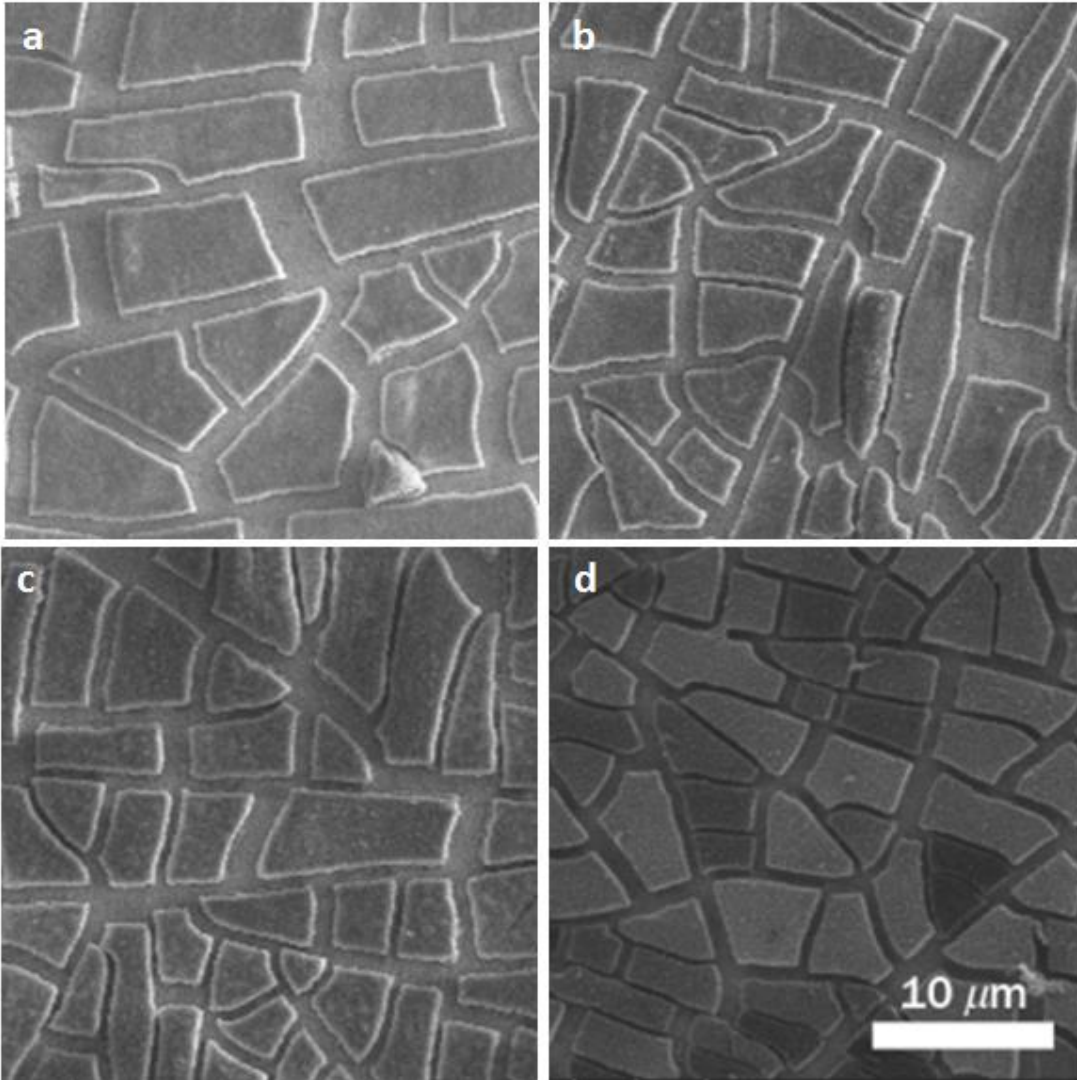


Figure 5-7. Top-down SEM images showing the electrode morphology of ion beam-mixed silicon electrodes after galvanostatic cycling at 4.2 Ag^{-1} for 100 cycles for Si^+ -implantation to doses of a) 10^{13} , b) 10^{14} , c) 10^{15} and d) 10^{16} cm^{-2} .

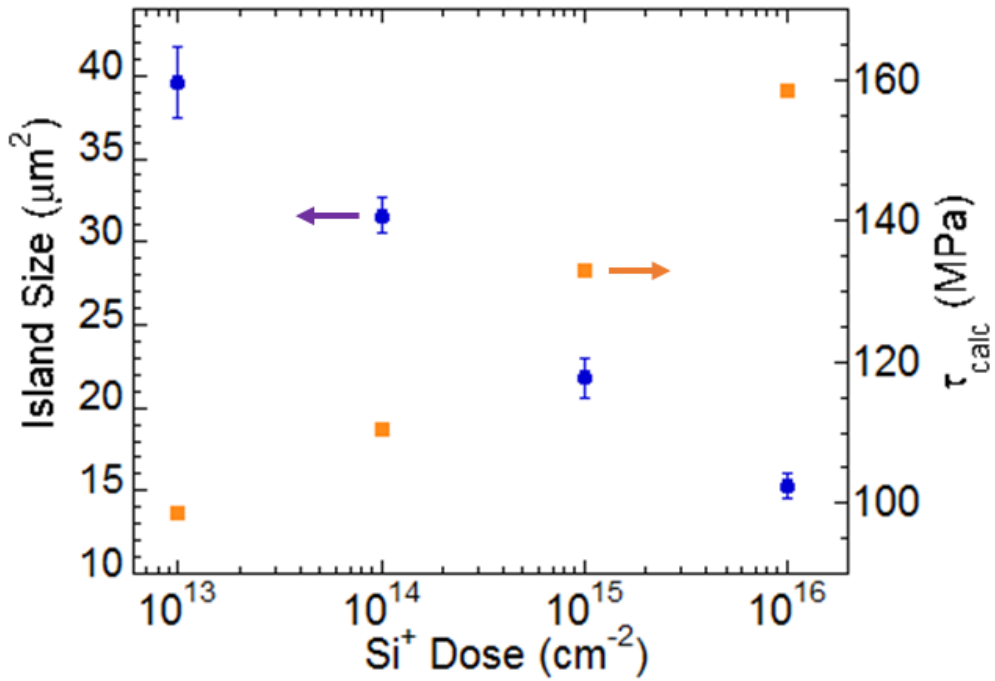


Figure 5-8. The relationships between both the average area of islands and calculated interfacial shear stresses against the Si^+ dose for ion beam-mixed Si electrodes subjected to galvanostatic cycling at 4.2 Ag^{-1} for 100 cycles. The error bars for the island area measurements show significance.

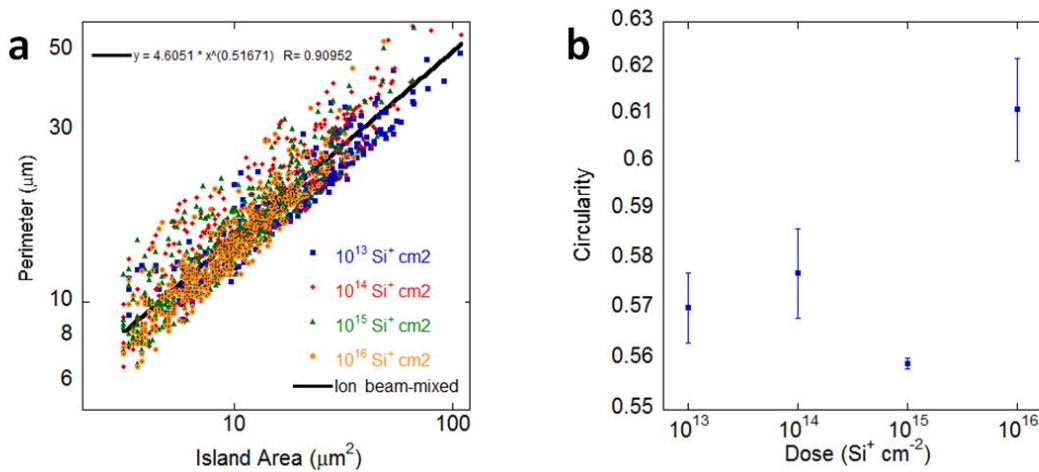


Figure 5-9. Shape descriptors for the fractured silicon islands: (a) fractal dimension and (b) circularity.

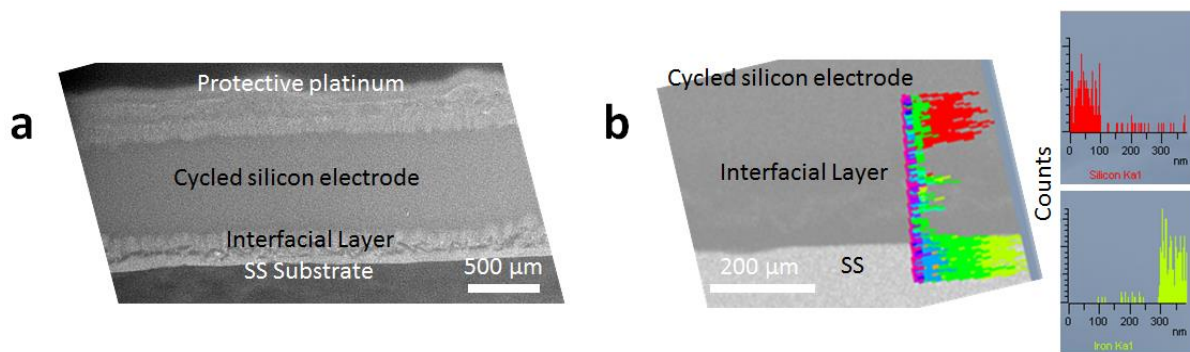


Figure 5-10. Images of a $10^{13} \text{ Si}^+ \text{ cm}^{-2}$ implanted electrode by (a) XTEM and (b) dark field STEM with EDS of silicon (red) and iron (yellow). The samples are oriented with the substrate at the bottom.

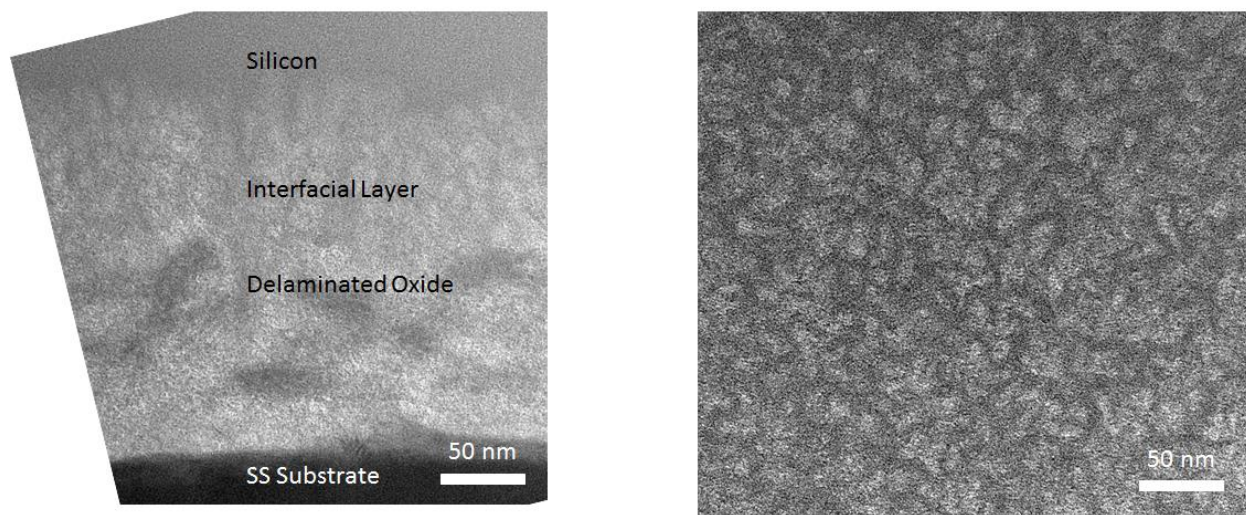


Figure 5-11. XTEM images of the interface between the silicon and substrate for the 10^{13} electrode: (a) bright field image and (b) a high magnification bright field image showing porous structure of the silicon electrode.

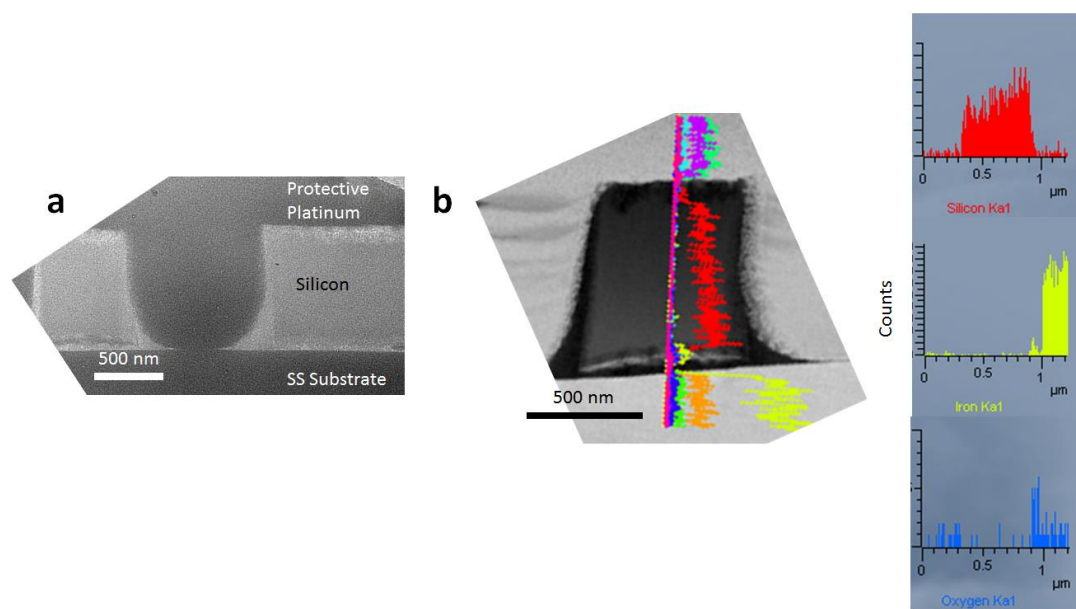


Figure 5-12. Micrographs of a $10^{16} \text{ Si}^+ \text{ cm}^{-2}$ implanted electrode by (a) bright field XTEM and (b) dark field STEM with EDS of silicon (red), oxygen (blue), and iron (yellow). The samples are oriented with the substrate at the bottom.

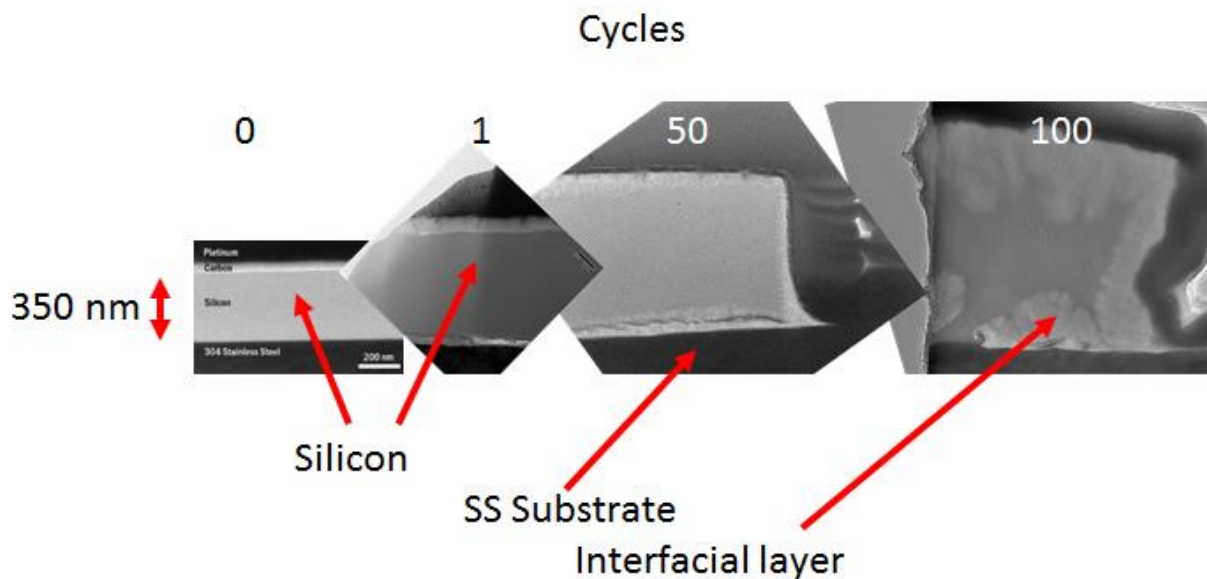


Figure 5-13. Bright field XTEM images of the 10^{16} cm^{-2} implanted silicon electrode at cycles 0, 1, 50, and 100 from left to right. The films are scaled to each other.

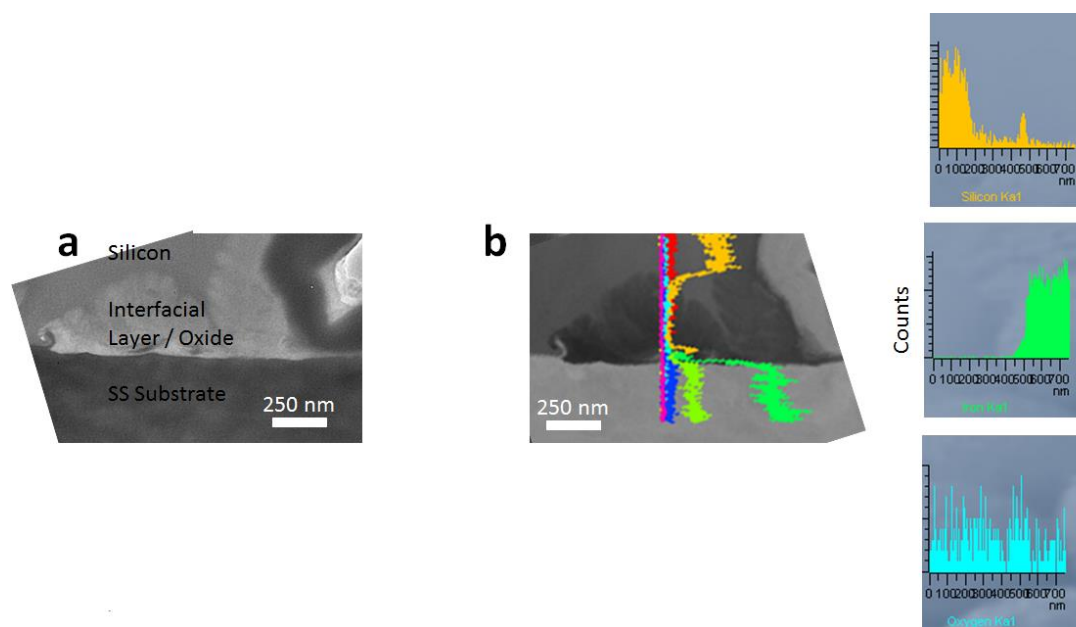


Figure 5-14. Micrographs of a 10^{16} Si^+ cm^{-2} implanted electrode interface after 100 cycles by (a) bright field XTEM and (b) dark field STEM with EDS of silicon (orange), oxygen (aqua), and iron (green). The samples are oriented with the substrate at the bottom.

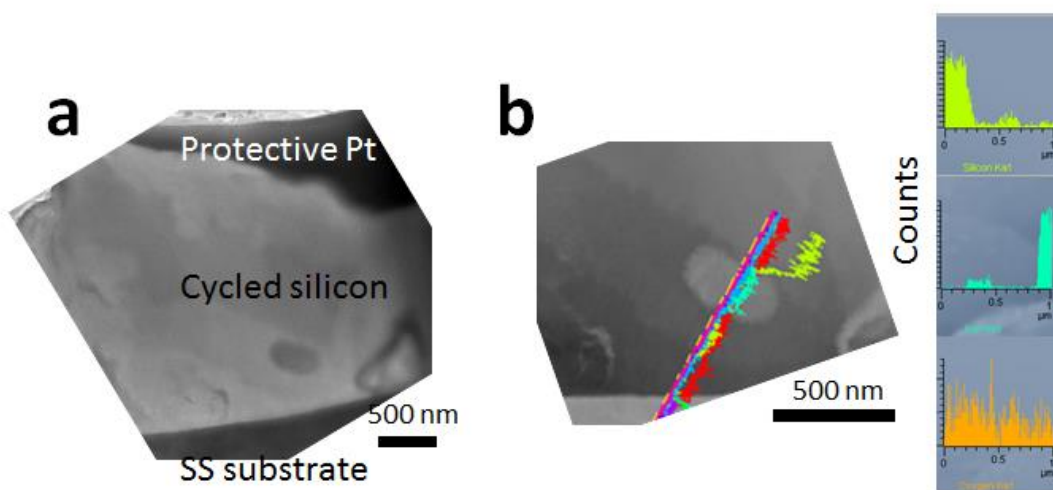


Figure 5-15. Micrographs of a 10^{16} Si^+ cm^{-2} implanted electrode steel particle after 100 cycles by (a) bright field XTEM and (b) dark field STEM with EDS of silicon (yellow), oxygen (orange), and iron (blue-green). The samples are oriented with the substrate at the bottom.

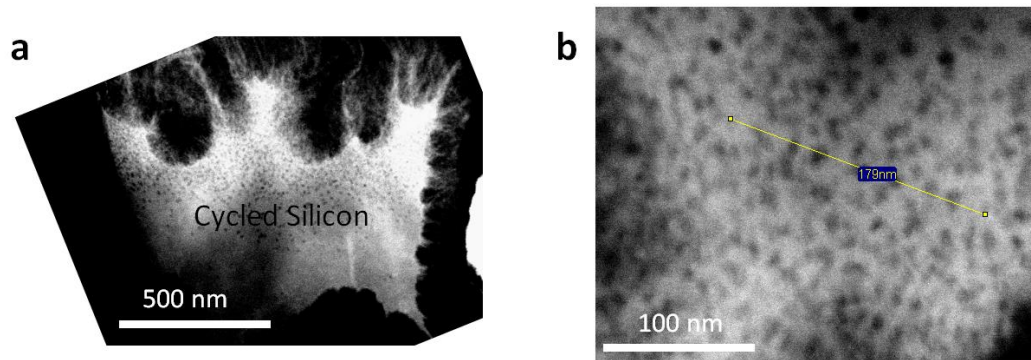


Figure 5-16. Dark field STEM images of a $10^{16} \text{ Si}^+ \text{ cm}^{-2}$ implanted electrode after 100 cycles showing the (a) filament structure and (b) internal nanopores.

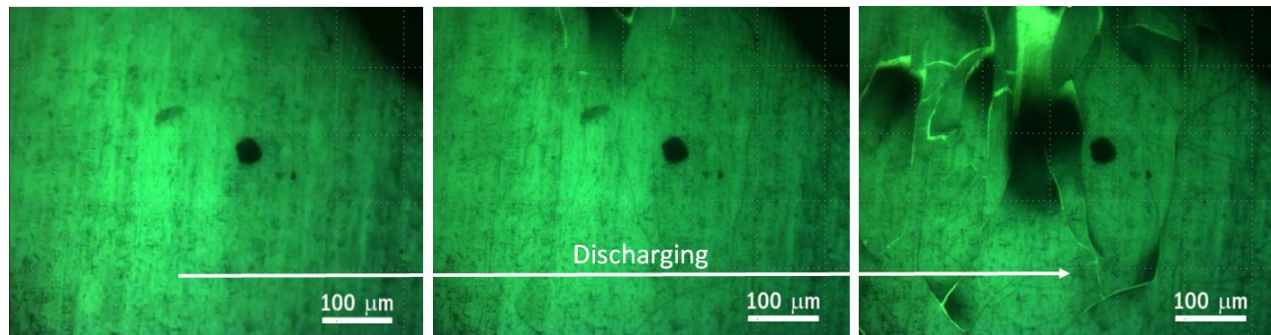


Figure 5-17. OM images of an as-deposited film cracking during discharge. The silicon electrode was cycled at 4.2 A g^{-1} . The images shown are during the first discharge cycle.



Figure 5-18. OM images of an ion beam-mixed film cracking during discharge. The silicon electrode was cycled at 4.2 A g^{-1} . The images shown are during the first discharge cycle.

CHAPTER 6

FRACTURE DUE TO CYCLING RATE AND THICKNESS OF ION BEAM-MIXED SILICON ELECTRODES

One limitation of nanostructured anodes is the limited total capacity of each electrode. It would be convenient to be able to use micrometer or thicker films in devices. Of course electrode fracture and poor kinetics have hindered progress in thick film configurations. In reports where different thicknesses of films are cycled, thicker films always show worse performance and are often cycled at a slower rate [26, 64, 123, 129]. If ion beam-mixing is offered as a possible solution, issues with the accelerating voltage and beam currents may become an issue at higher voltages. According to the SRIM code, an implant of Si^+ through a 1.1 μm amorphous silicon film to promote ion beam-mixing at the interface would need an energy of ~ 1 MeV.

It is also important to understand how the silicon thin film would fracture under different cycling rates. For example, in the previous chapter it was reported that 10^{15} and 10^{16} Si^+ cm^{-2} ion beam-mixed silicon electrodes fractured into islands between 10 – 20 μm^2 . The only other analysis of fractured silicon reports that a 350 nm as-deposited silicon film fractured to islands with sizes within that range but at a cycling rate of C/10 [123]. Both substrates were a type of stainless steel, so the difference in substrate chemistry is expected to have a negligible effect. If the fractured island size could be varied by cycling rate, then a facile route to nanostructured silicon could be achieved through thin film fracture. In combination with ion beam-mixing, the dimensions of the fractured islands could be pushed smaller for better performance.

In this chapter, fracture due to film thickness and cycling rate will be investigated. Thicker films are grown on an as-deposited and ion beam-mixed template as a method to avoid high implant energies. The thicker and thin films will be evaluated based on cycling performances and through fracture analysis.

6.1 Experiments

6.1.1 Sample Preparation

Thin films of 350 nm amorphous silicon were deposited using PECVD, the same method described in Chapters 3 and 5. The as-deposited film acts as a template for further film growth of an additional 350 nm, 700 nm, and 1050 nm, by running the same deposition cycle an additional one or two times. The intended final thickness of the films should therefore be 350, 700, 1050 and 1,400 nm. For the ion beam-mixed electrodes, the 350 nm film is implanted with a 10^{16} Si⁺ cm⁻² dose with an energy of 250 keV at 500 nAcm⁻². The 10^{16} Si⁺ cm⁻² dose was chosen since it resulted in the best performance for the 350 nm silicon electrodes. The implant was performed at room temperature. The 350 nm ion beam-mixed film then acts as a template for the additional growth. Therefore, there is no implantation through the additional film thickness. The as-deposited and ion beam-mixed silicon films both come from the same initial batch and had the additional thickness growth simultaneously. The films were cleaned using water, ethanol, acetone, and isopropyl alcohol before deposition to remove surface contamination. A buffered oxide etch was also considered since the template were exposed to air between the initial PECVD growth and the additional film growth.

6.1.2 Electrochemistry

The as-deposited and implanted films were galvanostatically tested for 100 cycles between the voltage range of 0.01 – 1.5 V. The applied current for the 750 nm and 1,100 nm electrodes were varied between 4.2 Ag⁻¹ and 0.84 Ag⁻¹. The applied current for the 350 nm electrode was varied between 8.4 Ag⁻¹, 4.2 Ag⁻¹, 2.1 Ag⁻¹, 1.4 Ag⁻¹, 0.84 Ag⁻¹, and 0.21 Ag⁻¹ which will be referred to as 2C, C/1, C/2, C/3, C/5, and C/20 respectively. The microstructure of cycled electrodes were observed under SEM to determine the average fractured island size. The 700 nm samples were also tested with cyclic voltammetry with a sweep rate of 417 μVs⁻¹ across a 0.01 – 2.0 V range, in case the impedance pushes the reaction potentials further apart.

The 350 nm samples were tested with cyclic voltammetry with a sweep rate of $83 \mu\text{Vs}^{-1}$ across a 0.01 – 1.5 V, a five hour charge and discharge.

6.2 Results

6.2.1 Sample Characterization

As mentioned in Chapter 3, compressive thermal stresses were manifested within the silicon thin film during cooling from the PECVD temperature of 300 °C to room temperature. The thicker films fared worse than the thin films. This was especially true the films deposited to the expected thickness of 1,400 nm where the entire film fractured before it could even be tested. The ion beam-mixed films fared comparatively better than the as-deposited films at each thickness, but the entire 1,400 nm fractured with an ion beam-mixed template also. That leaves only the 350 nm, 700 nm, and 1,050 nm films to be tested electrochemically.

An XTEM image of the 350, 700 nm, and 1,050 nm as-deposited and implanted thin films are compared in Figure 6-1. An estimate of the ion implantation profile use the TRIM code is also overlaid for comparison. The top and bottom layers of the 700 nm film show no detectable differences except for a thin layer of a light contrast halfway through the thickness. A similar feature can be seen in the 1,050 nm film about one-third of the way through the thickness to the surface. The region of light contrast is expected to the native oxide of silicon. A similar layer can also clearly be seen at the interface between 1,050 nm silicon film and the SS substrate, another oxide. The thickness of the 700 nm film is in fact 700 nm; however, the expected 1,050 nm measures ~1,100 nm. The variation in thickness may be a result of the chamber becoming contaminated over the course of the deposition and accumulation from previous users. The film still serves its purpose for the experiment and will be referred as a 1,100 nm film in the remainder of this chapter.

The native oxide on the silicon was a concern before deposition. The oxide was attempted to be removed via a buffered oxide etch. However, it is likely that the oxide was

stabilizing the buckling by absorbing some of the stress. After etching the previously pristine film buckled and fractured as seen in Chapter 3. This event only happened for the as-deposited films. The ion beam-mixed films remained in pristine condition, which may be explained by the superior adhesion of silicon to the SS substrate. Since a comparison could not be made electrochemically between the etched as-deposited and ion beam-mixed electrodes, the buffered oxide was avoided.

6.2.2 Electrochemistry

The charge and discharge curves of the as-deposited silicon electrodes of thicknesses 350, 700, and 1,100 nm cycled at the 0.84 Ag^{-1} rate are shown in Figure 6-2. The as-deposited silicon electrodes show a reduction in capacity during cycling and large irreversible capacity loss during the first cycle for all thicknesses. For the 350 nm sample, the first cycle discharge (charge) capacity is 2066 (3442) mAhg^{-1} , yielding a charge efficiency of 60.0%. For the 700 nm sample, the first cycle has a discharge (charge) capacity of 2169 (4054) mAhg^{-1} with a charge efficiency of 53.5%. For the 1,100 nm sample, the first cycle discharge (charge) capacity was 1152 (2265) mAhg^{-1} with a charge efficiency of 50.9%. The first charge sequence for all samples drop below and rise to a peak reduction potential for lithiation before dropping again. Similar behavior was seen for the 350 nm film cycles at 4.2 Ag^{-1} . While the 350 nm and 700 nm film react at approximately the same potential of $\sim 0.2 \text{ V vs Li/Li}^+$ during the first charge cycle, the 1,100 nm reacts at $\sim 0.1 \text{ V vs Li/Li}^+$.

The charge and discharge curves of the $10^{16} \text{ Si}^+ \text{ cm}^{-2}$ ion beam-mixed silicon electrodes of thicknesses 350, 700, and 1,100 nm cycled at the 0.84 Ag^{-1} rate are shown in Figure 6-3. The ion beam-mixed silicon electrodes also show a reduction in capacity during cycling and large irreversible capacity loss during the first cycle for all thicknesses. For the 350 nm sample, the first cycle discharge (charge) capacity is 2830 (3750) mAhg^{-1} , yielding a charge efficiency of 75.5%. For the 700 nm sample, the first cycle has a discharge (charge) capacity of 2612 (3433)

mAhg⁻¹ with a charge efficiency of 76.1%. For the 1,100 nm sample, the first cycle discharge (charge) capacity was 1846 (2827) mAhg⁻¹ with a charge efficiency of 65.3%. The ion beam-mixed electrodes also appear to overshoot a peak reduction potential. The reduction potential appears to decrease as the sample thickness increases during the first charge cycle.

The CV profiles of the first, fifth, and twentieth cycles of a 350 nm 10¹⁶ Si⁺ cm⁻² ion beam-mixed silicon electrode is shown in Figure 6-4. The voltage sweep rate is 83 μVs⁻¹. In the first cycle there is a reduction peak at 0.71 V vs Li/Li⁺ and another from 0.01 – 0.23 V vs Li/Li⁺. The reduction peak at 0.74 V vs Li/Li⁺ vanishes as cycling continues. The first cycle shows a dual oxidation peak at 0.38 and 0.51 V vs Li/Li⁺ and another at 1.0 V vs Li/Li⁺. The high voltage oxidation peak remains during the second cycle and vanishes sometime thereafter. During the second cycle, a dual reduction peak forms with a broad high voltage shoulder at 0.012 and 0.17 V vs Li/Li⁺. The low voltage oxidation peak becomes more prominent and shifts slightly to 0.35 V vs Li/Li⁺. By the twentieth cycle the trend continues with the high voltage reduction peak located at 0.18 V and the low voltage oxidation peak located at 0.34 V vs Li/Li⁺. The magnitude of the gravimetric current increases as cycling progresses, with regard to the oxidation processes. Whereas the 10¹³ Si⁺ cm⁻² implanted electrode exhibits peak broadening, the 10¹⁶ Si⁺ cm⁻² implanted electrode clearly forms dual peaks. The peak locations are at 0.016 and 0.16 V vs Li/Li⁺ during lithiation. During delithiation the peaks are at 0.38 and 0.51 V vs Li/Li⁺.

The CV profiles of the first, fifth, and twentieth cycles of a 700 nm 10¹⁶ Si⁺ cm⁻² ion beam-mixed silicon electrode is shown in Figure 6-5. The voltage sweep rate is 417 μVs⁻¹, the same rate tested for the electrodes in Chapter 5. In the first cycle there is a small reduction peak at 0.71 V vs Li/Li⁺ and another from 0.01 – 0.25 V vs Li/Li⁺. The reduction peak at 0.71 V vs Li/Li⁺ vanishes as cycling continues. The first cycle shows a broad oxidation peak between

0.3 and 0.6 V vs Li/Li⁺. During the second cycle, the oxidation peak becomes larger with a shift towards a higher voltage. By the twentieth cycle electrode appears to have completely failed.

Representative cycle life behavior of the 700 nm as-deposited and ion beam-mixed silicon electrodes cycled at 4.2 Ag⁻¹ (C/1) can be seen in Figure 6-6. The cycle life behavior of the 350 nm electrodes were discussed in the previous chapter, while the 1,100 nm electrodes had difficulty starting. The as-deposited silicon electrode fails rapidly, but retains some capacity until cycle twenty. The 10¹⁶ Si⁺ cm⁻² implanted electrode performs significantly better than the as-deposited electrode, but suffers from a continuous decline. These electrodes are also compared with their 350 nm counterparts from Chapter 5. The layered gravimetric capacity compares the expected capacity between electrodes of different thicknesses. If a 350 nm and 700 nm electrode has the exact same gravimetric capacity, then the 700 nm electrode would have double the layered capacity since it is twice the thickness. Despite the lower gravimetric capacity, the 700 nm film can store more total capacity than a 350 nm electrode for approximately thirty to forty cycles. Afterwards the 10¹⁶ Si⁺ cm⁻² ion beam-mixed electrode could store more total capacity at the 4.2 Ag⁻¹ rate. Both as-deposited electrodes completely failed by the thirtieth cycle.

Representative cycle life behavior of the 350, 700, and 1,100 nm as-deposited and ion beam-mixed silicon electrodes cycled at 0.84 Ag⁻¹ (C/5) can be seen in Figure 6-7. The as-deposited silicon electrodes fall to about 1,000 mAhg⁻¹ within the first few cycles, but perform better than their counterpart cycled at a higher rate. The 350 nm and 700 nm as-deposited electrodes retain ~500 mAhg⁻¹ by cycle one hundred. The 10¹⁶ Si⁺ cm⁻² implanted electrodes perform significantly better, with the 350 nm variety performing best. The 350 nm ion beam-mixed electrode begins a sharper decline in capacity around cycle fifty and retains a gravimetric capacity of 1,850 mAhg⁻¹ by cycle one hundred. The 700 nm ion beam-mixed electrode has a lower initial capacity which is fairly stable for about fifteen cycles around 2,250 mAhg⁻¹, before

increasing its failure rate. The 1,100 nm ion beam-mixed electrode has a continual decline in capacity, but never fails at the peak rate of either the 350 nm or 700 nm electrodes. The capacity in the first ten cycles is $\sim 1,250 \text{ mAhg}^{-1}$. When comparing the layered capacities, the 700 nm film actually stores more capacity than the 1,100 nm electrode for about forty cycles, but then fails below the 350 nm electrode by cycle fifty. The 1,100 nm electrode stores the most charge between cycles forty and seventy-five. The 350 nm ion beam-mixed electrode stores the most charge for the remainder of the experiment.

6.2.3 Cycling Induced Fracture

Fractures of the 700 nm as-deposited and ion beam-mixed electrodes cycled at 4.2 Ag^{-1} are shown in Figure 6-8. The island sizes for both electrodes are on the order of $100 \mu\text{m}^2$. The ion beam-mixed electrodes appear smaller, but not to the extent as in the 350 nm films. Both electrodes appear to have cracked through the whole thickness of the film.

Fractured surfaces of a 1,100 nm ion beam-mixed electrode cycled at 0.84 Ag^{-1} are shown in Figure 6-9. The SEM images shows fracture of some islands that are on the order of $1,000 \mu\text{m}^2$. However, through thickness cracking does not appear to be uniform as smaller features can also be seen. While there are regions of a uniform thickness for the small islands, there exists a height distribution between these regions.

The island structure of the 10^{16} cm^{-2} ion beam-mixed electrodes after galvanostatic cycling at 8.4, 2.1, 1.4, 0.84, and 0.21 Ag^{-1} for one hundred cycles was investigated using top-down SEM as shown in Figure 6-10. Based off of measurements of 39 islands, the average island area for the 8.4 Ag^{-1} cycled electrode is $31.0 \pm 8.4 \mu\text{m}^2$. Based off of measurements of 154 islands, the average island area for the 2.1 Ag^{-1} cycled electrode is $9.3 \pm 0.8 \mu\text{m}^2$. Based off of measurements of 226 islands, the average island area for the 1.4 Ag^{-1} cycled electrode is $6.1 \pm 0.4 \mu\text{m}^2$. Based off of measurements of 250 islands, the average island area for the 0.84 Ag^{-1} cycled electrode is $5.4 \pm 0.3 \mu\text{m}^2$. Based off of measurements of 197 islands, the average

island area for the 0.21 Ag^{-1} cycled electrode is $14.8 \pm 1.2 \mu\text{m}^2$. Additionally, the measured perimeters were 24.7 ± 3.6 , 13.9 ± 0.7 , 11.2 ± 0.5 , 10.3 ± 0.4 , and 17.5 ± 0.9 in order of decreasing cycling rate. The circularity shape descriptors were 0.570 ± 0.031 , 0.587 ± 0.017 , 0.593 ± 0.013 , 0.617 ± 0.012 , and 0.591 ± 0.016 in order of decreasing cycling rate.

6.3 Discussion

6.3.1 Effect of Ion Implantation and Thickness on Electrochemical Properties

The best gauge of comparing for the influence of thickness and ion implantation can be seen in Figure 6-7. In all cases the improvement due to ion beam mixing is retained, even through $300 \text{ }^\circ\text{C}$ anneals for up to almost 2 hours, relating to the second and third layer depositions via PECVD. As the electrode increases in thickness, the influence of the ion beam mixing decreases. For instance, the 350 nm ion beam-mixed electrodes are much better improved when compared to the ion beam-mixed 1,100 nm electrode in relation to their respective as-deposited counterparts. The same relationship can be seen in Figure 6-6, although only comparing two thicknesses.

6.3.2 Effect of Ion Implantation and Cycling Rate on Electrochemical Properties

The first comparison can be made through Figure 6-4 and Figure 5-3(c). Both electrodes are ion beam-mixed with a dose of $10^{16} \text{ Si}^+ \text{ cm}^{-2}$ and have a thickness of 350 nm. The electrode in Figure 6-4 has a well-defined reduction and dual oxidation peak in the first cycle which looks more like the second cycle in Figure 5-3(c). Beyond the second cycle, both electrodes share similar characteristics. It is therefore expected that a large impedance, likely diffusion related, limits the reduction of the silicon at higher sweep rates, but the partial reduction that does occur assists the electrochemical reaction in future cycles.

The opposite characteristics can be seen in Figure 6-5. Here a 700 nm electrode fails to fully lithiate before eventually failing. Outside of film fracture, this partial lithiation due to high impedances contributes to the lower capacity in thicker electrodes or electrodes cycled at higher

rates. This type of behavior is commonly expressed when charging and discharging electrodes at different rates [19, 43, 98, 130]. Ion beam-mixed electrodes retain improvements over as-deposited electrodes when cycled after different rates.

6.3.3 Effect of Ion Implantation and Thickness on Electrode Failure

In Figure 6-7, the silicon electrode fractures through the thickness of the 700 nm films. These electrodes and the electrodes in Chapter 5 were cycled at the same rate; however, the 700 nm 10^{16} Si⁺ cm⁻² ion beam-mixed electrodes have a fractured island area of the order of 100 μm^2 , about an order of magnitude larger than the similarly implanted 350 nm films. This result does not follow the relationship proposed in Equation 2-15. At the 4.2 Ag⁻¹ cycling rate, the 700 nm electrodes generally had capacities $\sim 1,000$ mAhg⁻¹ less than their 350 nm counterparts. The partial lithiation state likely has a different yield stress or lower fracture toughness which can complicate the comparison. This result neither supports nor disproves Equation 2-15.

The fracture characteristics in Figure 6-9 are likely due to the native oxide of the template layer silicon. Preferential cracking along the interface could expel the top 700 nm of the film and allowing the now exposed 350 nm film to cycle as normal. This type of fracture could explain why the ion beam-mixed 1,100 nm electrode did not have a sharp decay rate when compared to the 700 nm electrode in Figure 6-7(b). The 304 SS surface was shown to be rough in Chapter 3. The terraced structure in Figure 6-9(b) could be influenced by the underlying substrate. Otherwise the structure would suggest that silicon fractured by lateral cracks either above or below the native oxide layer.

6.3.4 Effect of Cycling Rate on Electrode Failure

The 350 nm 10^{16} Si⁺ cm⁻² ion beam-mixed electrodes generally displayed a smaller crack spacing as the cycling rate decreased, except at the slowest cycling rate studied, shown in Figure 6-10. When the island areas and perimeters are plotted against cycling rate in Figure

6-11, the fractured island area can be estimated through a linear relationship when excluding the 0.21 Ag⁻¹ (C/20) result. The fractured area increased by ~3.43 μm²(Ag⁻¹)⁻¹ while the perimeter increases by ~1.83 μm(Ag⁻¹)⁻¹. Further investigation is required to understand the differences between the fracture at a C/5 and C/20 rate. A minimum island size is expected somewhere between those two rates. Figure 6-12 compares the island areas and perimeters of all the measured islands of the rate-tested electrodes. The best-fit fractal dimensions are 0.528, 0.532, 0.537, 0.539, and 0.556 for the 8.4, 2.1, 1.4, 0.84, and 0.21 Ag⁻¹ rates, respectively. The similar dimension indicates little difference in the shape of fracture between the electrodes.

6.4 Concluding Remarks

Ion beam-mixing has been shown to retain improvements in electrochemical performance despite altering electrode thickness or cycling rate. A thin native oxide layer on the template surface likely altered the fracture characteristics of the 1,100 nm thick silicon electrodes. Special care should be taken to remove the oxide; however, buckling fracture of the as-deposited electrode upon the native oxide removal complicated the comparisons. A relationship between the fractured island area and cycling rate has been established between 0.84 and 8.4 Ag⁻¹ for the 350 nm ion beam-mixed electrode. Controlling the lithium insertion or extraction rates could be used to create a nano-patterned surface.

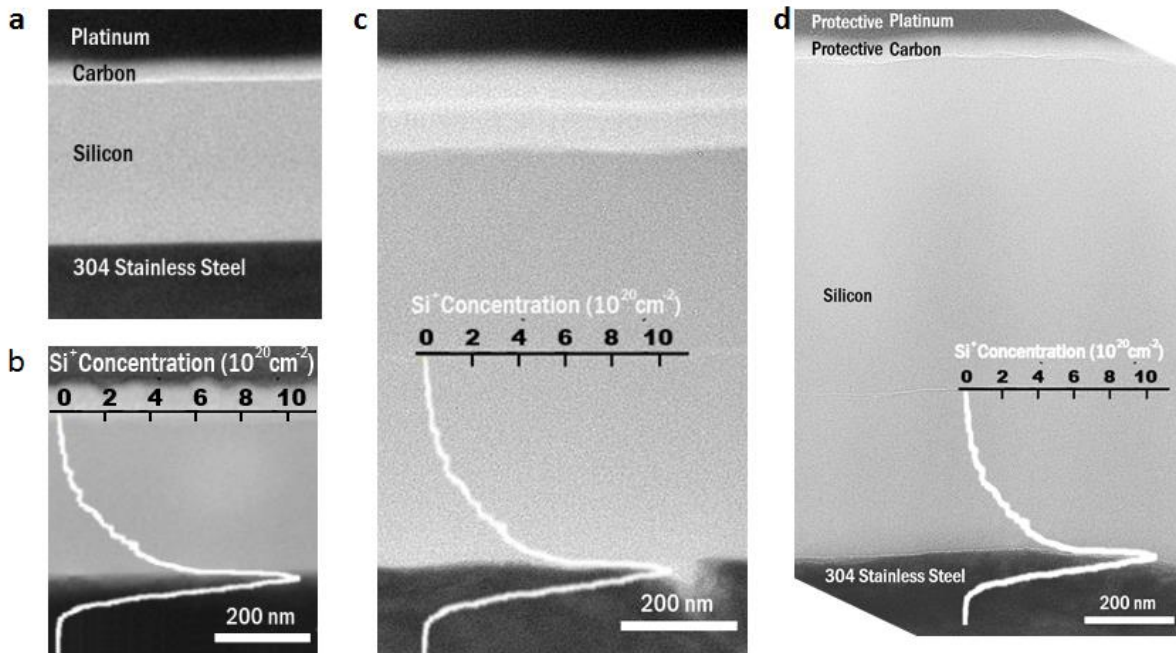


Figure 6-1. XTEM images of virgin Si electrodes prior to electrochemical cycling for various thicknesses: a) 350 nm-thick as-deposited electrode, (b) 350 nm-thick ion beam-mixed electrode Si⁺-implanted at 250 keV to a dose of 10¹⁶ cm⁻², (c) 700 nm-thick ion beam-mixed electrode, and (d) 1,100 nm-thick ion beam-mixed electrode, where only the lower 350 nm of the film is implanted, as shown by a TRIM overlay.

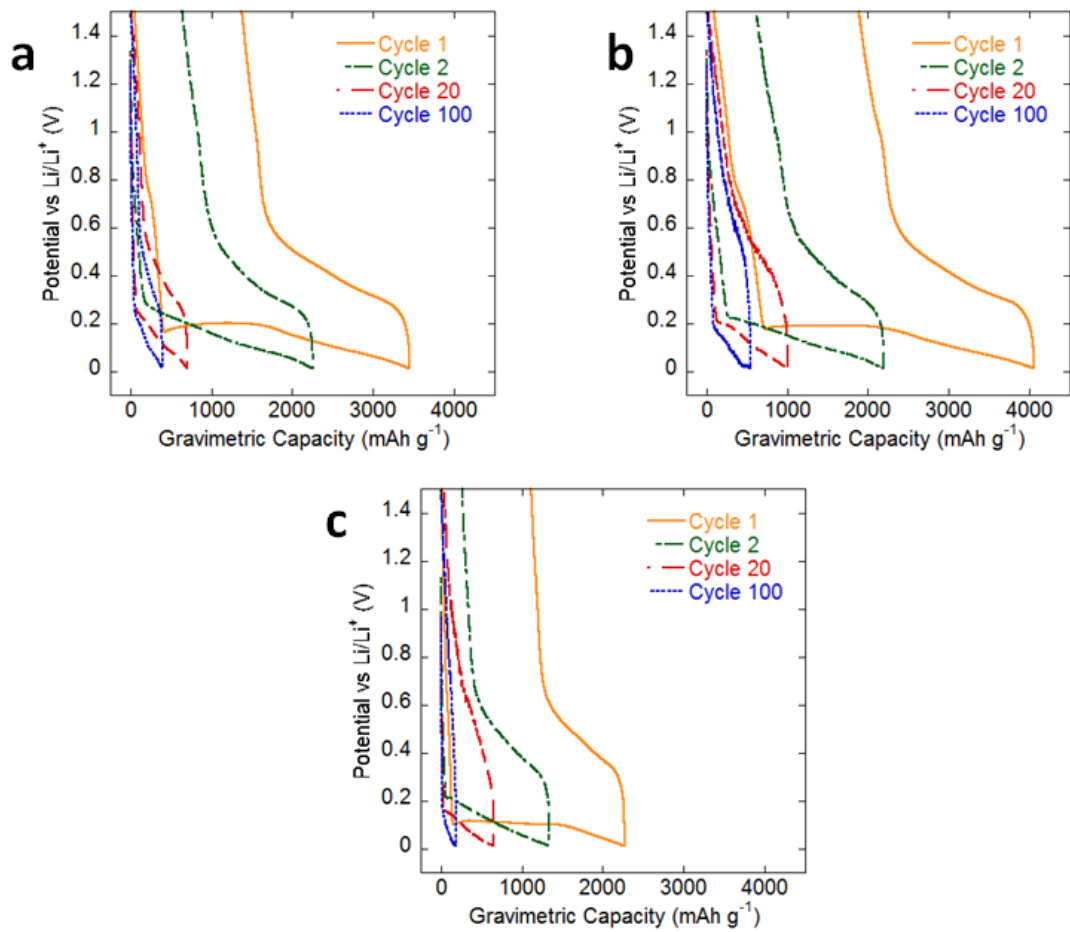


Figure 6-2. Galvanostatic cycling at 0.84 Ag⁻¹ for the as-deposited silicon electrode for various thicknesses: (a) 350 nm, (b) 700 nm, and (c) 1,100 nm.

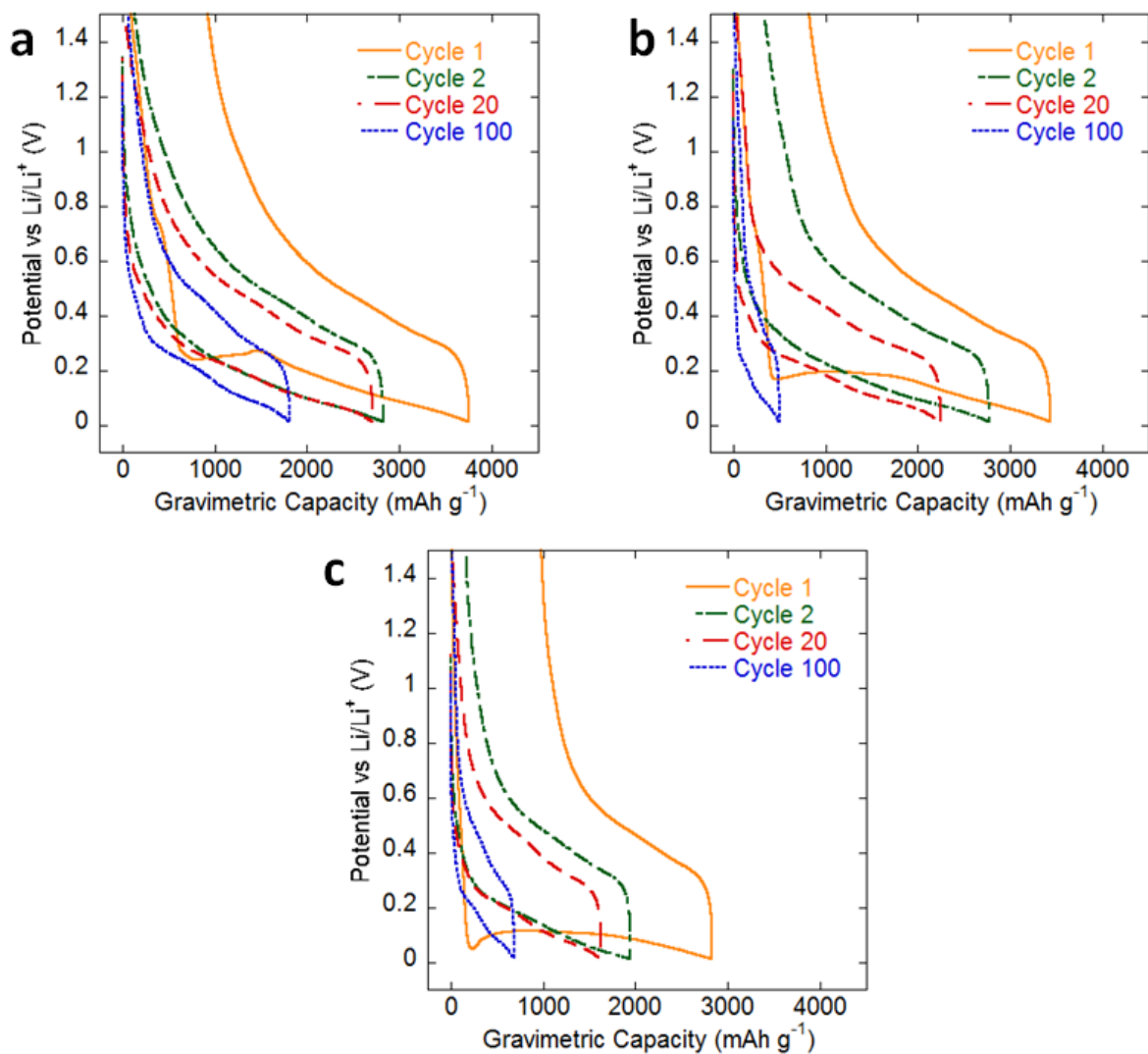


Figure 6-3. Galvanostatic cycling at 0.84 Ag^{-1} for the $10^{16} \text{ Si}^+ \text{ cm}^{-2}$ ion beam-mixed silicon electrode for various thicknesses: (a) 350 nm, (b) 700 nm, and (c) 1,100 nm.

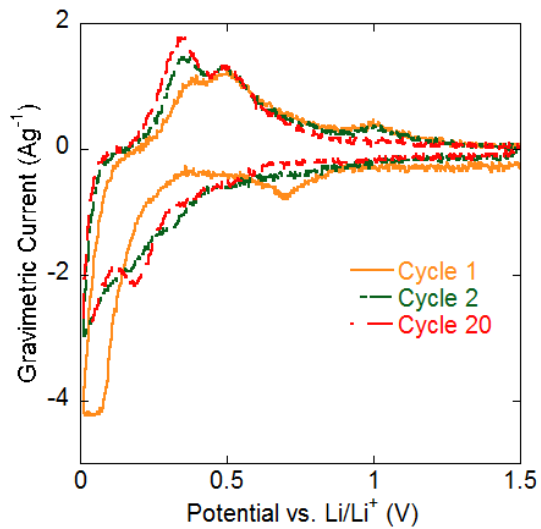


Figure 6-4. Cyclic voltammogram at a sweep rate of $83 \mu\text{Vs}^{-1}$ for cycles 1, 5, and 20 of the $350 \text{ nm } 10^{16} \text{ cm}^{-2} \text{ Si}^+$ ion beam-mixed silicon electrode.

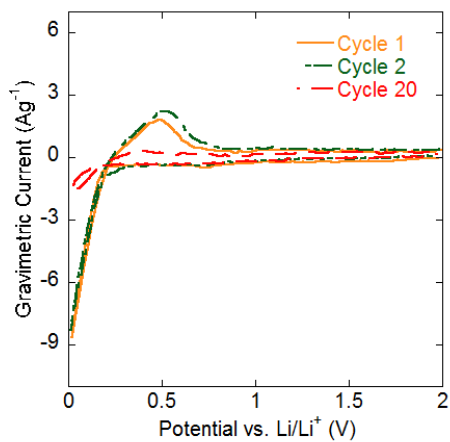


Figure 6-5. Cyclic voltammogram at a sweep rate of $417 \mu\text{Vs}^{-1}$ for cycles 1, 5, and 20 of the $700 \text{ nm } 10^{16} \text{ Si}^+ \text{ cm}^{-2}$ ion beam-mixed silicon electrode.

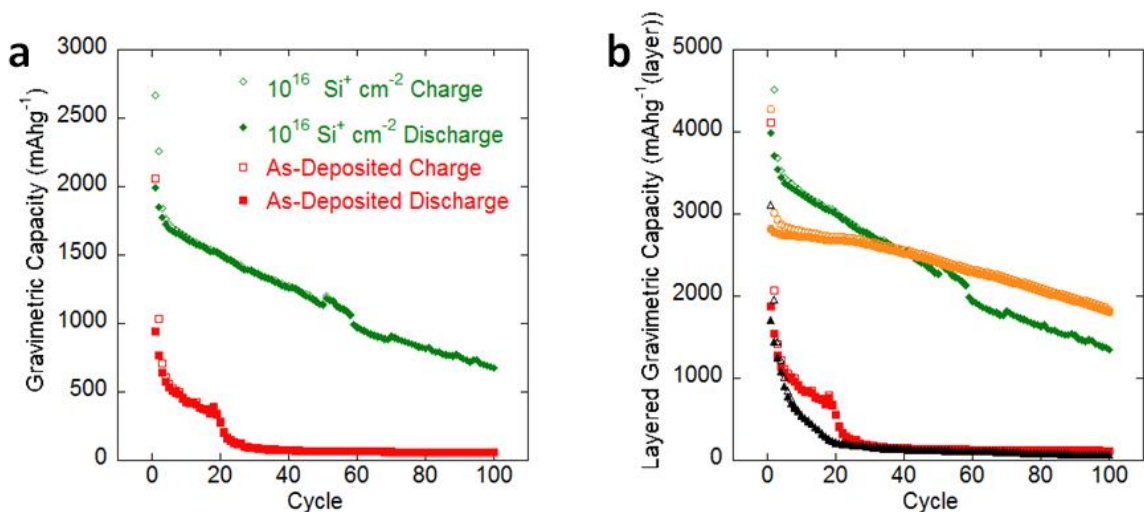


Figure 6-6. Typical cycle life data for the 700 nm silicon electrodes cycled at 4.2 A g⁻¹. The as-deposited and ion beam-mixed electrodes Si⁺-implanted to dose of 10¹⁶ cm⁻² are compared in (a) while the layered capacity is shown in (b). The layered capacity is shown with the addition of the respective 350 nm electrodes from Chapter 5.

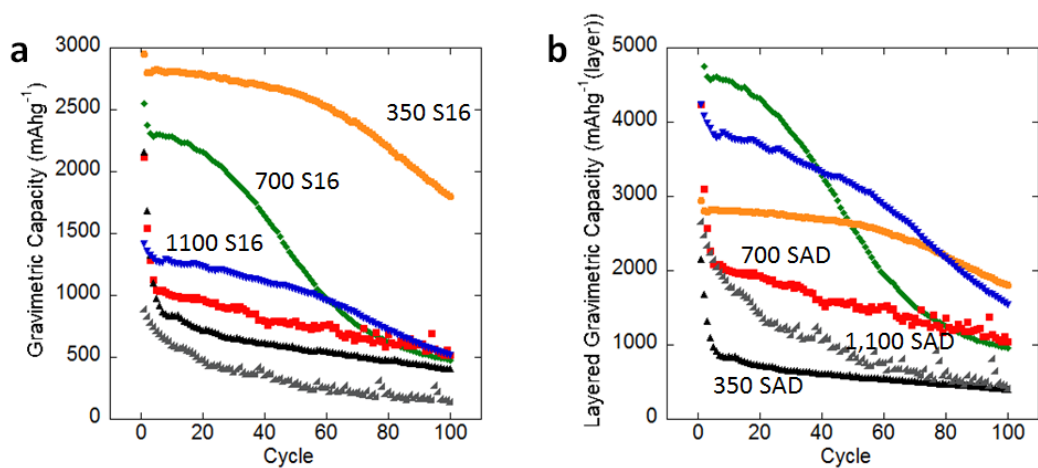


Figure 6-7. Typical cycle life data for silicon electrodes of various thicknesses galvanostatically cycled at 0.84 A g⁻¹. In (a), the 350, 700, and 1,100 nm as-deposited and ion beam-mixed silicon electrodes are compared. S16 refers to the implanted dose, and SAD refers to the as-deposited electrode. The layered capacities of the same electrodes are shown in (b).

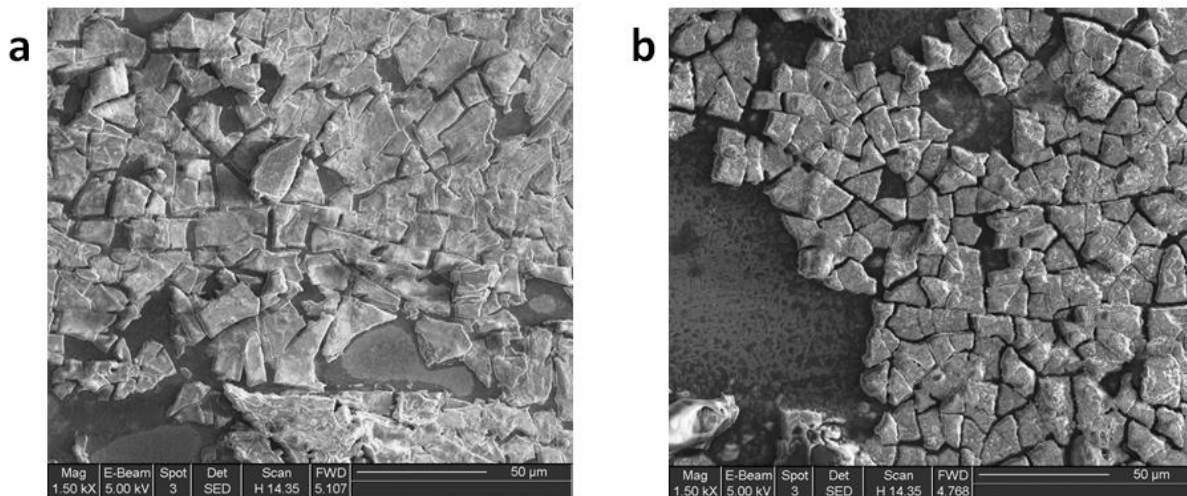


Figure 6-8. Top-down SEM images showing the electrode morphology of the 700 nm thick silicon electrode after 100 cycles at 0.84 A g^{-1} : (a) as-deposited and (b) ion beam-mixed electrodes.

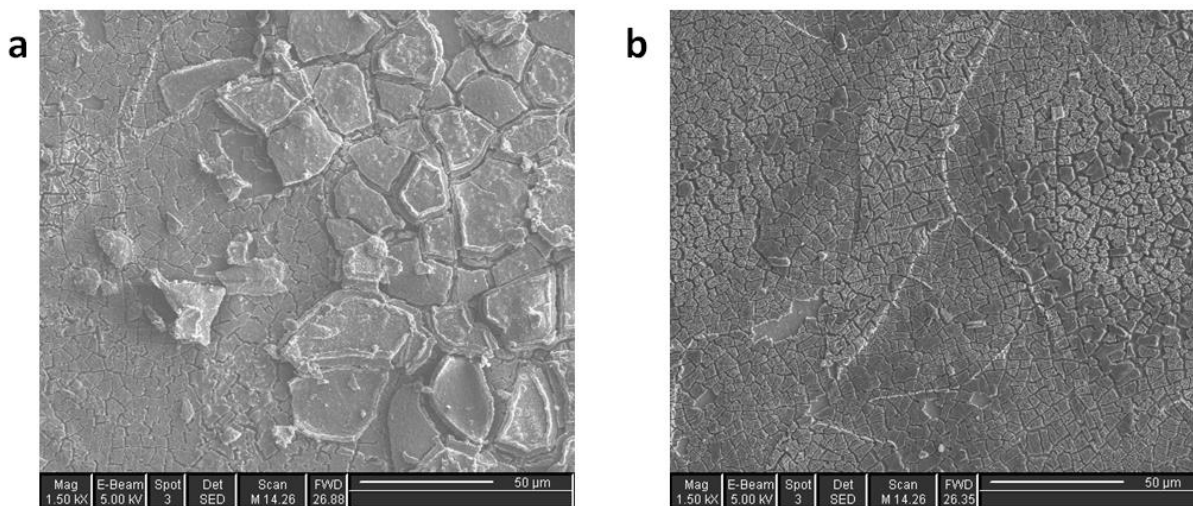


Figure 6-9. Top-down SEM images showing different crack morphologies of the 1,100 nm thick silicon electrode galvanostatically cycled at 0.84 A g^{-1} for 100 cycles: (a) large through-thickness islands and (b) terraced structure.

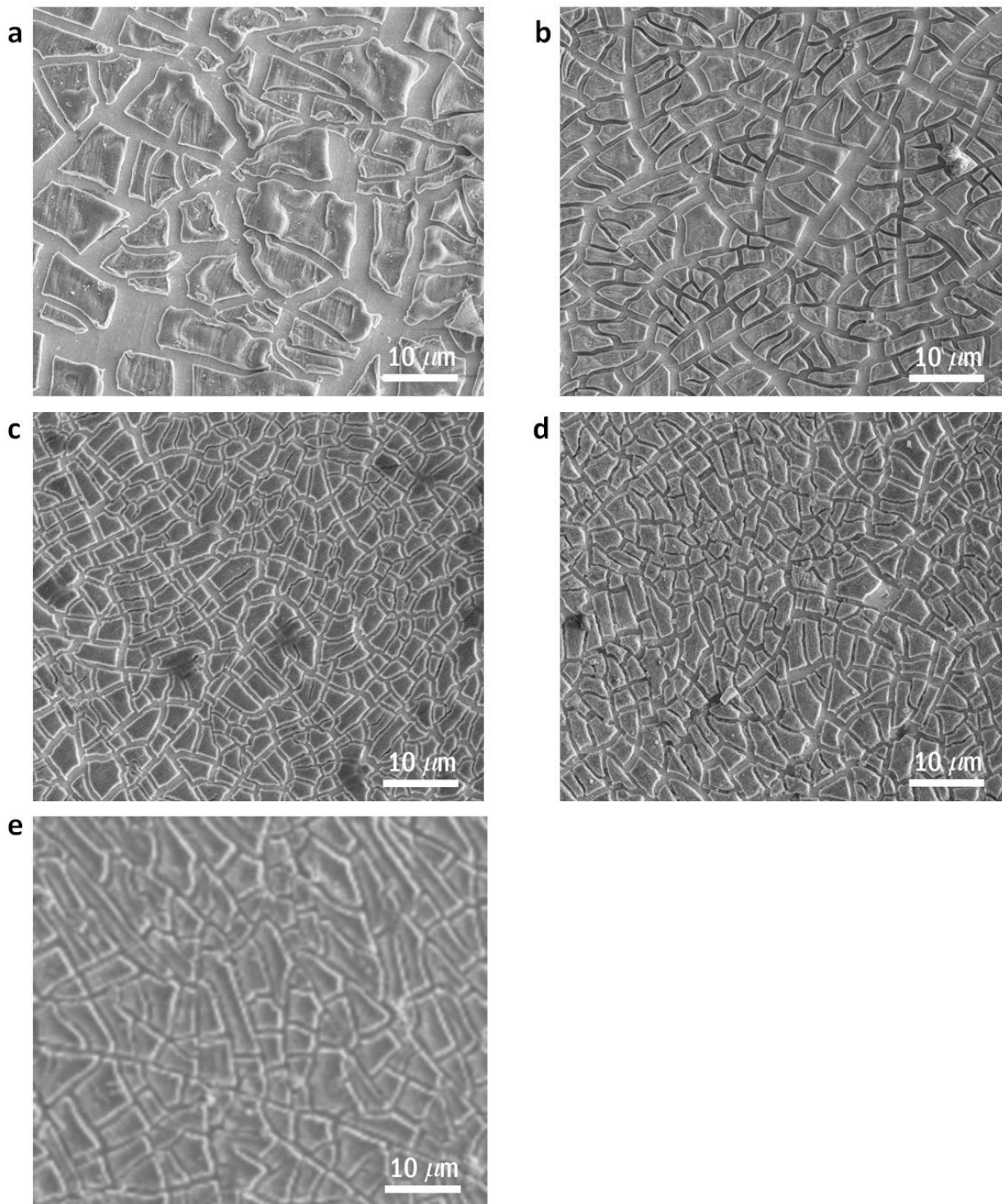


Figure 6-10. Top-down SEM images showing the electrode morphology of ion beam-mixed Si electrodes after various galvanostatic cycling at rates for 100 cycles: (a) 8.4 A g^{-1} , (b) 2.1 A g^{-1} , (c) 1.4 A g^{-1} , (d) 0.84 A g^{-1} and (e) 0.21 A g^{-1} .

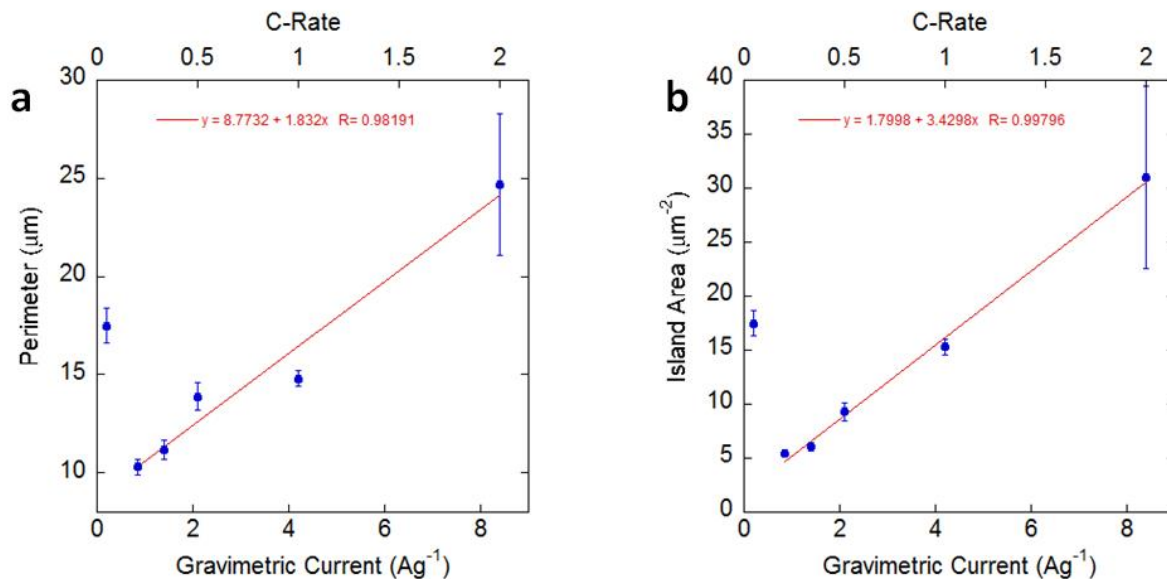


Figure 6-11. Comparison of geometric properties in relation to the cycling rate for the 350 nm ion beam-mixed silicon electrodes: (a) perimeter and (b) island area.

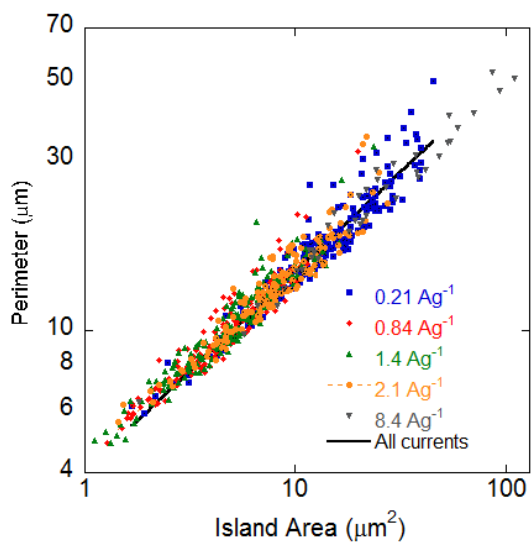


Figure 6-12. The fractal dimension of the 350 nm ion beam-mixed electrodes cycled at different rates.

CHAPTER 7

ION BEAM-MIXING

Physically, a large number of factors can be an influential contributing factor for ion beam-mixing including interface chemistry, stress, contaminants, morphology, implant species, implant energy, and implant dose. Ebe et al. found that the adhesion of copper onto polyamide films was better at 0.5 keV Ar ions rather than 5 or 10 keV ion due to carbonization of the polyamide at higher energies [131]. Wolf et al. found that a broad mixing region is required to improve adhesion if there is little to no chemical affinity between the ion and host [132]. Martin et al. found that ion implantation with oxygen or oxygen plus argon improved adhesion by two orders of magnitude, while argon alone did not alter the adhesion of gold onto glass [133]. Due to the large number of factors involved with ion beam-mixing, models relating implant characteristics to adhesion improvements have not been reliably developed.

In this study, the ions were chosen to match the film chemistry in order to isolate improvements due to the ion beam-mixing. The implanted species are also compatible with the substrate materials. Germanium has solubility in nickel up to about 10 at% [134]. Silicon is also soluble in steel as 304 SS already contains an appreciable amount of silicon in relation to the implant doses and concentrations. Therefore it is expected that the silicon and germanium implants may improve adhesion through a similar mechanism. This chapter will evaluate a possible physical mixing method to relate implant dose and interfacial shear stress.

Figure 7-1 shows the TRIM implant profile of Ge⁺ ions into a Ni₈₀Fe₂₀ under the conditions used in this study. The implant profile is defined by,

$$C(x) = \frac{MQ_i}{\Delta R_p \sqrt{2\pi}} e^{-\frac{(x-R_p)^2}{2\Delta R_p^2}} \quad (7-1)$$

where $C(x)$ is the concentration of a species as a function of depth, M is a scalar factor that defines the diffusion source ($M \leq 2$, which defines a finite diffusion source at a surface), Q_i is the

implant dose, R_p is the projected range of the implant, and ΔR_p is the straggle or deviation of the implant. Figure 7-1 also shows a Gaussian fit defined by Equation 7-1 where R_p is redefined and set to 0 Å (offset by film thickness, 1400 Å). The straggle, ΔR_p , is 247 Å into the substrate with $M = 0.74$. It is suspected that damage, amorphization, or concentration threshold exists where a feature below the threshold does not contribute to improved adhesion. This critical concentration, C_{cr} , is related to a critical length, L_{cr} , as follows

$$L_{cr} = R_p \sqrt{2 \ln \left(\frac{\sqrt{2\pi} C_{cr} \Delta R_p}{M Q_i} \right)} \quad (7-2)$$

At this point, the interface which was once defined by a delta has now increased in thickness through mixing with a characteristic length defined in Equation 7-2. It is speculated that the interfacial shear stress increases proportionally to the characteristic length,

$$\tau_i = \begin{cases} \tau_{ad} & L_{cr} < L_{ad} \\ \tau_{ad} + B L_{cr} & L_{ad} \leq L_{cr} \leq L_s \\ \tau_s & L_s < L_{cr} \end{cases} \quad (7-3)$$

where τ_{ad} and L_{ad} define the initial interfacial shear stress and characteristic length, τ_s and L_s define the yield stress of the substrate and the appropriate characteristic length, and B is a scaling factor with units of Nm^{-3} . A physical interpretation for B has not been determined. This mixing mechanism should only relate to a “dilute” implant, where a species is soluble and the dose is low enough to avoid precipitation. At a sufficiently high dose, the film will be best adhered by minimum of the shear properties of the either the film or the substrate. One will yield before the other no matter how well an interface is mixed. Combining Equations 2-15, 7-2, and 7-3 yields

$$A(Q_i) = \frac{\pi}{4} \left(\frac{2h\sigma_y}{\tau_{ad} + B \Delta R_p \sqrt{2 \ln \left(\frac{\sqrt{2\pi} C_{cr} \Delta R_p}{M Q_i} \right)}} \right)^2 \quad (7-4)$$

where the fracture island area is defined as a function of implant dose. Since τ_{ad} , τ_s , C_{cr} , and B are unknown, the model is difficult to fit due to being non-linear. If the critical concentration is $8.0 \times 10^{17} \text{ Ge}^+ \text{ cm}^{-3}$ and $\tau_{ad} = 15 \text{ MPa}$, then $B = 5.01 \times 10^{14} \text{ Nm}^{-3}$. A critical concentration of $8.0 \times 10^{17} \text{ Ge}^+ \text{ cm}^{-3}$ is within the range of the TRIM estimate for the size of the damaged layer seen in Figure 4-2. The interfacial shear stress value of $\tau_{ad} = 15 \text{ MPa}$ was chosen since Equation 2-15 predicts an island size $\sim 220 \mu\text{m}^2$, which is roughly the island size observed, although features were poorly defined. The model is fit to the island size data in Figure 7-2 with an $R^2 = 0.991$.

The model proposed above which relates island area to implant dose is also applied to the silicon electrodes of Chapter 5. Figure 7-3 shows the implant profile of 250 keV Si⁺ into a Si film with the silicon-steel interface at 3500 Å. The straggle, ΔR_p , is 346 Å into the substrate with $M = 1.04$. Since the island sizes for the as-deposited film were closer to $160 \mu\text{m}^2$ on average, τ_{ad} was chosen to be 50 MPa, using Equation 2-15. It makes sense for the interfacial shear stress of the silicon and 304 SS interface to be larger than germanium and Ni₈₀Fe₂₀ interface since the as-deposited germanium could be peeled off by tape while the silicon was strongly adhered. The friction strength between gold and mica was also measured to be 40 MPa [135], which may be an appropriate estimate for the shear strength between the 304 SS oxide layer and underlying metal. For Si, the C_{cr} is chosen to be $10^{17} \text{ Si}^+ \text{ cm}^{-2}$ which leads to $B = 6.22 \times 10^{14} \text{ Nm}^{-3}$. The model is superimposed in Figure 7-4, where the island size data against implant dose is also presented. The fit has an R^2 value of 0.932.

While the models may explain a significant amount of the variance in the data, the actual mechanism towards improved interfacial strength may depend on the oxide layer that is found at the surface of both metallic substrates. A simple experiment to etch the substrate or ablate the surface in-situ to provide better cleaning would isolate the effect of the surface oxide. A contaminant monolayer may also interfere with the ion beam-mixing results. The as-deposited

layer would be expected to have poor adhesion to the contaminant monolayer, but ion bombardment may easily break up the layer and open the possibility for improved adhesion to the underlying substrate.

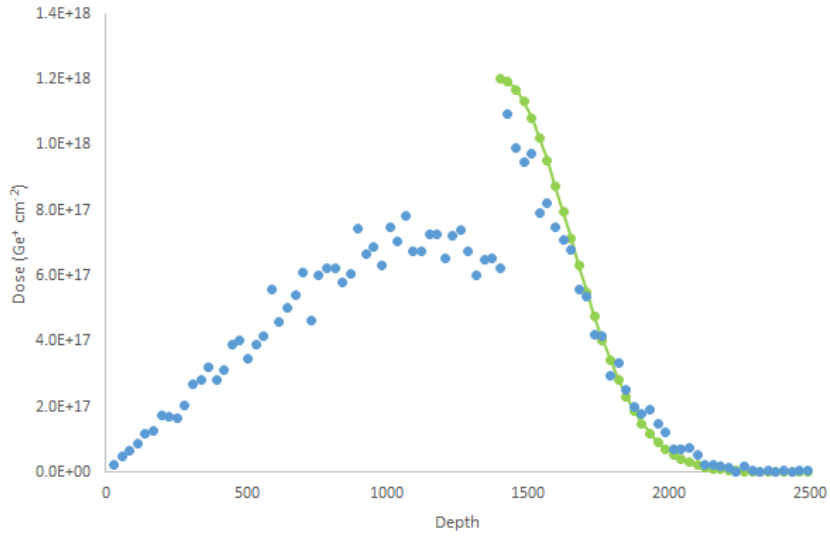


Figure 7-1. Gaussian fit to the TRIM implant prediction for Ge⁺ into germanium with a nickel-iron interface at 1400 Å.

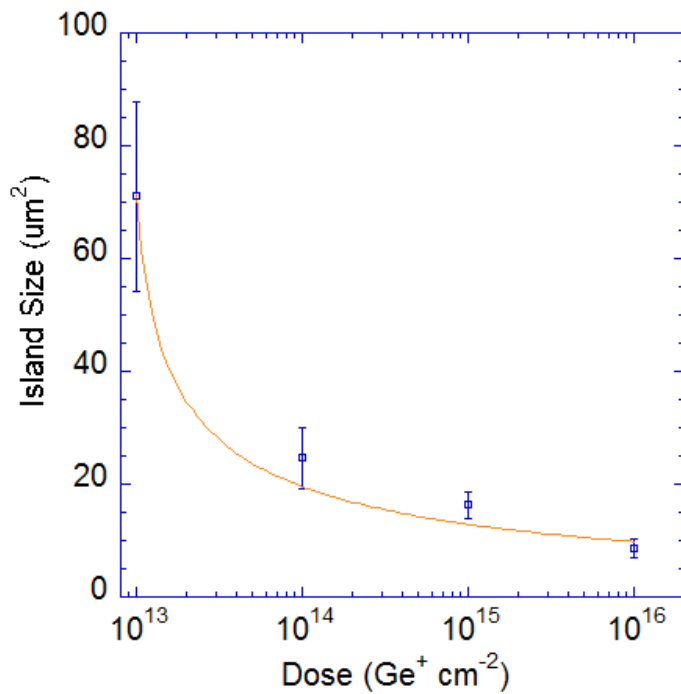


Figure 7-2. Fit of Equation 7-4 to the island size data of the cycled 140 nm germanium electrodes from Chapter 4.

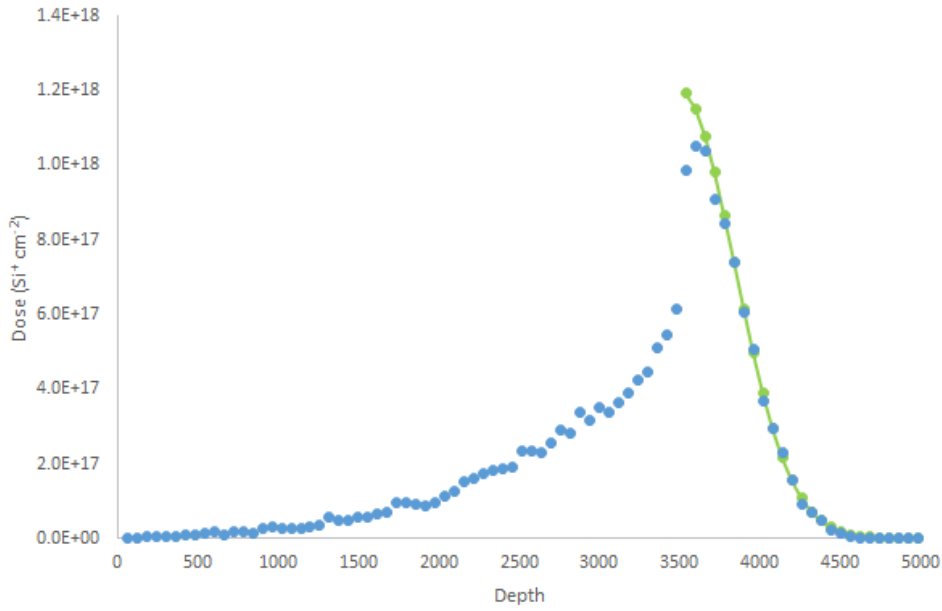


Figure 7-3. Gaussian fit to the TRIM implant prediction for Si⁺ into silicon with a stainless steel interface at 3500 Å.

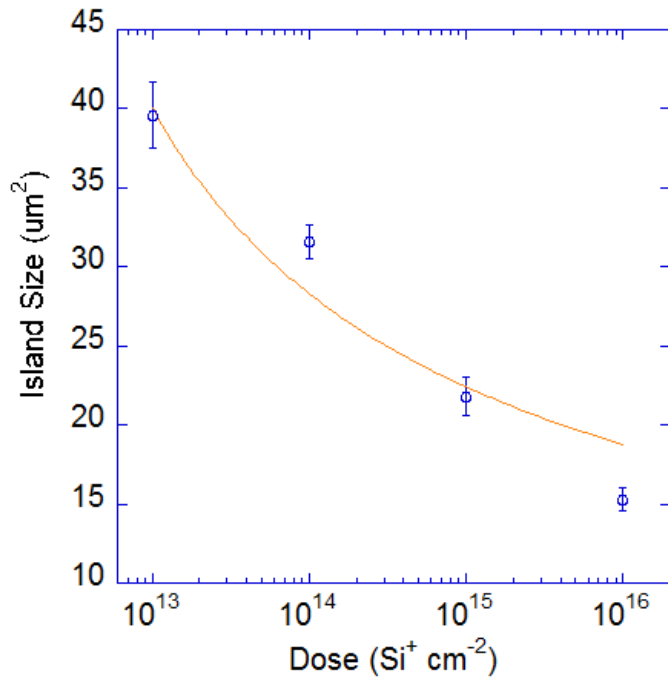


Figure 7-4. Fit of Equation 7-4 to the island size data of the cycled 350 nm silicon electrodes from Chapter 5.

CHAPTER 8 CONCLUSIONS

8.1 Summary

In conclusion, the electrochemical performances of ion beam-mixed germanium and silicon electrodes for Li ion batteries were investigated. It was shown that increasing ion dose resulted in a concomitant improvement in cycle life behavior as compared to electrodes not subjected to ion beam mixing. Unlike the as-deposited electrodes which experienced large-scale delamination from the current collector after only one electrochemical cycle, ion beam-mixed electrodes did not experience any large-scale delamination for silicon and resisted large scale delamination in germanium.

Furthermore, by quantifying the microstructure of the ion beam-mixed electrodes after electrochemical cycling, it was proposed that increasing ion dose resulted in increased interfacial strength of the electrode to the current collector. Both germanium and silicon electrodes showed smaller feature features as the implanted ion dose increased. The improvement in electrochemical performance with increasing ion dose was therefore attributed to improved interfacial strength between the electrode and current collector. The mechanistic relationship between interfacial strength and cyclability is unclear for both germanium and silicon electrodes. In the germanium electrodes, the $10^{15} \text{ Ge}^+ \text{ cm}^{-2}$ implanted dose samples resulted in fifty cycles without any capacity fade while the $10^{14} \text{ Ge}^+ \text{ cm}^{-2}$ implanted dose samples died after a few cycles. Such a result implies that achieving an island size below $20 \mu\text{m}^2$ may be most important in determine cyclability. The same $20 \mu\text{m}^2$ island area may also apply for the silicon electrode, since only the $10^{16} \text{ Si}^+ \text{ cm}^{-2}$ implant dose resulted in features that small.

Cross-sectional analysis of the fractured silicon electrodes show the presence of an interlayer, thought to be an SEI layer, at the silicon / substrate interface along with a

delaminated surface oxide. It is therefore expected that the benefit of ion beam-mixing only influences the initial fracture. Fractured islands of differing dimensions were also tailored by changing the cycling rate, where in general, a slow cycling rate results in a smaller crack feature.

8.2 Future Work

Portions of this experiment can be repeated with deposition on metal coated ultra-thin silicon wafer, or other appropriate substrates. A more appropriate substrate would eliminate confounding variables such as the impact of the compressive thermal stress or the impact of ion bombardment not related to ion beam mixing (relaxed versus unrelaxed structures) at the interface through wafer bending experiments. It is unclear whether the histories of those effects are retained during the lithiation process. If the entirety of the increased performance is related to ion beam-mixing, then the smooth electrochemically polished surface will provide more information to the nature of film fracture. In the experiment the substrate was rough and therefore had numerous nucleation sites of high stress intensity factors.

Studies of the interlayer between the silicon and the substrate could lead to a better understanding of the fatigue related failure modes in silicon electrodes. The impact of adding vinylene carbonate or other sacrificial additives to the electrolyte in order to influence the SEI layer growth is unclear. The nature and sequence of formation of the interlayer may provide reasons as to why the $10^{13} - 10^{15} \text{ Si}^+ \text{ cm}^{-2}$ ion beam-mixed silicon electrodes fared similarly in terms of electrochemical performance, but had obvious differences in fracture dimensions. If the fracture dimensions are not so critical, why would the $10^{16} \text{ Si}^+ \text{ cm}^{-2}$ silicon electrode provide such an improved performance? If the fracture dimensions are critical to the point where only those structures with island sizes below $20 \mu\text{m}^2$ would lead to improved cycling performance, then an as-deposited film patterned to appropriate dimensions should replicate the impact of ion beam mixing.

Another ion beam-mixing experiment would be to investigate the chemical role of the implant species. An implant with a noble gas could act as a baseline comparison to silicon if all of the improvement in adhesion was due to physical mixing. Other implant species such as phosphorus or arsenic could simultaneously improve the electrical conductivity of silicon and provide improved adhesion. The dose rate could also be varied to provide differing amounts of damage at the same dose to determine if an amorphization or damage threshold exists to overcome.

The fracture dependence on cycling rate also has an unresolved issue with the silicon cycled at the 0.21 Ag^{-1} (C/20) rate. At a certain strain rate, plastic flow could be the preferred deformation mechanism, and the film might fracture at the higher voltage rather than lower voltage oxidation sequence, if there is a difference between the fracture potentials. Rate-dependent fracture mechanisms are important to consider when comparing electrode failure between different studies.

Other experiments could look at the impact of surface preparation to avoid the use of ion beam mixing. If a monolayer of contaminants is the principle cause for the poor adhesion of the as-deposited layers, then improved cleaning techniques could push the cyclability past several of the ion beam-mixed samples. Likewise, the surface oxide, which delaminated in all of the tested silicon electrodes, appeared to be a weak link. Removal of the oxide layer may improve performance beyond that of the ion mixed results of this study.

APPENDIX A

THREE DIMENSION RECONSTRUCTION AND ANALYSIS OF SERIALY SECTIONED SOLID OXIDE FUEL CELL ELECTRODES

The microstructure and morphology of solid oxide fuel cell (SOFC) electrodes directly impact the electrochemical polarization. Several metrics to analyze the morphology of an electrode are phase fraction, porosity, surface area, triple phase boundary (TPB) length, tortuosity, and connectivity.

A.1 FIB/SEM Serial Sectioning

In preparing a serially sectioned sample using a FIB, the first step is to deposit a thin layer of carbon on the surface as a sacrificial layer to protect the specimen surface during alignment processes. Once the site of interest and beams are properly aligned, a needle is inserted near the site of interest emitting an organometallic platinum gas. The precursor gas interacts with ion beam and deposits a platinum layer on the specimen surface [60]. The protective platinum layer is a protective mask for the subsequent milling and dictates the sampling area. The next step is to make a “C-trench” around three edges of the platinum layer shown in Figure A-1. The slicing direction will proceed from the C-trench edge with two connected vertices to the opposite end of the platinum layer. The viewing direction with the SEM is the same as the slicing direction. The other two edges in the C-trench are prepared to accommodate deposition from the milling process which could otherwise end up blocking the view of the cross sectioned microstructure. For samples with a 10 μm by 10 μm sampling area, the C-trench dimensions were typically 2 μm by 12 μm on either side of the sampling area and 12 μm by 10 μm for the viewing trench, as shown in Figure A-1. The milling times and depth are sample dependant.

The serial sectioning process is automated by FEI's Auto Slice and View software. The dimension of the milling mask, number of slices, and image collection time are all inputs to the software. The milling mask is typically placed over the sampling area, dictated by the platinum

layer, with an addition 0.5 μm on every edge to account for the possibility of sample drift. The distance between slices can be determined by the pattern dimension in the milling direction divided by the number of slices. Images are collected through either secondary electrons or backscattered electrons, depending on what gives superior phase contrast. Contrast for the pore phase can also be improved by epoxy infiltration which can be seen in Figure A-2. With epoxy filled pores, each cross-sectional slice will be planar. Epoxy infiltration was carried out using a Struers EpoVac system.

A.2 Phase Identification and Measurements

The alignment and labeling processes were performed using Amira Resolve RT 4.0, along with most microstructural measurements. It is convenient to save the workspace as a network. The images collected from the Auto Slice and View software were directly imported after determining the in-plane pixel dimensions from the image scale bar shown in Figure A-3. The width of the cross section, parallel to the platinum cap, is properly measured by the scale bar. The vertical dimension of the cross section, parallel to the depth of the mill, is multiplied by ~ 1.3 to account for the 38° viewing angle since the ion and electron beams are offset by 52° in the FEI Strata DB 235. The width will be referred to as the x-dimension, the vertical dimension of the cross section as the y-dimension, and the slicing direction as the z-dimension. These dimensions are input after importing the source images to the Amira software. The input window can be seen in Figure A-4.

A.2.1 Alignment and Shearing

After importing the images with proper dimensions into the Amira software, the images need to be aligned if there was any sample drift. If every image is already perfectly aligned, this step may be skipped. To align the images, right click the green module signifying your data and select compute then AlignSlices, shown in Figure A-5. In the properties window select the edit action. Each image will now be shown in the viewing window. Scroll through the images to find

a common feature, usually on the back wall of a C-trench, shown in Figure A-6. Once a common feature is found, select the landmark alignment mode in the toolbar above the viewing window. Also select the edit landmarks arrow. In each image, select the common feature four times so that a red and yellow marker fills in over the feature. Once completed, select align all slices in the toolbar. Afterwards select the resample action in the properties window to create a new green module with properly aligned images.

Although the images are now aligned to each other, the images are not orthogonal to the viewing direction. To create an orthogonal view, right click the green module with the aligned images and select Shear, shown in Figure A-7. In the properties window for Shear, input -38 as the angle and click apply. If done properly, the interface between the platinum layer and region of interest should be at the same y-position in every slice. This can be easily viewed by right clicking the new green module and selecting OrthoSlice.

The final step in the image preparation is to crop out the excess of the images. The crop function is shown in Figure A-8. Align the OrthoSlice images so that the XY plane is viewed orthogonally. In the properties of the green Sheared module, select the crop option. In the first slice, align the top edge just below the interface between the platinum and sample cross section. The sides are also set within the width of the platinum layer. In the last slice, the bottom edge of the crop box is defined. If the images are not perfectly aligned such that the platinum drifts into the uncropped region, or milling artifacts appear on any of the edges then adjust the crop dimensions accordingly. Click OK when finished.

A.2.2 Labeling

Phase identification occurs during the labeling process, usually based on the relative grayscale values in the SEM image. To create a label field, right click the cropped green module and select Labeling and LabelField, shown in Figure A-9. The labeling process is carried out when viewing the images in the XY-plane. Initially two phases are initialized for the

sample, Exterior and Inside. The Exterior phase is often renamed to the pore phase, while the Inside phase for the active electrode material. In composite electrodes, an additional third phase is added for the ion conducting electrolyte. Additional phases to account for closed pores, milling artifacts, or different materials such as platinum could also be added by selecting New Materials button. The materials can be renamed by right clicking the material names. Once the correct number of materials are set-up, labeling can progress through a variety of techniques.

The simplest technique is to utilize the Magic Wand. With a clear distinction between phases, adjusting the grayscale slide to only capture the material of interest allows a convenient labeling process when the region is selected on the image. A red mask appears over the image signifying what proportion of the image would be selected by the wand. Fill interior is generally selected to remove imaging artifacts where a single pixel may vary substantially from its neighbors. Once selected with the wand, the material needs to be added to the appropriate material by highlighting the material and pressing “+” or selecting the plus shaped button. If there is no systematic variation in contrast between images or within images, selecting All Slices and Same material only could appropriately label the chosen phase in every image slice with one click.

Other imaging techniques are Blow, Lasso, Brush, and Pick Region. The Blow tool grows from an initial starting point along a contrast gradient while the user holds down and moves the mouse. The Blow tool is useful if there is a contrast gradient within a phase, but the phase boundaries are distinct to the eye but not appropriate for the Magic Wand. The Lasso tool allows the user to freehand an outline of a particle, which will be automatically filled in for phase selection when completed. The brush allows the user to color in phase by freehand in order to label. Both freehand labeling techniques can be assisted by locking previously labeled phases to mask off and protect those regions. Pick Region selects a single phase in either one

or every image which can then be easily removed or combined with another phase for imaging or measurement purposes. When performing those operations with Pick Region, it is useful to resample the LabelField beforehand to create additional copies.

A.2.3 Surface Generation

A three dimension depiction of the labeled areas can be generated by right clicking the green labeled module and selecting Compute and SurfaceGen. In the SurfaceGen properties window, there are three options for smoothing: constrained smoothing, unconstrained smoothing, and none. Constrained smoothing smooths the surface while preserving voxel details from the LabelField by only performing a limited amount of smoothing at interfaces. Unconstrained smoothing creates a smooth representation, although often with loss of detail at interfaces. Selecting none simply creates a three dimensional representation where the voxels retain a prism shape, and no details at the interfaces are lost. Clicking apply results in a green surface module. The three dimensional surface can be viewed by right clicking the new green surface module and selecting Display and SurfaceView.

A.2.4 Measurements Module

The phase fraction, porosity, tortuosity, and surface area can all be conveniently measured in Amira 4.0. The first three can be accessed by right clicking the green labeled module and selecting Measure and MaterialStatistics. The phase fraction represents the normalized volume of each phase. The measurement can be performed over the whole volume or on a slice by slice basis to view composition gradients. To perform the measurement over the whole sampled volume, select Materials and Apply in the MaterialStatistics properties window. Selecting Show in the newly created green module's properties window displays the total number of voxels, volume of each phase, and center of mass in each direction. Following the same process but selecting Volume per slice instead of Materials allows the user to extract

information on composition gradients. Porosity is measured the same way since it is just the phase fraction of the pore phase.

The tortuosity of a given phase can be determined by extracting the Polar moment of inertia from the MaterialStatistics module. Through this technique, the tortuosity is measured from the center of mass of the phase rather than through each possible parallel path. The cumulative distance between the center of mass positions for each phase in each slice is compared to the distance between the starting and ending position.

A.2.5 Nodal Connectivity and Measured Average Z-Orientation

The nodal connectivity of the reconstructed electrode microstructure was measured through a skeletonization process of the dataset. The skeletonization process proceeds by iteratively thinning a given phase so that a complex microstructure is reduced to nodes (vertices) and pathways. A more detailed review of the skeletonization process can be found in other works by Gostovic et al [Gostovic 2011 [136]]. The skeleton output lists a series of pathway segments, often segmented by slice. The pathway endpoints represent node positions while node separation distance represents \mathbf{L}_k , the topological length. The number of pathway endpoints at a certain node position results in the local nodal connectivity, \mathbf{k}_i , such that,

$$\langle \mathbf{k} \rangle = \frac{\sum_i \mathbf{k}_i}{N_k} \quad (\text{A-1})$$

where $\langle \mathbf{k} \rangle$ is the average nodal connectivity, and N_k is the total number of nodes. The average topological length is defined by,

$$\langle \mathbf{L}_k \rangle = \frac{\sum_j \mathbf{L}_{k,j}}{N_k} \quad (\text{A-2})$$

where $\mathbf{L}_{k,j}$ is the individual length between nodes.

The measured average z-orientation (MAZO) represents the direction in space that nodal connections orient towards the electrolyte interface. This angle is formed between the

line segment of the starting node to the ending node and the line segment between the starting node and the projection of the starting node in the ending node's slice. Therefore an angle of zero degrees would be orthogonal to the electrolyte surface while an angle of ninety degrees would be in the plane parallel to the electrolyte surface. The methods in this sections were utilized to characterize the structure of LCM and LSCF composite SOFC cathodes [136].

A.2.6 Active Connectivity and TPB Measurements

The connectivity of an electrode represents the fraction that efficiently contributes to the electrochemical process. If an electron conducting material in contact with the interconnect and an ion conducting material in contact with the electrolyte form a TPB then system has a connectivity of one. The connectivity would be zero if the ion conducting material was isolated within the electron conducting material since the ion conducting material would be effectively inactive. The pore and electron conducting phases would be active if they were connected to the electrode surface. The ion conducting phase would be active if it was connected to the electrolyte.

In the two dimensional cross-sectioned images, the TPB are represented by points where the three phases meet. Since there is no knowledge of the TPB morphology between slices, the TPB length is estimated by the least squares distance between the points on each slice. If the following slice no longer contains information about the specific TPB, then an in-plane measurement is determined from the previous slice to close the TPB loop. The TPB density is determined using both the TPB length measurement and connectivity information so that,

$$\rho_{\text{TPB}} = \frac{L_{\text{TPB,active}}}{V_{\text{total}}} \left(1 + \frac{L_{\text{TPB,unknown}}}{L_{\text{TPB,active}} + L_{\text{TPB,inactive}}} \right) \quad (\text{A-3})$$

where ρ_{TPB} is the TPB density, V_{total} is the total composite electrode and pore volume the reconstruction, and L_{TPB} is the TPB length for active, inactive, and unknown interfaces.

Unknown TPBs are those that are begin or terminate at the sidewall of the reconstruction volume, so its true connectivity is uncertain. The methods in this section were utilized to determine the structure-property relationships for AFLs of various compositions [137, 138].

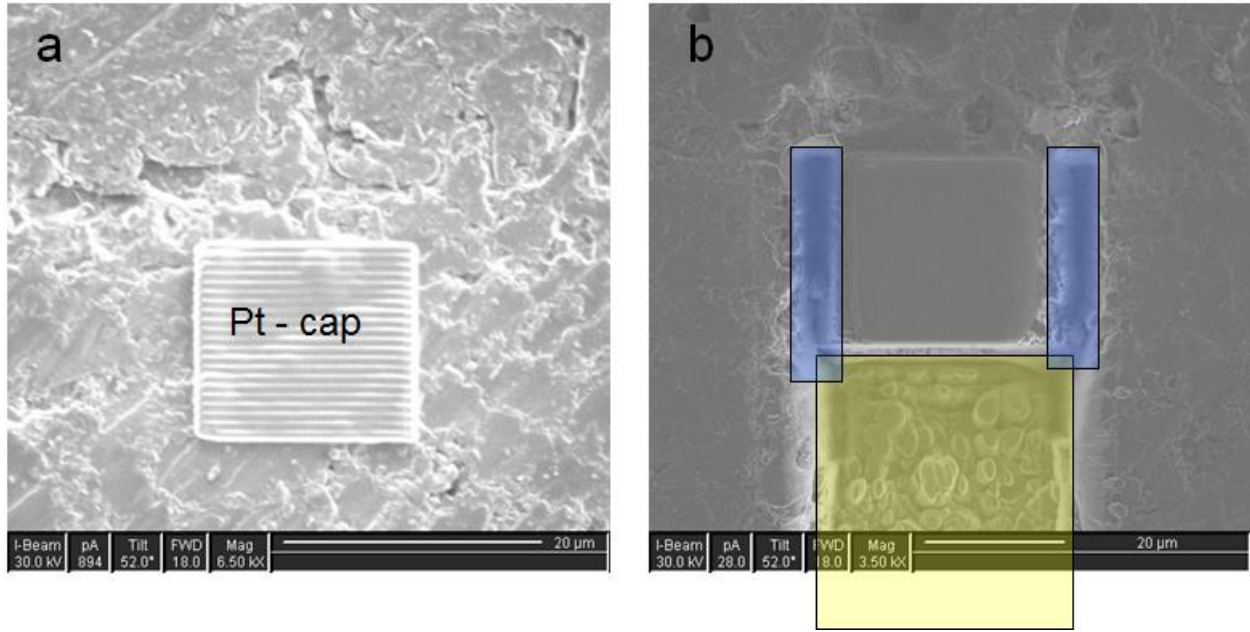


Figure A-1. Top down ion beam micrographs showing the C-trench procedure: (a) the region of interest covered by a platinum cap and (b) the capped region of interest surrounded by a C-trench, with highlighted milling areas.

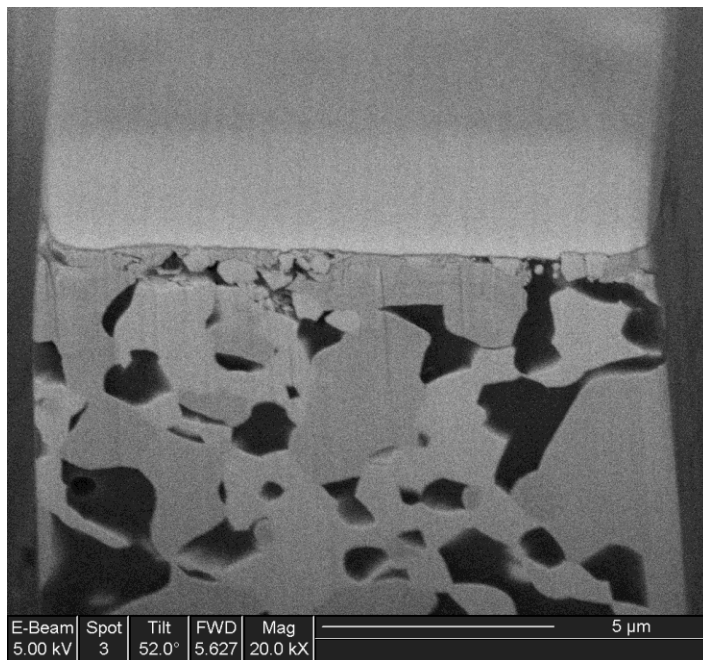


Figure A-2. Cross-sectional SEM image of composite SOFC electrode with a platinum cap at the top of the image.

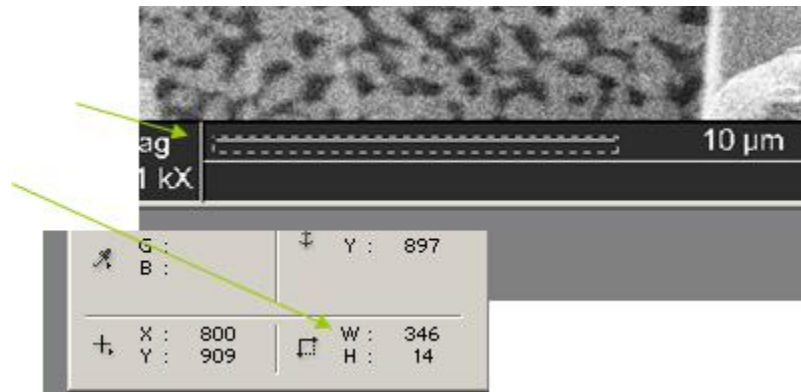


Figure A-3. Method to calibrate the pixel dimensions to that of the SEM image.

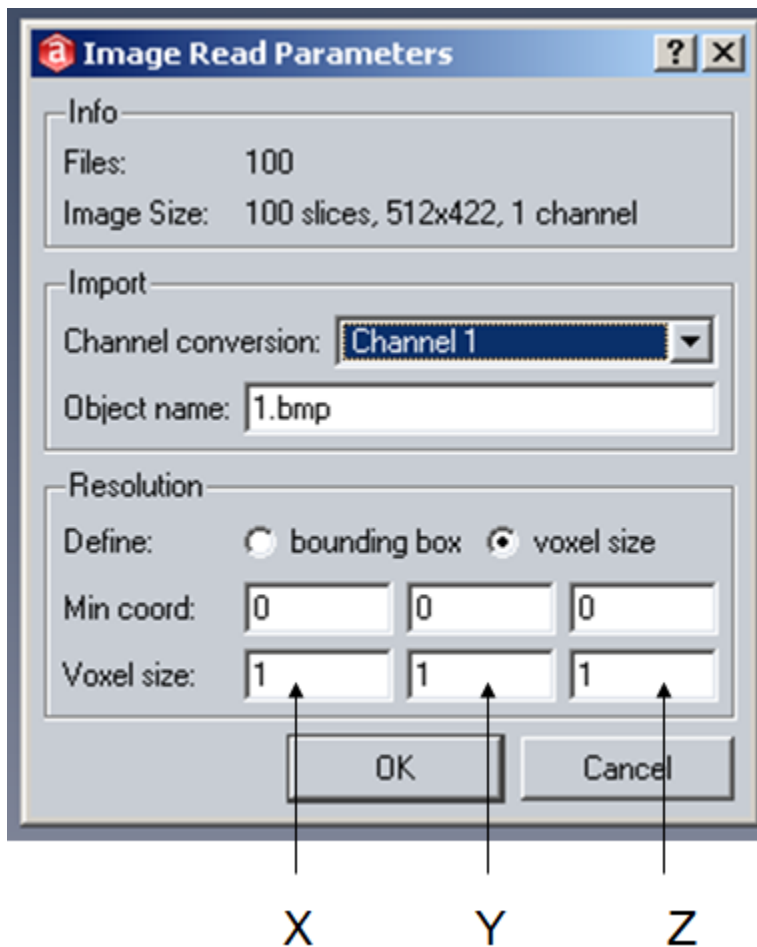


Figure A-4. Import window for Amira 4.0. Channel conversion should be “Channel 1” while the calibrated pixel dimensions are entered for X, Y, and Z.

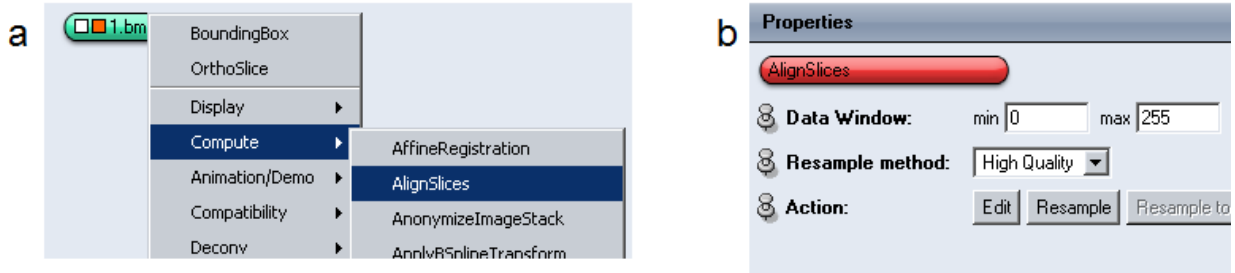


Figure A-5. The AlignSlices procedure from Amira with windows showing (a) the AlignSlices module creation process and (b) the AlignSlices properties window.

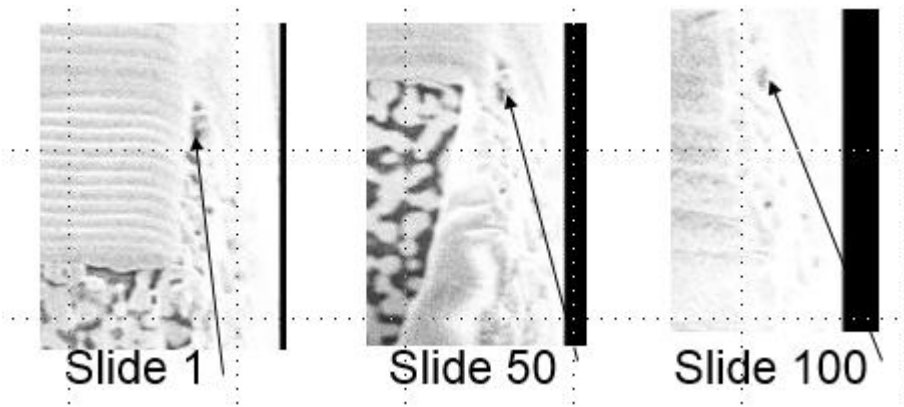


Figure A-6. A series of cross-sectional SEM images import for alignment. The fiducial mark is indicated in each slide by the arrow. Before alignment, image drift is evident from slide 1 to slide 100.

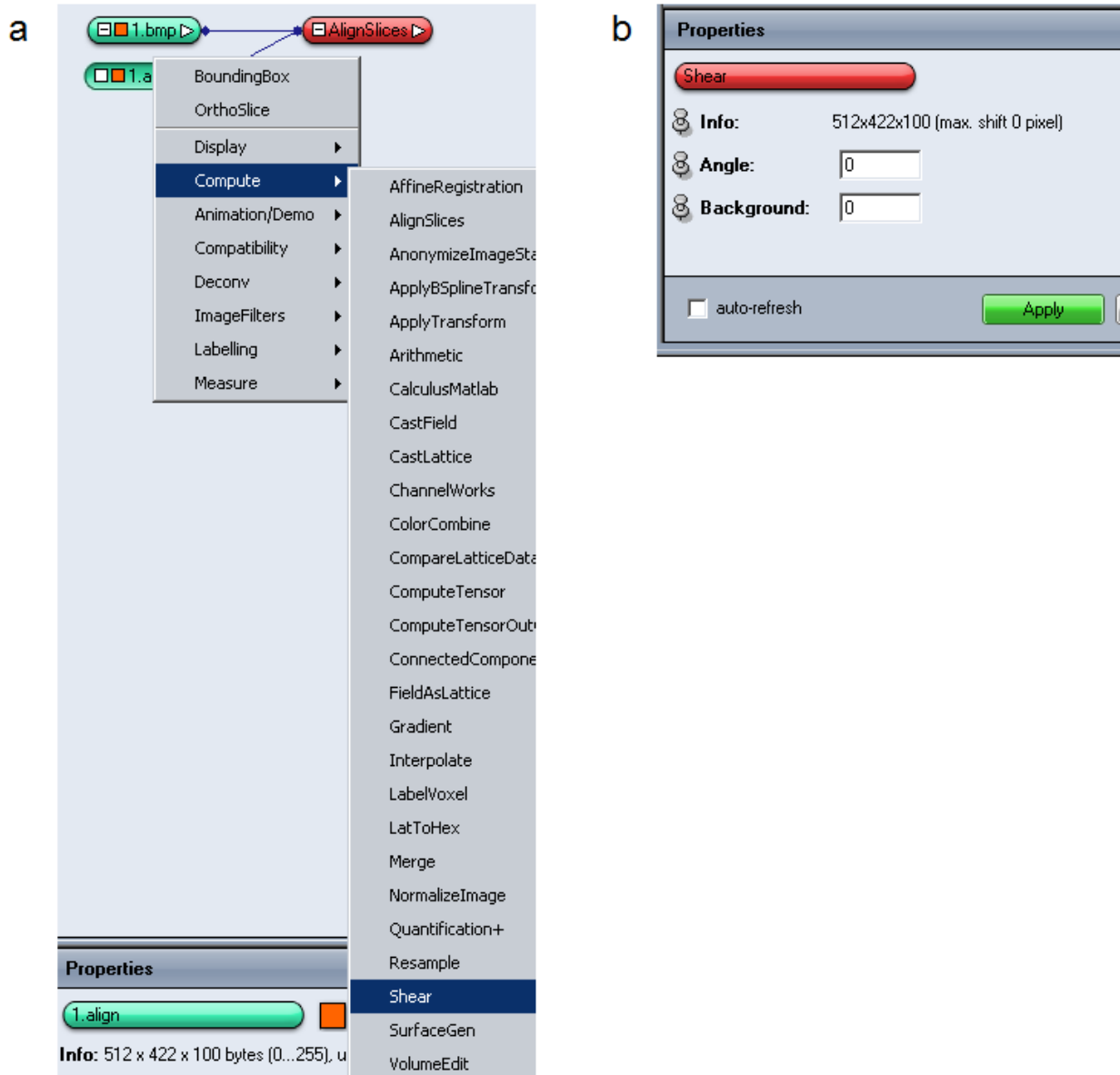


Figure A-7. The Shear procedure from Amira with windows showing (a) the Shear module creation process and (b) the Shear properties window.



Figure A-8. Amira properties window for the Sheared output module. The crop function is indicated by the arrow.

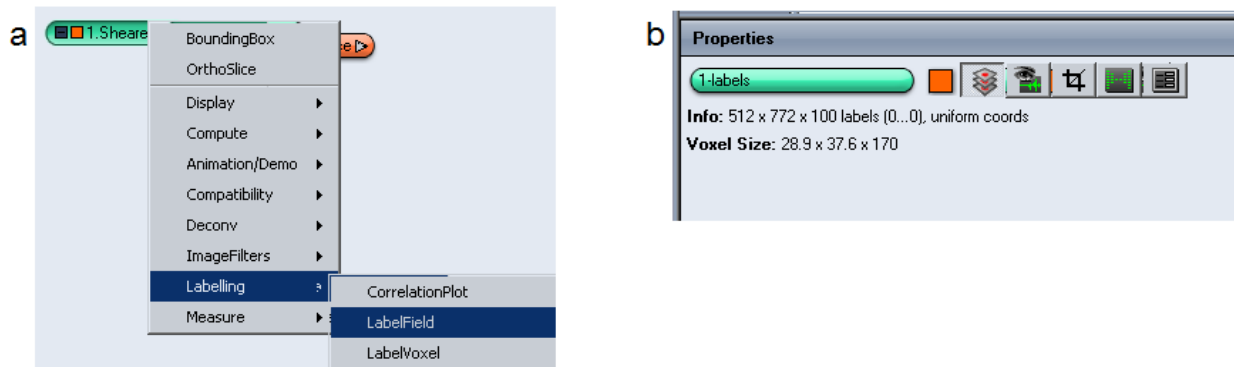


Figure A-9. The LabelField procedure from Amira with windows showing (a) the LabelField module creation process and (b) the LabelField properties window. The label editor is depressed in (b).

LIST OF REFERENCES

- [1] Research and Markets 2013.
- [2] P. Poizot, F. Dolhem, *Ener. Environ. Sci.* 4 (2011) 2003-2019.
- [3] U. S. Energy Information Administration 2009.
- [4] United Nations Development Programme 2004.
- [5] J.M. Tarascon, M. Armand, *Nature* 414 (2001) 359-367.
- [6] M.S. Whittingham, *Science* 192 (1976) 1126-1127.
- [7] M. Broussely, P. Biensan, B. Simon, *Electrochim. Acta* 45 (1999) 3-22.
- [8] D.W. Murphy, F.J. Disalvo, J.N. Carides, J.V. Waszczak, *Mater. Res. Bull.* 13 (1978) 1395-1402.
- [9] M. Lazzari, B. Scrosati, *J Electrochem. Soc.* 127 (1980) 773-774.
- [10] K. Mizushima, P.C. Jones, P.J. Wiseman, J.B. Goodenough, *Solid State Ionics* 3-4 (1981) 171-174.
- [11] T. Nagaura, K. Towaza, in: *Prog. Batt. Sol. Cell.* 1990.
- [12] J.O. Besenhard, G. Eichinger, *J Electroanal Chem.* 68 (1976) 1-18.
- [13] G. Eichinger, J.O. Besenhard, *J Electroanal Chem.* 72 (1976) 1-31.
- [14] S. Basu, C. Zeller, P.J. Flanders, C.D. Fuerst, W.D. Johnson, J.E. Fischer, *Mater. Sci. Eng.* 38 (1979) 275-283.
- [15] K. Xu, *Chem. Rev.* 104 (2004) 4303-4417.
- [16] L. El Ouatani, R. Dedryvere, C. Siret, P. Biensan, D. Gonbeau, *J Electrochem. Soc.* 156 (2009) A468-A477.
- [17] J.W. Fergus, *J. Power Sources* 195 (2010) 939-954.
- [18] P.G. Bruce, B. Scrosati, J.M. Tarascon, *Angew. Chem. Int. Edit.* 47 (2008) 2930-2946.
- [19] C.K. Chan, H.L. Peng, G. Liu, K. McIlwrath, X.F. Zhang, R.A. Huggins, Y. Cui, *Nature Nanotechnol.* 3 (2008) 31-35.
- [20] R.A. Huggins, W.D. Nix, *Ionics*, 6 (2000) 57-63.
- [21] U. Kasavajjula, C.S. Wang, A.J. Appleby, *J. Power Sources* 163 (2007) 1003-1039.

- [22] S.J. Lee, J.K. Lee, S.H. Chung, H.Y. Lee, S.M. Lee, H.K. Baik, *J. Power Sources* 97-8 (2001) 191-193.
- [23] J. Graetz, C.C. Ahn, R. Yazami, B. Fultz, *J Electrochem. Soc.* 151 (2004) A698-A702.
- [24] K.L. Lee, J.Y. Jung, S.W. Lee, H.S. Moon, J.W. Park, *J. Power Sources* 129 (2004) 270-274.
- [25] H.J. Jung, M. Park, S.H. Han, H. Lim, S.K. Joo, *Solid State Commun.* 125 (2003) 387-390.
- [26] H. Guo, H.L. Zhao, C.L. Yin, W.H. Qiu, *Mater. Sci. Eng. B Sol. St. Mater. Adv. Tech.* 131 (2006) 173-176.
- [27] M. Green, E. Fielder, B. Scrosati, M. Wachtler, J. Serra Moreno, *Electrochem. Solid St.* 6 (2003) A75-A79.
- [28] C.K. Chan, X.F. Zhang, Y. Cui, *Nano Lett.* 8 (2008) 307-309.
- [29] C.M. Park, J.H. Kim, H. Kim, H.J. Sohn, *Chem. Soc. Rev.* 39 (2010) 3115-3141.
- [30] T. Song, J.L. Xia, J.H. Lee, D.H. Lee, M.S. Kwon, J.M. Choi, J. Wu, S.K. Doo, H. Chang, W. Il Park, D.S. Zang, H. Kim, Y.G. Huang, K.C. Hwang, J.A. Rogers, U. Paik, *Nano Lett.* 10 (2010) 1710-1716.
- [31] W.B. Xing, A.M. Wilson, K. Eguchi, G. Zank, J.R. Dahn, *J Electrochem. Soc.* 144 (1997) 2410-2416.
- [32] C.S. Wang, G.T. Wu, X.B. Zhang, Z.F. Qi, W.Z. Li, *J Electrochem. Soc.* 145 (1998) 2751-2758.
- [33] M. Yoshio, H.Y. Wang, K. Fukuda, T. Umeno, N. Dimov, Z. Ogumi, *J Electrochem. Soc.* 149 (2002) A1598-A1603.
- [34] Y. Liu, K. Hanai, J. Yang, N. Imanishi, A. Hirano, Y. Takeda, *Electrochem. Solid St.* 7 (2004) A369-A372.
- [35] R. Huang, X. Fan, W.C. Shen, J. Zhu, *Appl. Phys. Lett.* 95 (2009).
- [36] L.F. Cui, Y. Yang, C.M. Hsu, Y. Cui, *Nano Lett.* 9 (2009) 3370-3374.
- [37] J. Lee, J. Bae, J. Heo, I.T. Han, S.N. Cha, D.K. Kim, M. Yang, H.S. Han, W.S. Jeon, J. Chung, *J Electrochem. Soc.* 156 (2009) A905-A910.
- [38] A.A. Arie, J.O. Song, J.K. Lee, *Mater. Chem. Phys.* 113 (2009) 249-254.
- [39] A.A. Arie, O.M. Vovk, J.K. Lee, *J Electrochem. Soc.* 157 (2010) A660-A665.
- [40] A.A. Arie, J.K. Lee, *Synthetic Met.* 161 (2011) 158-165.
- [41] B. Wang, X.L. Li, X.F. Zhang, B. Luo, M.H. Jin, M.H. Liang, S.A. Dayeh, S.T. Picraux, L.J. Zhi, *ACS Nano* 7 (2013) 1437-1445.

- [42] C.J. Yu, X. Li, T. Ma, J.P. Rong, R.J. Zhang, J. Shaffer, Y.H. An, Q. Liu, B.Q. Wei, H.Q. Jiang, *Adv. Ener. Mater.* 2 (2012) 68-73.
- [43] N.G. Rudawski, B.R. Yates, M.R. Holzworth, K.S. Jones, R.G. Elliman, A.A. Volinsky, *J. Power Sources* 223 (2013) 336-340.
- [44] B.Y. Tsaur, Z.L. Liao, J.W. Mayer, *Appl. Phys. Lett.* 34 (1979) 168-170.
- [45] J.K. Hirvonen, *J. Vac. Sci. Technol. A.* 3 (1985) 2691-2692.
- [46] B.M. Paine, *P. Soc. Photo-Opt. Inst.* 530 (1985) 114-121.
- [47] B.M. Paine, R.S. Averbach, *Nucl. Instrum. Meth. B.* 7-8 (1985) 666-675.
- [48] J.E. Pawel, C.J. Mchargue, L.J. Romana, J.J. Wert, *Surf. Coat. Tech.* 51 (1992) 129-132.
- [49] G.S. Chang, S.M. Jung, Y.S. Lee, I.S. Choi, C.N. Whang, J.J. Woo, Y.P. Lee, *J Appl. Phys.* 81 (1997) 135-138.
- [50] L. Guzman, A. Miotello, R. Checchetto, M. Adami, *Surf. Coat. Tech.* 158 (2002) 558-562.
- [51] J.H. Hong, Y. Lee, S. Han, K.J. Kim, *Surf. Coat. Tech.* 201 (2006) 197-202.
- [52] S. Yeo, *Int. J. Adhes. Adhes.* 40 (2013) 145-148.
- [53] D.J. Oconnor, J.P. Biersack, *Nucl. Instrum. Meth. B.* 15 (1986) 14-19.
- [54] W.D. Wilson, L.G. Haggmark, J.P. Biersack, *Phys. Rev. B* 15 (1977) 2458-2468.
- [55] J.P. Biersack, L.G. Haggmark, *Nuc. Inst. Meth.* 174 (1980) 257-269.
- [56] J.F. Ziegler, *Nucl. Instrum. Meth. B.* 219 (2004) 1027-1036.
- [57] O. Scherzer, *Z. Phys.* 114 (1939) 427-434.
- [58] M. Haider, P. Hartel, H. Muller, S. Uhlemann, J. Zach, *Microsc. Microanal.* 16 (2010) 393-408.
- [59] S. Uhlemann, H. Muller, P. Hartel, J. Zach, M. Haider, *Phys. Rev. Lett.* 111 (2013).
- [60] T. Tao, J.S. Ro, J. Melngailis, Z.L. Xue, H.D. Kaesz, *J Vac. Sci. Tech. B* 8 (1990) 1826-1829.
- [61] L.A. Giannuzzi, F.A. Stevie, *Micron* 30 (1999) 197-204.
- [62] W.C. Oliver, G.M. Pharr, *J Mater. Res.* 7 (1992) 1564-1583.
- [63] J. Chen, S.J. Bull, *J Mater. Res.* 24 (2009) 590-598.
- [64] J. Graetz, C.C. Ahn, R. Yazami, B. Fultz, *Electrochem. Solid St.* 6 (2003) A194-A197.
- [65] E.M. Kindle, *J Geo.* 31 (1923) 138-145.

- [66] X. Xiao, P. Liu, M.W. Verbrugge, H. Haftbaradaran, H. Gao, J. Power Sources 196 (2011) 1409-1416.
- [67] J. Singh, D.E. Wolfe, J Mater. Sci. 40 (2005) 1-26.
- [68] T. Shinoda, H. Miyake, T. Matsuzaka, T. Matsumoto, H. Kanai, Mater. Sci. Tech. 8 (1992) 913-921.
- [69] M.M. de Lima, R.G. Lacerda, J. Vilcarromero, F.C. Marques, J Appl. Phys. 86 (1999) 4936-4942.
- [70] E. Johlin, N. Tabet, S. Castro-Galnares, A. Abdallah, M.I. Bertoni, T. Asafa, J.C. Grossman, S. Said, T. Buonassisi, Phys. Rev. B 85 (2012).
- [71] M.R. Stjohn, A.J. Furgala, A.F. Sammells, J Electrochem. Soc. 129 (1982) 246-250.
- [72] Argonne National Laboratory, Illinois, 1979.
- [73] S. Lai, A.F. Sammells, Proc. Inter. Ener. Conv. Eng. Conf. (1977).
- [74] C.S. Fuller, J.C. Severiens, Phys. Rev. 96 (1954) 21-24.
- [75] B. Laforge, L. Levan-Jodin, R. Salot, A. Billard, J Electrochem. Soc. 155 (2008) A181-A188.
- [76] O.W. Holland, B.R. Appleton, J. Narayan, J Appl. Phys. 54 (1983) 2295-2301.
- [77] B.R. Appleton, O.W. Holland, D.B. Poker, J. Narayan, D. Fathy, Nucl. Instrum. Meth. B. 7-8 (1985) 639-644.
- [78] L. Romano, G. Impellizzeri, M.V. Tomasello, F. Giannazzo, C. Spinella, M.G. Grimaldi, J Appl. Phys. 107 (2010).
- [79] B.L. Darby, B.R. Yates, N.G. Rudawski, K.S. Jones, A. Kontos, R.G. Elliman, Thin Solid Films 519 (2011) 5962-5965.
- [80] D.J. Oliver, J.E. Bradby, S. Ruffell, J.S. Williams, P. Munroe, J Appl. Phys. 106 (2009).
- [81] A. Witvrouw, F. Spaepen, J Appl. Phys. 74 (1993) 7154-7161.
- [82] E. Borch, S. Degennaro, R. Macii, M. Zoli, J Phys. D 21 (1988) 1304-1305.
- [83] J.I. Jang, M.J. Lance, S.Q. Wen, G.M. Pharr, Appl. Phys. Lett. 86 (2005).
- [84] D.J. Oliver, J.E. Bradby, J.S. Williams, M.V. Swain, P. Munroe, Nanotech. 19 (2008).
- [85] D.J. Oliver, J.E. Bradby, J.S. Williams, M.V. Swain, P. Munroe, J Appl. Phys. 101 (2007).
- [86] P. Lemaitre, J Mater. Sci. Lett. 7 (1988) 895-896.
- [87] B.R. Lawn, B.J. Hockey, S.M. Wiederhorn, J Mater. Sci. 15 (1980) 1207-1223.
- [88] L. Baggetto, P.H.L. Notten, J Electrochem. Soc. 156 (2009) A169-A175.

- [89] S. Yoon, C.M. Park, H.J. Sohn, *Electrochem. Solid St.* 11 (2008) A42-A45.
- [90] L. Baggetto, E.J.M. Hensen, P.H.L. Notten, *Electrochim. Acta* 55 (2010) 7074-7079.
- [91] V.A. Sethuraman, V. Srinivasan, A.F. Bower, P.R. Guduru, *J Electrochem. Soc.* 157 (2010) A1253-A1261.
- [92] J.J. Wortman, R.A. Evans, *J Appl. Phys.* 36 (1965) 153-&.
- [93] R.A. Sharma, R.N. Seefurth, *J Electrochem. Soc.* 123 (1976) C239-C239.
- [94] B.A. Boukamp, G.C. Lesh, R.A. Huggins, *J Electrochem. Soc.* 128 (1981) 725-729.
- [95] G.A. Tritsarlis, K.J. Zhao, O.U. Okeke, E. Kaxiras, *J Phys. Chem. C* 116 (2012) 22212-22216.
- [96] S. Bourderau, T. Brousse, D.M. Schleich, *J. Power Sources* 81 (1999) 233-236.
- [97] M.H. Ryou, D.J. Lee, J.N. Lee, Y.M. Lee, J.K. Park, J.W. Choi, *Adv. Ener. Mater.* 2 (2012) 645-650.
- [98] A. Magasinski, P. Dixon, B. Hertzberg, A. Kvit, J. Ayala, G. Yushin, *Nature Mater.* 9 (2010) 461-461.
- [99] W.R. Liu, M.H. Yang, H.C. Wu, S.M. Chiao, N.L. Wu, *Electrochem. Solid St.* 8 (2005) A100-A103.
- [100] L.B. Chen, X.H. Xie, J.Y. Xie, K. Wang, J. Yang, *J Appl. Electrochem.* 36 (2006) 1099-1104.
- [101] S.R. Gowda, V. Pushparaj, S. Herle, G. Girishkumar, J.G. Gordon, H. Gullapalli, X.B. Zhan, P.M. Ajayan, A.L.M. Reddy, *Nano Lett.* 12 (2012) 6060-6065.
- [102] K.J. Zhao, M. Pharr, L. Hartle, J.J. Vlassak, Z.G. Suo, *J. Power Sources* 218 (2012) 6-14.
- [103] Q.N. Sa, Y. Wang, *J. Power Sources* 208 (2012) 46-51.
- [104] H.K. Kang, S.R. Lee, W.I. Cho, B.W. Cho, *Phys. Chem. Chem. Phys.* 15 (2013) 1569-1577.
- [105] W. Li, R. Yang, X.J. Wang, T. Wang, J. Zheng, X.G. Li, *J. Power Sources* 221 (2013) 242-246.
- [106] H.X. Li, H.M. Bai, Z.L. Tao, J. Chen, *J. Power Sources* 217 (2012) 102-107.
- [107] G.B. Cho, J.P. Noh, H.J. Sung, S.H. Lee, Y.M. Im, H.J. Ahn, K.W. Kim, *Nano. Res. Lett.* 7 (2012).
- [108] S.K. Soni, B.W. Sheldon, X.C. Xiao, M.W. Verbrugge, D. Ahn, H. Haftbaradaran, H.J. Gao, *J Electrochem. Soc.* 159 (2012) A38-A43.

- [109] T.L. Kulova, A.M. Skundin, Y.V. Pleskov, O.I. Kon'kov, E.I. Terukov, I.N. Trapeznikova, *Chem. Biochem. Eng. Quart.* 21 (2007) 83-92.
- [110] M.T. McDowell, S.W. Lee, J.T. Harris, B.A. Korgel, C.M. Wang, W.D. Nix, Y. Cui, *Nano Lett.* 13 (2013) 758-764.
- [111] J.W. Wang, Y. He, F.F. Fan, X.H. Liu, S.M. Xia, Y. Liu, C.T. Harris, H. Li, J.Y. Huang, S.X. Mao, T. Zhu, *Nano Lett.* 13 (2013) 709-715.
- [112] M.N. Obrovac, L.J. Krause, *J Electrochem. Soc.* 154 (2007) A103-A108.
- [113] S. Xun, X. Song, L. Wang, M.E. Grass, Z. Liu, V.S. Battaglia, G. Liu, *J Electrochem. Soc.* 158 (2011) A1260-A1266.
- [114] Q. Sun, B. Zhang, Z.W. Fu, *Appl. Surf. Sci.* 254 (2008) 3774-3779.
- [115] W.Y. Hsien, Z.L. Dong, C.F. Li, S.K. Yen, *Surf. Coat. Tech.* 216 (2013) 52-59.
- [116] H.S. Ryu, H.J. Ahn, K.W. Kim, J.H. Ahn, J.Y. Lee, E.J. Cairns, *J. Power Sources* 140 (2005) 365-369.
- [117] N.N. Sinha, J.C. Burns, R.J. Sanderson, J. Dahn, *J Electrochem. Soc.* 158 (2011) A1400-A1403.
- [118] W. Fredriksson, K. Edstrom, *Electrochim. Acta* 79 (2012) 82-94.
- [119] S. Ohara, J. Suzuki, K. Sekine, T. Takamura, *J. Power Sources* 136 (2004) 303-306.
- [120] A. Kushima, J.Y. Huang, J. Li, *ACS Nano* 6 (2012) 9425-9432.
- [121] K.J. Zhao, W.L. Wang, J. Gregoire, M. Pharr, Z.G. Suo, J.J. Vlassak, E. Kaxiras, *Nano Lett.* 11 (2011) 2962-2967.
- [122] V.B. Shenoy, P. Johari, Y. Qi, *J. Power Sources* 195 (2010) 6825-6830.
- [123] J.C. Li, A.K. Dozier, Y.C. Li, F.Q. Yang, Y.T. Cheng, *J Electrochem. Soc.* 158 (2011) A689-A694.
- [124] S.W. Lee, M.T. McDowell, J.W. Choi, Y. Cui, *Nano Lett.* 11 (2011) 3034-3039.
- [125] K.J. Zhao, M. Pharr, Q. Wan, W.L. Wang, E. Kaxiras, J.J. Vlassak, Z.G. Suo, *J Electrochem. Soc.* 159 (2012) A238-A243.
- [126] H. Yang, S. Huang, X. Huang, F.F. Fan, W.T. Liang, X.H. Liu, L.Q. Chen, J.Y. Huang, J. Li, T. Zhu, S.L. Zhang, *Nano Lett.* 12 (2012) 1953-1958.
- [127] M. Pharr, K.J. Zhao, X.W. Wang, Z.G. Suo, J.J. Vlassak, *Nano Lett.* 12 (2012) 5039-5047.
- [128] J.W. Choi, J. McDonough, S. Jeong, J.S. Yoo, C.K. Chan, Y. Cui, *Nano Lett.* 10 (2010) 1409-1413.
- [129] J.P. Maranchi, A.F. Hepp, P.N. Kumta, *Electrochem. Solid St.* 6 (2003) A198-A201.

- [130] H.S. Kim, M.G. So, S.M. Lee, Bull. Kor. Chem. Soc. 29 (2008) 2441-2444.
- [131] A. Ebe, E. Takahashi, Y. Iwamoto, N. Kuratani, S. Nishiyama, O. Imai, K. Ogata, Y. Setsuhara, S. Miyake, Thin Solid Films 282 (1996) 356-359.
- [132] G.K. Wolf, Nucl. Instrum. Meth. B. 46 (1990) 369-378.
- [133] P. Martin, Gold Bull. 19 (1986) 14.
- [134] A. Nash, P. Nash, Bull. Alloy Phase Diag. 8 (1987) 9.
- [135] Q.Y. Li, K.S. Kim, Proc. Royal Soc. A 464 (2008) 1319-1343.
- [136] D. Gostovic, N.J. Vito, K.A. O'Hara, K.S. Jones, E.D. Wachsman, J Amer. Cer. Soc. 94 (2011) 620-627.
- [137] K.T. Lee, N.J. Vito, H.S. Yoon, E.D. Wachsman, J Electrochem. Soc. 159 (2012) F187-F193.
- [138] K.T. Lee, N.J. Vito, E.D. Wachsman, J. Power Sources 228 (2013) 220-228.

BIOGRAPHICAL SKETCH

Nicholas Vito was born in 1985 in Illinois. Having not discovered the fountain of youth, he has increased in volume, mass, and became more knowledgeable over the years. In May 2008, he graduated from the University of Illinois at Urbana-Champaign with a B. S. in materials science and engineering and decided to take his talents to the University of Florida. He graduated with a Ph.D. in material science and engineering in December 2013.